Max-Planck-Institut
für Meteorologie

MAX-PLANCK-GESELLSCHAFT

International Max Planck Research School
on Earth System Modelling

Arctic boundary-layer processes and climate change

Felix Pithan

Hamburg 2014

Berichte zur Erdsystemforschung
Reports on Earth System Science

158
2014

Hinweis

Die Berichte zur Erdsystemforschung werden vom Max-Planck-Institut für Meteorologie in Hamburg in unregelmäßiger Abfolge herausgegeben.

Sie enthalten wissenschaftliche und technische Beiträge, inklusive Dissertationen.

Die Beiträge geben nicht notwendigerweise die Auffassung des Instituts wieder.

Die "Berichte zur Erdsystemforschung" führen die vorherigen Reihen "Reports" und "Examensarbeiten" weiter.

Anschrift / Address

Max-Planck-Institut für Meteorologie
Bundesstrasse 53
20146 Hamburg
Deutschland

Tel./Phone: +49 (0)40 4 11 73 - 0
Fax: +49 (0)40 4 11 73 - 298

name.surname@mpimet.mpg.de
www.mpimet.mpg.de

Notice

The Reports on Earth System Science are published by the Max Planck Institute for Meteorology in Hamburg. They appear in irregular intervals.

They contain scientific and technical contributions, including Ph. D. theses.

The Reports do not necessarily reflect the opinion of the Institute.

The "Reports on Earth System Science" continue the former "Reports" and "Examensarbeiten" of the Max Planck Institute.

Layout

Bettina Diallo and Norbert P. Noreiks
Communication

Copyright

Photos below: ©MPI-M
Photos on the back from left to right:
Christian Klepp, Jochem Marotzke,
Christian Klepp, Clotilde Dubois,
Christian Klepp, Katsumasa Tanaka

Max-Planck-Institut
für Meteorologie

MAX-PLANCK-GESELLSCHAFT

International Max Planck Research School
on Earth System Modelling

Arctic boundary-layer processes and climate change

Felix Pithan

Hamburg 2014

Berichte zur Erdsystemforschung
Reports on Earth System Science

158
2014

Felix Pithan

Max-Planck-Institut für Meteorologie
Bundesstrasse 53
20146 Hamburg

Als Dissertation angenommen
vom Fachbereich Geowissenschaften der Universität Hamburg

auf Grund der Gutachten von

Prof. Dr. Bjorn Stevens,
Dr. Thorsten Mauritsen und
Prof. Rodrigo Caballero

Hamburg, den 30. Juni 2014
Professor Dr. Christian Betzler
Leiter des Departments Geowissenschaften

ISSN 1614-1199

Abstract

Climate change is amplified in the Arctic compared to lower latitudes. Contrary to a widespread opinion, this thesis shows that atmospheric processes rather than the retreat of snow and ice dominate the Arctic amplification of warming in contemporary climate models. Stable stratification suppresses vertical mixing in the lower Arctic atmosphere. Warming therefore remains confined to a shallow layer near the surface and relatively little heat is radiated to space. Additionally, at the cold Arctic surface temperatures, more warming is required to obtain the same increase in outgoing longwave radiation than in the tropics.

The stratification or vertical temperature structure of the lower Arctic atmosphere thus plays an important role for Arctic climate change. Current climate models poorly represent this vertical structure, mostly because they lack mixed-phase clouds in Arctic winter. Mixed-phase clouds inhibit surface radiative cooling and cause temperature inversions to be weak and elevated. The lack of such clouds is traced back to deficiencies in representing mixed-phase cloud microphysics at cold temperatures for most analysed models. In the absence of mixed-phase clouds, when the surface cools radiatively, turbulent heat fluxes towards the surface are crucial for inversion strength and the surface heat budget. It is known that general circulation models tend to overestimate turbulent fluxes in stably stratified boundary layers, but reducing turbulent diffusivity to a more realistic range leads to biases in the large-scale circulation. A new turbulence scheme with realistic diffusivity is implemented into ECHAM6 and the effect of non-resolved orography on the flow is increased to obtain realistic pressure and wind fields.

Zusammenfassung

Das Klima der Arktis verändert sich stärker als das niedrigerer Breitengrade. Im Gegensatz zu einer weitverbreiteten Auffassung zeigt diese Arbeit, dass Prozesse in der Atmosphäre und nicht der Rückgang von Schnee- und Eisbedeckung der wesentliche Grund für diese arktische Verstärkung des Klimawandels in den aktuellen Klimamodellen sind. Die stabile Schichtung von Luftmassen unterdrückt die vertikale Durchmischung der unteren arktischen Atmosphäre. Die Erwärmung bleibt dadurch auf eine dünne Schicht in Bodennähe begrenzt, und relativ wenig Energie wird ins Weltall abgestrahlt. Außerdem ist bei den kalten arktischen Bodentemperaturen eine größere Erwärmung als in den Tropen notwendig, um überall den gleichen Anstieg der abgegebenen Langwellenstrahlung zu erhalten.

Die Schichtung bzw. das vertikale Temperaturprofil der unteren arktischen Atmosphäre spielt daher eine wichtige Rolle für Klimawandel in der Arktis. Klimamodelle repräsentieren diese Struktur nur sehr schlecht. Viele Modelle reproduzieren den charakteristischen bewölkten Zustand der arktischen Atmosphärengrenzschicht im Winter nicht, in dem Mischphasenwolken Strahlungsabkühlung an der Oberfläche verhindern und Temperaturinversionen schwach und von der Oberfläche entfernt sind. Das Fehlen solcher Wolken wird in den meisten analysierten Modellen auf Defizite in der Darstellung von Mischphasenwolkenmikrophysik zurückgeführt. Wenn keine Mischphasenwolken vorhanden sind und der Boden durch Strahlungsprozesse Wärme verliert, sind turbulente Wärmeflüsse von entscheidender Bedeutung für die Inversionsstärke und das Energiebudget am Boden. Bekanntermaßen neigen Wetter- und Klimamodelle dazu, turbulente Wärmeflüsse in stabilen Grenzschichten zu überschätzen, aber eine Verringerung der turbulenten Diffusivität auf realistischere Werte führt zu Problemen in der großskaligen Zirkulation. Ein neues Turbulenzschema mit realistischer Diffusivität wird in ECHAM6 eingebaut, und der Effekt nicht aufgelöster Orografie auf den Wind wird erhöht, um realistische Druck- und Windfelder zu erhalten.

Contents

1 Introduction **7**
1.1 Feedback processes and Arctic amplification 12
1.2 Inversions, mixed-phase clouds and surface fluxes in the Arctic boundary layer 15
1.3 Stable boundary layers and the large-scale circulation 16

2 Temperature feedbacks dominate Arctic amplification in CMIP5 climate models **19**
2.1 Methods 25

3 Statistical artifacts in 'Current GCM's unrealistic negative feedback in the Arctic' by Boé et al. **29**
3.1 Introduction 29
3.2 Feedback analysis 32
3.3 Statistical artifacts from self-correlation 33
3.4 Discussion and conclusion 36

4 Mixed-phase clouds cause climate model biases in Arctic wintertime temperature inversions **39**
4.1 Introduction 39
4.2 Models and data 43
  4.2.1 Single-column models, forcing and initialisation 44
4.3 Lower tropospheric temperature structure in CMIP5 models 48
4.4 The formation of Arctic air masses 52
4.5 The two states of the boundary layer in observations and CMIP5 models 55
  4.5.1 The role of mixed-phase cloud microphysics 62
  4.5.2 Model sensitivity to turbulent diffusivity and heat conduction . . 64
4.6 Conclusions 66

5 Challenges in improving the representation of boundary-layer turbulence in a general circulation model **69**
5.1 Introduction 69
5.2 Model, data and experiments 72

- 5.2.1 ECHAM6 climate model . . . 72
- 5.2.2 Data . . . 74
- 5.2.3 Experiments . . . 75
- 5.3 Total turbulent energy scheme . . . 75
  - 5.3.1 Turbulent potential and turbulent kinetic energy . . . 76
  - 5.3.2 Length scales . . . 77
  - 5.3.3 Diffusivities under stable and unstable stratification . . . 77
  - 5.3.4 Surface layer . . . 78
- 5.4 Results and discussion . . . 79
  - 5.4.1 Performance of the total turbulent energy scheme in idealised single-column experiments . . . 79
  - 5.4.2 Surface drag and large-scale pressure gradients . . . 84
  - 5.4.3 Neutral turbulent Prandtl number, temperature and precipitation 87
- 5.5 Discussion and Conclusions . . . 90

6 Conclusions **93**

Bibliography **97**

Chapter 1

Introduction

Despite covering only a small fraction of the globe, the Arctic has an important place in its climate system, and maybe an even more central role in our understanding of that system. It is also the source of some of the most emblematic pictures that are key to how the public perceives climate change including in countries far equatorwards of the Arctic circle. While global climate change is often considered a very abstract phenomenon that is difficult to grasp for non-specialist and non-scientific audiences, observations of retreating sea ice and pictures of melting ice and glaciers have attracted wide attention and are often considered the most graphical representations of a warming planet. Sea-ice retreat is also one of the reasons the polar bear is threatened by extinction, making the species the mascot of many debates on the impacts of climate change and the need to limit greenhouse gas emissions and mitigate further global warming (Manzo 2010).

Figure 1.1: Polar bears on sea ice, picture courtesy of Jakob Grahn, University of Tromsø

This thesis investigates why the Arctic warms faster than the rest of the planet. It strives to explain what causes the special vertical structures of temperature and humidity in the lower Arctic atmosphere, and how these interact with clouds and heat fluxes at the surface. It also investigates the role of boundary-layer turbulence for global climate, a typical area in which observations from the Arctic have been used to understand processes and constrain parametrisations for global models. The following section explains how the Arctic is special from a physical point of view, and how it interacts with the rest of the climate system.

While the Tropics receive more energy from the sun than they radiate back to space, the extra-tropical and especially the polar regions radiate more energy to space than they absorb from the sun (Figure 1.2). The surplus energy from the Tropics is carried poleward by the atmospheric and oceanic circulations. As long as the climate system is in equilibrium, the Tropical surplus and the extra-tropical deficit cancel. The difference between the energy absorbed from the sun and that radiated to space poleward of a given latitude must be transported across that latitude by atmospheric or oceanic motions. The radiation budgets at low and high latitudes are thus intrinsically linked to each other and the large-scale circulation of the atmosphere and oceans.

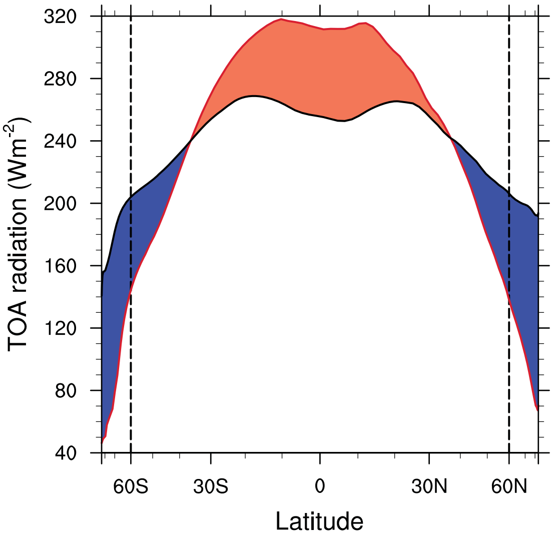

Figure 1.2: Zonal mean top-of-atmosphere absorbed shortwave radiation (red) and outgoing longwave radiation (black). Orange and blue areas represent the regional energy surplus respectively deficit that drive and are balanced by the atmospheric and oceanic circulation. Radiation fluxes are taken from an AMIP run (1979-2008) using ECHAM 6.2. The x-Axis is scaled to represent the fractional surface area occupied by each latitude band, such that the orange and blue areas are of equal size.

Throughout most of the planet, temperatures usually decrease with height in the Troposphere. Because the Arctic radiates more energy to space than it receives from the sun, its surface is often colder than the air aloft, where the atmospheric heat transport arrives from mid-latitudes (Figure 1.3). This temperature inversion is typical of the Arctic atmosphere, and we will later discuss its relevance to climate change.

When the global climate is disturbed, for a example by a uniform increase in the greenhouse effect, the atmosphere reacts differently at low and high latitudes. This causes different changes in the regional energy budgets, and the poleward energy transport adjusts to the new state. Overall, these processes lead to surface temperature change being amplified in the Arctic compared to the global mean. Arctic warming directly affects the ice masses of the Greenland ice sheet which contain the equivalent of about 7 m of global sea-level rise and have contributed several metres to past sea-level variations (Huybrechts 2002). The Arctic and subarctic permafrost regions are substantial carbon pools, and whether or how quickly thawing permafrost might release substantial amounts of methane is a matter of lively scientific debate (Whiteman et al. 2013; Notz et al. 2013). On shorter timescales, changes in the Arctic can impact lower latitudes by triggering changes in the Atlantic meridional overturning circulation which drives an important northward heat transport in the Atlantic (Jungclaus et al. 2005), or by changing the atmospheric circulation patterns that control northern hemisphere mid-latitude winter conditions (Petoukhov and Semenov 2010).

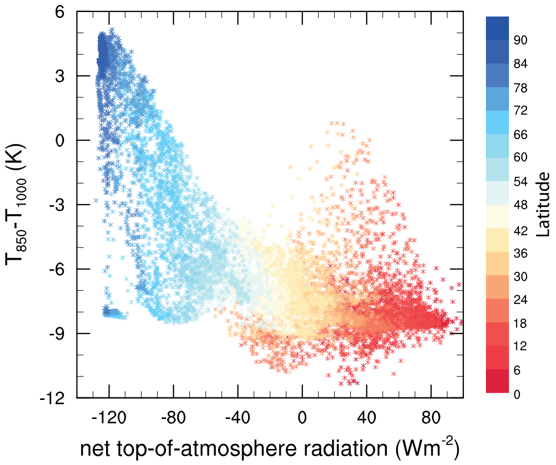

Figure 1.3: Difference between annual mean temperatures at 850 and 1000 hPa vs. top-of-atmosphere net radiation balance. Colours show latitude bands from the equator to the pole. Data source as in Fig. 1.2, Northern Hemisphere only.

The climate of the Arctic is further characterised by the contrast between polar day and polar night creating a very pronounced seasonal cycle and by feedbacks in the coupled atmosphere-sea-ice-ocean system enhancing interannual variability. This large seasonal and interannual variability, extreme environmental conditions and the logistic difficulties of accessing the remote polar regions make the Arctic not only a very interesting but also challenging place to study the behaviour of our climate system. As a consequence, in-situ observations from the Arctic remain scarce even after more than a century of scientific exploration, and long-term climate records are totally lacking for the central Arctic ocean (Figure 1.4). Even remote sensing data are often limited to lower latitudes either by restricted coverage of geostationary satellites bound to an orbit over the equator or by the difficulties of adapting retrievals to the special conditions of the polar atmosphere. Substantial and unobserved warming over the Arctic ocean has even been suggested to explain why the global mean surface temperatures recorded by global data sets have increased so little in the past decade, a phenomenon known as the global warming hiatus (Cowtan and Way 2013). According to the research, this apparent hiatus would reduce to heat being redistributed from the observed mid-latitudes to the Arctic, where the global surface temperature records lack data and have to recur to extrapolating available observations.

The Arctic continues to attract the attention of earth system scientists from many disciplines for reasons that go beyond the region's immediate role for global climate and the weather of densely populated mid-latitude regions. It is considered a natural laboratory used to investigate topics as diverse as cloud-aerosol interactions, boundary-layer turbulence, cloud-radiation and atmosphere-surface interaction, to name only a few examples. Pristine background conditions allow to study cloud formation processes at low cloud condensation nuclei (CCN) and ice nuclei (IN) concentrations as well as the impact of pollution, and the long-lived stable boundary layers building up over sea ice in polar night provide an almost ideal setting to study turbulence under stable stratification with homogeneous surface conditions.

The Arctic also allows us to test our understanding of meteorological processes and climate by applying models and concepts at the limit or beyond the range of conditions for which they were conceived. One example for this are Arctic stratus clouds, widely extending low-level cloud decks that cover much of the Arctic (Morrison et al. 2012; Solomon et al. 2014). These clouds are the cold counterparts to the stratocumulus cloud decks occupying the eastern margins of subtropical oceans. Both cloud types typically have a temperature inversion near cloud top with substantially higher potential temperatures above the cloud. Water that evaporates at the surface provides the moisture that feeds subtropical stratus clouds, and the free tropospheric air aloft is much dryer than the boundary layer at low latitudes. In the Arctic, free tropospheric air, which is often moister than the near-surface air, can provide moisture for stratus clouds. Exploring the physical mechanisms that control Arctic clouds and contrasting these with what we know about subtropical clouds can help us to improve our understanding of

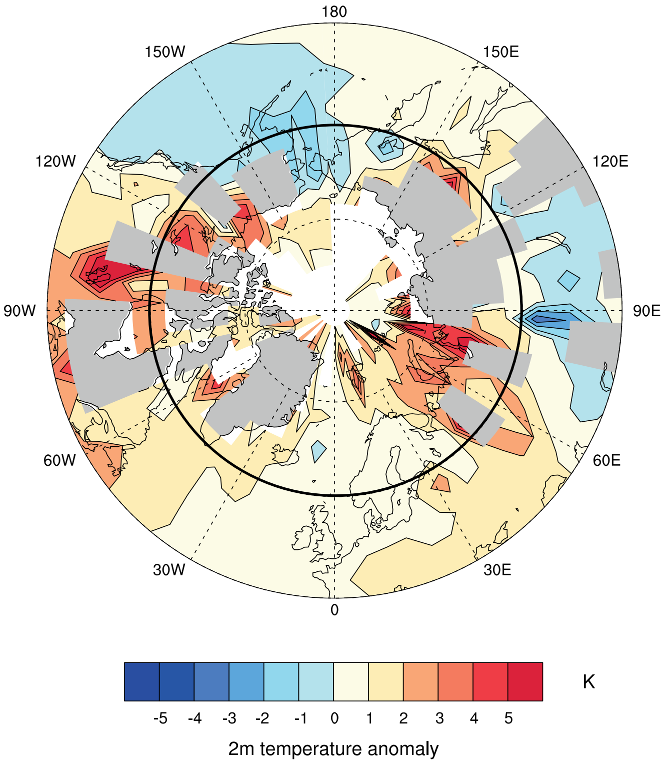
180
150W
150E
120W
120E
90W
90E
60W
60E
30W
30E
0
-5
-4
-3
-2
-1
0
1
2
3
4
5
K
2m temperature anomaly

Figure 1.4: Temperature anomalies relative to the 1961-1990 mean for the year 2012 according to the HadCRUT data set (Jones et al. 1999). The thick black line represents 60°N. Data is lacking for large parts of northern Siberia, Greenland, the Canadian Arctic Archipelago and the central Arctic ocean.

cloud processes in the climate system in general.

The remainder of this introductory section places the individual research questions for each chapter into the context of the scientific knowledge, open questions and current research initiatives on Arctic and sometimes global climate. More specific background information is given in the introduction to each individual chapter.

1.1 Feedback processes and Arctic amplification

The Earth's climate system is in equilibrium when the absorbed solar radiation is balanced by the infrared radiation out to space in the global mean. This balance can be perturbed by an external forcing which could be an increase in greenhouse gas concentrations or a decrease in the sun's strength. The Earth then radiates less (or more) energy to space than it receives from the sun, causing global warming (or cooling). Processes that respond to the changing surface temperature and in turn affect the radiation budget are called climate feedbacks (Figure 1.5, see also Schneider and Dickinson 1974). Positive feedbacks amplify the initial imbalance, and negative feedbacks act to reduce the imbalance and reestablish equilibrium. The total feedback of the climate system is negative, such that a finite forcing does not cause runaway climate change but leads to a new equilibrium at a different global mean temperature. However, the exact strength of the feedback parameter is unknown - in other words, it is not known how much exactly the climate will warm in response to a given forcing (Arrhenius 1896; IPCC 2013).

In the global mean, the dominant negative feedback is the Planck feedback, which corresponds to the increase in outgoing longwave radiation caused by vertically uniform warming of the surface and the troposphere. In the tropics, the upper troposphere warms more than the surface. This leads to a greater increase in outgoing radiation for a given amount of surface warming, i.e. a negative lapse-rate feedback, which also dominates the global mean lapse-rate feedback. A warmer atmosphere contains more water vapour, which is an important greenhouse gas, leading to further warming (positive water vapour feedback). Cloud changes in reaction to a changing surface temperature can locally increase or reduce warming, but the global cloud feedback is likely positive. Finally, the surface area covered by snow and ice is reduced in a warming climate, and more solar radiation is absorbed at the surface (surface albedo feedback).

The Arctic is warming faster than the rest of the planet in both observations and climate model experiments. This Arctic amplification of climate change is also found in temperature reconstructions of past climates, including both ice ages and warmer periods in the Earth's more distant past (Barron 1983; Dahl-Jensen et al. 1998). The Intergovernmental Panel on Climate Change's Fifth Assessment report (IPCC AR5) primarily mentions the surface albedo feedback as playing an important role in causing

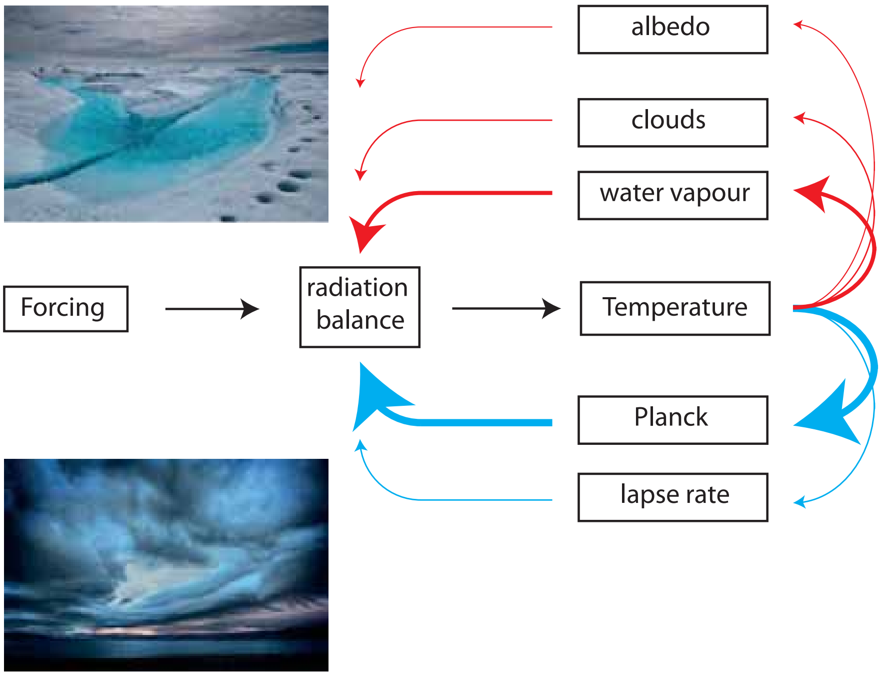
albedo
clouds
water vapour
Forcing
radiation balance
Temperature
Planck
lapse rate

Figure 1.5: Radiative forcing, feedback mechanisms and surface temperature change. Arrow thicknesses are scaled according to the globally averaged strength of each feedback process in MPI-ESM following Block and Mauritsen (2013). Image credits: melt stream by Ian Joughin, Creative Commons via EGU, clouds by stuckincustoms, Creative Commons via flickr

polar amplification (IPCC 2013). The report further mentions that 'other feedbacks including water vapour and cloud feedbacks have been suggested to be important amplifiers of Arctic climate change.' Temperature feedbacks (the lapse-rate and Planck feedbacks) are not mentioned explicitly, but a paper by Bintanja et al. (2011) discussing the effect of stratification on Arctic amplification is referenced without further discussion. Atmospheric and oceanic heat transport have also been thought to contribute to Arctic amplification. More recent results suggest that the zonal mean poleward energy transport reacts to differential warming caused by local feedbacks rather than driving it. Arctic warming in both observations and climate model results peaks in fall and winter, and the AR5 suggests that this 'strongly links Arctic amplification to feedbacks associated with the seasonal reduction in sea-ice extent and duration, as well as the insulating effect of sea ice in winter'. On the other hand, Bintanja and van der Linden (2013) suggest that only a quarter of the 21st century Arctic winter warming is caused by heat released by the ocean, and attribute the remainder to atmospheric processes.

Despite a relatively broad literature on feedbacks contributing to Arctic amplification, few studies have quantified and compared different feedback processes across a range of climate models. These studies were often limited by the use of regression methods based on longwave and shortwave fluxes routinely included in climate model output (e.g. Winton 2006; Crook et al. 2011). Such methods accurately account for the changes in either type of radiation but cannot disentangle the effects of individual physical processes related e.g. to changes in clouds or water vapour. Chapter 2 of this thesis therefore uses and extends the radiative kernel method (Soden et al. 2008) to quantify the contributions of individual feedback processes to Arctic amplification in climate models participating in the fifth phase of the Coupled model intercomparison project (CMIP5). I thereby intend to place into perspective the many processes that have been suggested to contribute to Arctic amplification.

Several studies have attempted to attribute the inter-model spread in Arctic amplification to specific processes (e.g. Holland and Bitz 2003; Winton 2006; Boé et al. 2009). If a main reason for models differing from each other can be convincingly identified, this provides a good basis to focus research efforts on improving the model representation of that process. Many present initiatives to investigate cloud processes and cloud feedbacks are indeed motivated by the fact that clouds are one of the key uncertainties causing models to produce different global mean warming responses for the same forcing. Linking future model behaviour to observable present-day quantities may be even more attractive - it is often hoped that such a correlation can help to constrain future projections to a much narrower range. However, in data sets as large as the CMIP archives, many variables correlate to a high degree of statistical significance by pure chance, and non-independent outcomes and variables may further distort the statistics. In chapter 3, I investigate a claim that CMIP3 models with strong present-day temperature inversions have lesser Arctic amplification, implying that the ensemble would underestimate true Arctic amplification. In this case, the investigated variables were affected by a statistical artifact of self-correlation that caused a seemingly significant but indeed spurious dependence.

1.2 Inversions, mixed-phase clouds and surface fluxes in the Arctic boundary layer

Because radiative cooling dominates over the absorption of solar radiation at high latitudes, the Arctic surface is often colder than its lower atmosphere (Figure 1.3). Such temperature inversions reduce the vertical fluxes of momentum, heat and moisture and thereby play an important role in the positive Arctic lapse-rate feedback. The inversions also interact closely with the widespread Arctic stratus clouds (Sedlar et al. 2012). Understanding the temperature and humidity structure of the lower Arctic atmosphere is thus an important basis to understanding Arctic climate change. Climate models poorly represent these structures (Medeiros et al. 2011), and we yet need to understand how the typical temperature and humidity inversions develop and decay.

Progress in understanding and modelling the Arctic boundary layer has long been hindered by the scarcity of in-situ and even remote-sensing observations. To overcome this barrier, the Canadian Coast Guard icebreaker 'Des Grosseilliers' was deployed into a region of thick sea ice north of Alaska in 1997/1998 for the Surface Heat Budget of the Arctic experiment (SHEBA) (Uttal et al. 2002). For an entire year, the crew made continuous observations of the sea-ice and snow surface, surface fluxes, atmospheric properties and clouds. The expedition obtained the possibly first full annual cycle of observations of temperature inversions in the central Arctic ocean, and observations of clouds containing both cloud liquid water and ice occurring throughout the year (Tjernström and Graversen 2009).

During winter, the boundary layer at the SHEBA site was found to be in either of two distinct states: A cloudy state, where cloud liquid water was present, surface radiative cooling was small or absent and temperature inversions were weak, and a radiatively clear state with no cloud liquid water, substantial surface radiative cooling and stronger temperature inversions. The states have been linked to varying large-scale conditions, but their occurrence has not been explained conceptually to date. In Chapter 4, a model experiment first conceived in the 1930s is used to understand the development of both states (Wexler 1936; Curry 1983).

The experiment represents a relatively warm and moist air mass that is advected into the Arctic in winter and cools radiatively (Figure 1.6). Elevated temperature inversions are first created by the warm air mass being advected over a cold surface. Radiative cooling leads to saturation of the air mass and triggers the formation of a cloud that

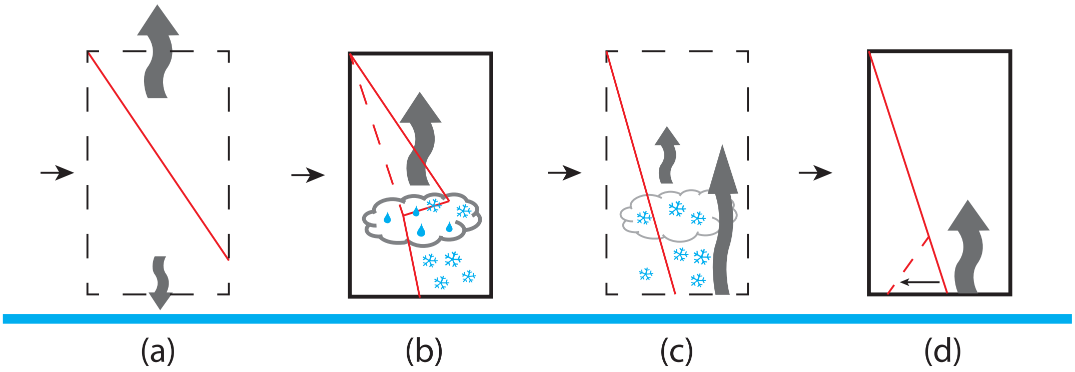

Figure 1.6: Sketch of the formation of Arctic air masses.

initially contains both liquid water and ice. This leads to the development of a well-mixed layer below the cloud and a maximum of radiative cooling near cloud top. As long as the interplay of radiative cooling, condensation and freezing of cloud droplets and gravitation-driven sedimentation of cloud ice sustains a mixed-phase cloud, the boundary layer remains in the cloudy state and surface radiative cooling is near zero. When cloud liquid water disappears, the boundary layer transits into a radiatively clear state, where the surface cools radiatively, and thus a stable boundary layer and strong surface-based temperature inversions begin to grow. We use this conceptual understanding to investigate the reasons for substantial climate model biases in typical wintertime inversion strength and surface fluxes.

About two decades after the SHEBA experiment, new intensive observation campaigns of the Arctic are being planned to further advance our understanding of the processes controlling Arctic weather and climate and their impacts on lower latitudes (WWRP 2014). Challenging the limits of what can be deduced and understood from currently available observations and investigating the main reasons for models to diverge from each other and from observations will be crucial to accurately direct those research efforts towards the places, times and variables or processes of which new high-quality observations will enable the largest possible leap forward in investigating the Arctic.

1.3 Stable boundary layers and the large-scale circulation

When the Arctic boundary layer transitions from the cloudy to the clear state, the surface begins to cool radiatively. The boundary layer becomes stably stratified, i.e. the potential temperature of air increases and therefore its density decreases with increasing distance from the surface. In a stably stratified boundary layer, the sensible heat flux is directed towards the surface. Turbulent mixing is produced by wind shear, but the density gradient caused by the stratification limits the size of turbulent eddies and thereby the amount of mixing. Correctly representing the fluxes of heat and momentum in stable boundary layers is crucial for obtaining realistic surface fluxes and near-surface temperatures, but current weather and climate models still struggle to meet this challenge.

An idealised case of a stable boundary layer developing over Arctic sea ice was run in both single-column models and Large-Eddy Simulations (LES) in the GABLS1 experiment (Beare et al. 2006; Cuxart et al. 2006). The single-column version of a climate model like ECHAM runs the physical parametrisation of local processes such as boundary-layer turbulence for a prescribed large-scale state. LES resolve the larger eddies containing the bigger share of turbulent energy, and are therefore expected to give a relatively accurate picture of the turbulent fluxes. The GABLS1 experiment showed that most operational models substantially overestimate surface drag and boundary-layer depth under stable stratification.

It is not too difficult to adjust a turbulence scheme in order to reproduce the LES results for an idealised setup like GABLS1, but more than a decade after the experiment was launched, world-leading operational centres still struggle to reduce the diffusivity of stable boundary layers to realistic values (Sandu et al. 2013). Neither have many climate modelling centres re-assessed or amended their turbulence parametrisation to yield more realistic profiles and surface fluxes. This is also true for ECHAM and the new Max Planck Institute Earth system model ICON, both of which are using a turbulence scheme that has not been changed since the early 1990s. Two obstacles render it so difficult to reduce the surface drag in general circulation models to a range consistent with observations and Large-Eddy Simulations. First, the role of surface drag for the large-scale circulation is not well understood. Enhanced surface drag as evident in many operational models has been shown to weaken synoptic high- and low-pressure systems. However, for reasons that are yet to be understood, models often produce more realistic large-scale pressure fields and circulations with exaggerated than with realistic surface drag. Secondly, many other parametrisations have over the time been adapted to produce a realistic climate while interacting with a - possibly biased - boundary-layer scheme. Making the boundary-layer scheme more realistic may now expose such compensating errors rather than improving the modelled climate. As more emphasis is being placed on projections of future circulation changes and therefore on climate models' ability to reproduce present-day circulation patterns, understanding the links between surface drag and the large-scale circulation becomes a more pressing challenge.

When the Earth's surface is heated by solar radiation, turbulent mixing drives the growth of a convective boundary layer. A growing convective boundary layer incorporates or entrains parcels of warmer free-tropospheric air at its upper boundary. ECHAM's current boundary-layer scheme does not reproduce this important characteristic of a dry convective boundary layer. The purely local computation of diffusivity virtually shuts down turbulence at and above the inversion layer which caps a dry convective boundary layer. Such a lack of dry entrainment affects boundary-layer structure and clouds in a numerical weather prediction model, and is likely to be a problem in the context of climate modelling as well (Beljaars and Viterbo 1998).

The turbulence scheme currently used in ECHAM was originally developed taking into account that in the limit of neutral stratification, the diffusivity constants for the turbulent transport of heat and momentum differ (Louis 1979). However, in its current implementation into ECHAM, the ratio between the diffusivities for momentum and heat called the turbulent Prandtl number is assumed to be equal to one in the surface layer. To what extent this assumption impacts the modelled climate is a question that yet has to be addressed.

Chapter 5 of this thesis tackles the scientific and model development problems of implementing more realistic boundary-layer schemes in climate models. A new turbulence scheme is implemented into the current version of ECHAM. The new model version ECHAM-TTE produces surface drag within the range of LES results for the GABLS1 case and substantially overestimates large-scale pressure gradients and zonal winds. Subgrid-scale orographic drag is enhanced to avoid this bias. The sensitivity of global model results to changes in the neutral Prandtl number is also investigated.

Chapter 2

Temperature feedbacks dominate Arctic amplification in CMIP5 climate models

Climate change is amplified in the Arctic in past warm (Barron 1983) and glacial (Dahl-Jensen et al. 1998) climates, historical observations (Chapman and Walsh 1993; Bekryaev et al. 2010) and climate model experiments (Manabe and Wetherald 1975; Holland and Bitz 2003)(Figure 2.1). Although a wide range of feedback mechanisms has been suggested to contribute to Arctic amplification, the increased absorption of solar radiation due to retreating snow and ice is often understood to be the main contributor (Serreze and Francis 2006; Screen and Simmonds 2010; Crook et al. 2011; Taylor et al. 2013). Yet, Arctic amplification is also found in models without snow and ice changes (Hall 2004; Graversen and Wang 2009), and has been shown to be primarily caused by feedbacks affecting terrestrial longwave radiation, i.e. temperature, water vapour and longwave cloud feedbacks, rather than feedbacks affecting solar shortwave radiation (Winton 2006). Here, we show that weaker Arctic temperature feedbacks (Manabe and Wetherald 1975; Bintanja et al. 2012) are the largest contributors to Arctic amplification in climate models: Surface warming leads to a smaller increase in the energy radiated to space in the Arctic because of 1) the vertical structure of warming and 2) the smaller increase of emitted blackbody radiation at colder temperatures. The weak Arctic temperature feedback is most pronounced in the cold season and roughly doubles wintertime warming.[1]

A quantitative understanding of the physical mechanisms underlying Arctic amplification is key to developing confidence in and constraining model projections of Arctic climate change, and to focusing research efforts and model-data comparisons on the most important processes. It is well established that Arctic amplification is in part caused by retreating sea-ice or snow-covered areas in a warming climate leading to an increase in the absorption of solar radiation at the surface (surface albedo feed-

---

[1] This chapter has been published as: Pithan, F. and T. Mauritsen, 2014: Arctic amplification dominated by temperature feedbacks in contemporary climate models, *Nature Geoscience* 7, 181-184

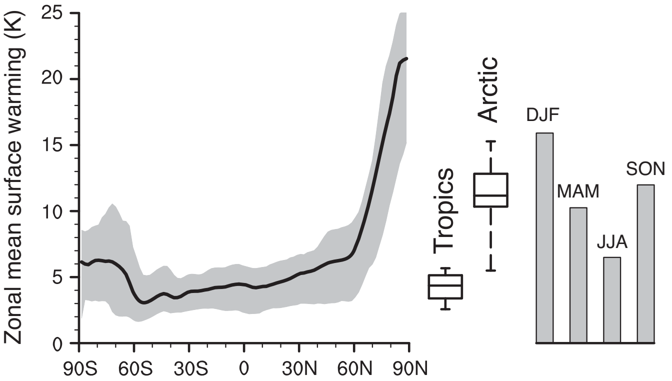

Figure 2.1: Arctic amplification in CMIP5 models. (left) Zonal mean surface temperature change for the last 30 years of the CMIP5 4xCO$_2$ experiment compared to the last 30 years of the control run. Boxes show the median (lines), 25th to 75th percentiles (boxes) and full spread (whiskers) of temperature change averaged over the tropics (30°S to 30°N) and the Arctic (60°N to 90°N), and bars (right) show the inter-model mean warming for different seasons. Inter-model mean warming is 11.2 K in the Arctic and 4.3 K in the tropics. Arctic warming is strongest in winter (15.9 K) and weakest in summer (6.5 K).

back)(Arrhenius 1896; Manabe and Wetherald 1975; Hall 2004). While the IPCC's fourth assessment report (AR4) stated that it was not clear whether the surface albedo feedback was the main cause of Arctic amplification (IPCC 2007), many recent studies indicate or assume that surface albedo feedback is the main cause (Serreze and Francis 2006; Screen and Simmonds 2010; Crook et al. 2011; Taylor et al. 2013). On the other hand, Arctic amplification does occur in models without surface albedo feedback (Hall 2004; Graversen and Wang 2009), and Arctic amplification in coupled climate models has been shown to be primarily caused by feedbacks acting on terrestrial longwave radiation (Winton 2006). The latter implies that the surface albedo feedback, which changes the absorption of solar shortwave radiation, can only play a secondary role in causing Arctic amplification. Important contributions to Arctic amplification have been suggested to result from the water vapour feedback caused by the greenhouse effect of additional water vapour (Graversen and Wang 2009), the cloud feedback due to changes in the effect of clouds on the earth's radiative balance (Vavrus 2004) and the lapse-rate feedback associated with the vertical structure of warming (Manabe and Wetherald 1975; Bintanja et al. 2012). Changes in atmospheric (Manabe and Wetherald 1980) and oceanic heat transport (Khodri et al. 2001; Holland and Bitz 2003; Spielhagen et al. 2011) are also thought to contribute to Arctic amplification.

The direct impact of rising temperatures on outgoing longwave radiation at the top of atmosphere (TOA) (temperature feedback) can be decomposed into a contribution from vertically uniform warming of the surface and troposphere (Planck feedback) and a contribution from tropospheric warming that deviates from the vertically uniform profile (lapse-rate feedback). The lapse-rate feedback connected to the vertical structure of atmospheric warming is known to contribute to stronger Arctic than tropical warming (Manabe and Wetherald 1975; Bintanja et al. 2012). In the tropics, air parcels rising in deep convective clouds create a tight coupling between surface and upper-tropospheric temperatures. In a warming climate, these air parcels release more latent heat, steepening the moist adiabatic lapse rate and thus causing greater warming in the upper troposphere than at the surface. Under this top-heavy warming profile, a smaller increase in surface temperatures is required to offset a given TOA imbalance. In the Arctic, cold dense air close to the surface is hardly mixed with the lighter air aloft, leaving radiation as the primary coupling mechanism. Radiative coupling does not impose a certain lapse rate, and surface-based warming remains confined to the lowermost parts of the atmosphere. Under this bottom-heavy warming profile, a larger increase in surface temperatures is required to offset a given TOA imbalance. The lapse-rate feedback is therefore negative in the tropics and positive in the Arctic.

The Planck feedback is generally overlooked as a contributor to Arctic amplification, even though the underlying physics are well established (Planck 1901). The longwave radiation emitted by the earth's surface rises with temperature following $R = \epsilon\sigma T^4$, where ϵ is the surface emissivity close to unity and σ the Stefan-Boltzmann-constant. Thus, a given increase in emitted radiation requires a larger temperature increase at colder background temperatures. For example, at 30 °C, an external forcing of 1 Wm^{-2} can be balanced by a 0.16 °C warming, whereas at -30 °C a 0.31 °C warming is required to balance the same forcing. Since the Arctic is colder than the tropics, the Planck feedback in itself causes Arctic amplification.

The local temperature change required to offset the radiative imbalance caused by a given forcing or feedback corresponds to that mechanism's warming contribution. We assess individual contributions to Arctic amplification as the difference between contributions to Arctic and tropical warming (Figure 2.2). Beyond the simple example quoted above, and accounting for the effects of atmosphere and clouds, the radiative flux change at the surface and TOA associated to a known surface temperature change can be computed from radiative kernels (Soden et al. 2008). We here invert the kernel method to compute the feedbacks' local warming contributions. The contribution of the Planck feedback's spatial structure to the spatial structure of warming is estimated as the difference between the warming response for a globally averaged and for the local Planck feedback (see methods).

Based on a conventional decomposition of feedbacks using top-of-atmosphere fluxes (Figure 2.2a), the largest contributor to Arctic amplification is the lapse-rate feedback,

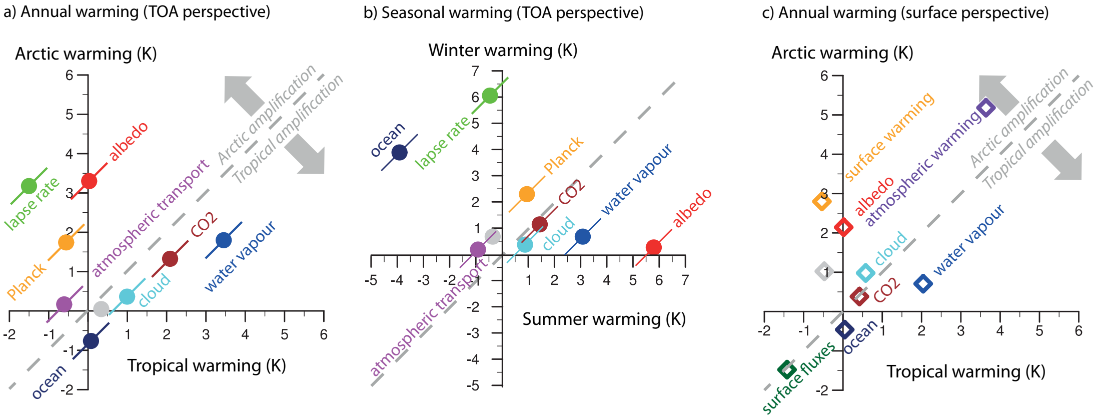

Figure 2.2: Warming contributions of individual feedback mechanisms. a) Arctic versus tropical warming from a TOA perspective b) Arctic winter versus summer warming c) Arctic versus tropical warming from a surface perspective. For a) and c), Feedbacks above the 1:1 line contribute to Arctic amplification, while feedbacks below the line oppose Arctic amplification. Gray is the residual error of the decomposition. Ocean includes the effect of ocean transport changes and ocean heat uptake.

followed by the surface albedo and Planck feedbacks. Although in absolute terms, the surface albedo feedback contributes slightly more to Arctic warming, the lapse-rate feedback additionally reduces tropical warming and therefore makes a greater contribution to Arctic amplification, as can be inferred from the distance to the 1:1 line. The water vapour feedback and CO_2 radiative forcing both lead to greater warming in the tropics, opposing Arctic amplification (Zhang et al. 1994; Hansen et al. 1997).

Instead of considering warming and moistening of the atmosphere as separate feedback mechanisms, they can be understood as one feedback caused by warming at constant relative humidity, plus a small feedback accounting for changes in relative humidity (Held and Shell 2012). This feedback decomposition assigns only a slightly larger contribution to Arctic amplification to the alternative lapse-rate feedback (Arctic: +3.8 K, tropics: -2.2 K) than to the surface albedo feedback (Arctic: +5.7 K), whereas the effect of the alternative Planck feedback on Arctic amplification is close to zero. In the fixed relative humidity framework, the contributions of the temperature-moisture and the surface albedo feedback to Arctic amplification are thus of roughly equal importance.

Arctic warming is stronger in winter (DJF) than summer (JJA). The strong winter warming has been linked to the release of heat stored in the ocean and to increases in downwelling longwave radiation (Bintanja and van der Linden 2013), but a quantitative understanding of the seasonal cycle of individual feedback mechanisms is lacking. From a TOA perspective, the surface albedo and water vapour feedbacks contribute to stronger summer warming but are outweighed by seasonal heat storage in the ocean and the lapse-rate feedback (Figure 2.2b). Seasonal heat storage in the ocean, including latent heat of melting sea ice, mitigates about two thirds of the summertime effect of surface albedo change. Heat from the ocean is released to the atmosphere in winter, which in combination with the positive lapse-rate feedback causes the well-known pattern of winter-amplified Arctic warming. In summer, when atmospheric stability is much weaker than in winter, the Arctic lapse-rate feedback is actually slightly negative.

Surface temperature change can be readily understood through TOA fluxes if the troposphere is essentially well-mixed and changes in the tropospheric temperature profile follow simple physical principles, such as the steepening of the moist adiabat in a warmer climate (Hansen et al. 1997). These assumptions do not hold in the Arctic, where a positive lapse-rate feedback represents a decoupling between surface and troposphere. The TOA-based feedback decomposition is thus internally consistent, but somewhat unsatisfying from a physical point of view, because the Arctic lapse-rate feedback reflects the breakdown of an assumption of vertical coupling rather than a specific physical mechanism. By analysing feedbacks at the surface in addition to the TOA, we can further understand what causes the surface amplification of Arctic warming reflected in the lapse-rate feedback (Figure 2.2c).

At the surface, the temperature feedback can be decomposed into a negative surface warming feedback (longwave radiation emitted from the surface) and a positive atmospheric warming feedback corresponding to the downwelling longwave radiation received by the surface. The largest contribution to Arctic amplification arises from the surface temperature feedback and is due to the smaller increase in longwave emissions per unit of warming at colder temperatures. This non-linear dependence of blackbody emissions on temperature plays a greater role from a surface than a TOA perspective because the meridional temperature gradient at the surface is larger than that in the troposphere. The atmospheric temperature feedback contributes to Arctic amplification because the near-surface atmosphere warms more in the Arctic than the tropics. Previous studies decomposing Arctic feedbacks from a surface perspective (Taylor et al. 2013) used a methodology that implicitly includes the spatial structure of the temperature feedback, and therefore did not identify the key role of the surface temperature feedback's structure for Arctic amplification.

In the annual mean, cloud feedback opposes Arctic amplification from a TOA perspective, but makes a small contribution to Arctic amplification from a surface perspective. Within the lowest 1-2 km of the Arctic atmosphere, cloud-top temperatures are often similar to surface temperatures (Serreze et al. 1992). Under these circumstances, low-level clouds hardly affect TOA longwave fluxes because the clouds radiate upwards at roughly the same temperature as the surface, but increase downward longwave radiation and thus warm the surface at the expense of the atmosphere. An increase or

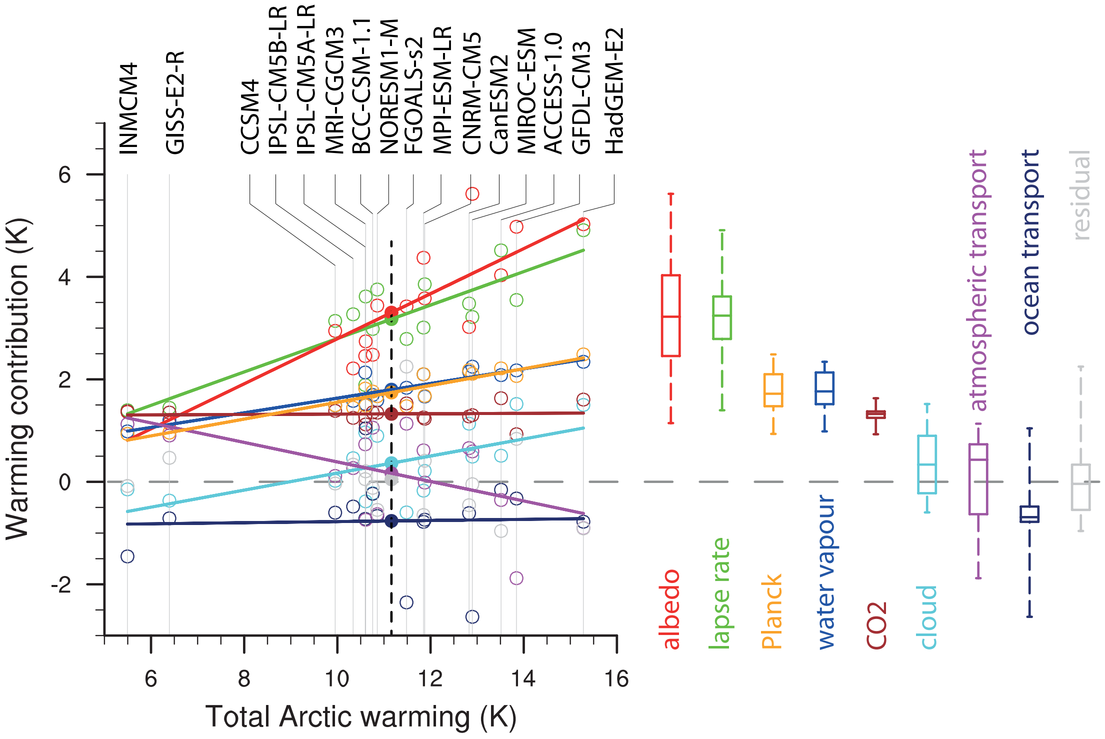

Figure 2.3: Inter-model spread of Arctic warming (left) Arctic warming contributions of feedbacks vs. total Arctic warming in individual models. Lines are linear regressions of feedback contributions against total Arctic warming. Filled circles on the black vertical line represent the ensemble mean. (right) Spread of Arctic warming contributions in the analysed models. Boxes show the median, 25th and 75th percentiles and whiskers the full ensemble spread.

thickening of such clouds in a warming climate as predicted by models hardly affects cloud feedback from a TOA perspective, but causes a positive cloud feedback at the surface. Likewise, the water vapour feedback contributes more to summer than winter warming from a TOA perspective, but has a stronger contribution to surface warming in winter than in summer (not shown) (Soden et al. 2008).

Besides quantifying the different contributions to Arctic amplification in the ensemble mean, it is valuable to understand why models differ in their degree of Arctic amplification (Holland and Bitz 2003). Our analysis shows that inter-model spread in Arctic warming is dominated by the spread in local feedback mechanisms, not meridional transport changes (Figure 2.3). Changes in atmospheric heat transport dampen inter-model spread because they are more positive in models with little Arctic warming. This is consistent with results from an energy-balance model used to reconstruct warming and transport changes in CMIP3 models (Hwang et al. 2011). In the ensemble mean, atmospheric heat transport does contribute to Arctic amplification by enhancing Arctic and reducing tropical warming (Figure 2.2a). Contrary to physical intuition, poleward atmospheric energy transport does not scale with the meridional temperature gradient within individual models, but increases in a majority of models despite a reduction in the equator-to-pole temperature gradient. Increasing latent energy transports overcompensating the decrease of dry static energy transport have been shown to cause such behaviour of climate models (Manabe and Wetherald 1980; Held and Soden 2006). Changes in ocean transport and ocean heat uptake are not correlated with total Arctic warming across different models.

To develop confidence in model projections of future Arctic warming, it is necessary to quantitatively understand the role of different physical mechanisms for Arctic amplification. Contrary to a widespread assumption, temperature feedbacks are the most important contributors to Arctic amplification in contemporary climate models. The surface albedo feedback is the second main contributor, while other suggested drivers of Arctic amplification either play minor roles or even oppose Arctic amplification in the ensemble mean.

2.1 Methods

Prior studies analysing the role of different feedbacks for Arctic amplification have often diagnosed feedbacks based on TOA and surface fluxes routinely included in climate model output (Winton 2006; Crook et al. 2011; Bintanja and van der Linden 2013). These methods provide a precise assessment of longwave and shortwave flux changes, but cannot quantify the temperature changes associated to individual feedback mechanisms. In the present study, we use and extend the radiative kernel technique (Soden et al. 2008) to overcome this limitation.

A radiative kernel k_i is the change in TOA radiation ΔR_i caused by a small change in the climate variable x_i, e.g. a one percent change in surface albedo (dx_i): $k_i = \frac{dR}{dx_i}$. The TOA flux change caused by one feedback in a climate change experiment can be estimated as $\Delta R_i = k_i \cdot \Delta x_i$, where Δx_i is for instance the surface albedo change between the control and perturbed climate. We use this established technique to compute the flux change caused by each feedback, and extend the method to convert flux changes into temperature responses associated with each feedback.

The warming response to a TOA flux imbalance is decomposed into three components: A global mean Planck feedback, the local deviation from the global mean Planck feedback and the effect of the lapse-rate feedback, i.e. deviations from vertically uniform warming, on surface temperature change

$$\Delta T = \sum_i \left(\Delta R_i \left(\overline{\frac{dT}{dR}} + \frac{dT}{dR}' + \frac{dT}{dR}^{LR} \right) \right). \tag{2.1}$$

The warming contribution e.g. of the surface albedo feedback is

$$\Delta T_a = \Delta R_a \left(\overline{\frac{dT}{dR}}\right), \tag{2.2}$$

and the contribution of the Planck feedback's deviation from its global mean is

$$\Delta T_P = \sum_i \left(\Delta R_i {\frac{dT}{dR}}'\right). \tag{2.3}$$

The local warming contribution of the lapse-rate feedback is

$$\Delta T_{LR} = \sum_i \left(\Delta R_i {\frac{dT}{dR}}^{LR}\right). \tag{2.4}$$

The warming response to a unit flux imbalance is the inverse of the vertically integrated temperature kernel, $\frac{dT}{dR} = \frac{1}{\int k_T dp}$, which we obtain by summing over the surface temperature kernel and all levels of the tropospheric temperature kernel. By averaging across latitudes and longitudes, we decompose this into the mean inverted kernel and a local deviation. To obtain the full warming response including the effect of the lapse-rate feedback, each level is weighted by its warming relative to surface warming when vertically integrating the temperature kernel $\int k_{T,weighted} = k_{Ts} + \int k_{Tl} \cdot \frac{\Delta T_l}{\Delta T_s} dp$.

In the surface-based feedback analysis, the inverted surface temperature kernel alone is used to compute the warming response, while atmospheric temperature change is treated as a feedback contributing to the surface flux imbalance. The surface temperature response is separated into a global mean component and the local deviation analogous to the Planck feedback

$$\Delta T = \sum_i \left(\Delta R_{s,i} \left(\overline{\frac{dT_s}{dR_s}} + {\frac{dT_s}{dR_s}}'\right)\right) \tag{2.5}$$

Atmospheric heat convergence is computed as the difference between TOA and surface fluxes, assuming no storage of heat in the atmosphere on the timescale of the experiment. Changes in oceanic heat convergence and ocean heat uptake, which are non-zero on the timescale considered, are computed as changes in total surface fluxes. To separate tropospheric and stratospheric responses, we assume a tropopause height of 100 hPa in the tropics (30°S to 30°N) decreasing linearly with latitude to 300 hPa at the poles. We use surface downward and upward shortwave fluxes to compute the effective albedo. Monthly mean data from the last 30 years of the CMIP5 pre-industrial control and 4xCO$_2$ runs are averaged into monthly climatologies for the feedback calculations. Radiative kernels were obtained from the MPI-ESM-LR control climate (Block and Mauritsen 2013). Using kernels from the 4xCO$_2$ runs leads to a smaller role of the albedo feedback (Block and Mauritsen 2013), and using kernels from other models (Soden et al. 2008) leads to larger residuals but does not qualitatively change the conclusions of the present study.

Chapter 3

Statistical artifacts in ’Current GCM’s unrealistic negative feedback in the Arctic’ by Boé et al.

Abstract

Contrasting our expectation of a positive lapse-rate feedback associated with the Arctic inversion, Boé et al. (2009) report that strong present-day Arctic temperature inversions are associated with stronger negative longwave feedbacks and thus reduced Arctic amplification in the CMIP3 model ensemble. We find that the relation between longwave feedbacks and inversion strength is an artifact of statistical self-correlation and that shortwave feedbacks have a stronger correlation with inter-model spread. We conclude that the conventional understanding of a positive lapse-rate feedback associated with the Arctic inversion is consistent with the CMIP3 model ensemble.[1]

3.1 Introduction

Arctic amplification of climate change is a consistent feature of observations (Serreze and Barry 2011), palaeoclimate reconstructions (Masson-Delmotte et al. 2006) and climate model simulations (Holland and Bitz 2003). Mechanisms believed to play a role in Arctic amplification include the surface albedo, cloud and water vapour feedbacks, atmospheric and oceanic heat transport and the atmospheric lapse-rate feedback (Serreze and Barry 2011). In this comment, we discuss the impact of temperature inversions on radiative feedbacks in the Arctic and show that physically unexpected correlations between present-day inversion strength and longwave feedbacks reported by Boé et al. (2009) are largely caused by a statistical artifact.

The total longwave feedback discussed by Boé et al. (2009) is composed of the Planck, lapse-rate, water vapour and cloud feedbacks, the sum of the Planck and lapse-rate feedbacks being the total temperature feedback. Since the supposed effect discussed by Boé et al. (2009) pertains to the clear-sky feedback, we omit to further discuss cloud feedbacks in this specific context. The negative Planck feedback corresponds to the increase in outgoing longwave radiation (OLR) caused by a vertically uniform warming. It dominates the total longwave and combined longwave and shortwave feedback and is the main cause of the Earth's climate coming to a new equilibrium after an external forcing is applied.

---

[1] This chapter has been published as: Pithan, F. and T. Mauritsen, 2013: Comments on ’Current GCM’s unrealistic negative feedback in the Arctic’, *J. Climate*, 26(19), 7783-7788

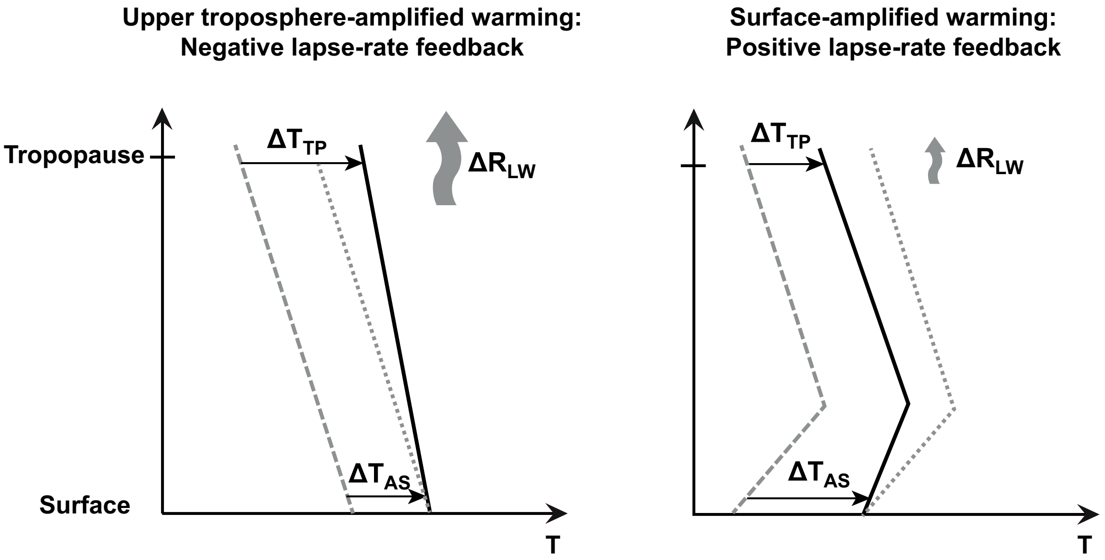
Upper troposphere-amplified warming:
Negative lapse-rate feedback
Surface-amplified warming:
Positive lapse-rate feedback
Tropopause
Surface
ΔT_TP
ΔR_LW
ΔT_AS
T
ΔT_TP
ΔR_LW
ΔT_AS
T

Figure 3.1: Conceptual picture of a negative lapse-rate feedback in the tropics (left) and a positive lapse-rate feedback in the Arctic (right).

The second part of the temperature feedback is the lapse-rate feedback: Warming in the Arctic is stronger at the surface than in the troposphere, in part due to the stably stratified Arctic atmosphere that tends to trap heat near the surface. In contrast, moist deep convection in the tropics keeps the atmospheric temperature profile close to a moist adiabat and therefore leads to a stronger warming in the upper troposphere than at the surface. The stronger Arctic warming at the surface leads to a positive feedback, since the OLR at the top of the atmosphere (TOA) increases less than it would in the case of a vertically uniform warming (Figure 3.1). Strong atmospheric stability is therefore understood to lead to a positive lapse-rate feedback in the Arctic, whereas moist deep convection in the tropics leads to a regionally negative lapse-rate feedback (Figure 3.2). This concept of atmospheric stability in the Arctic contributing to Arctic amplification was developed in early modelling studies by Manabe and Wetherald (1975) and Held (1978) and has recently been discussed by Bintanja et al. (2012).

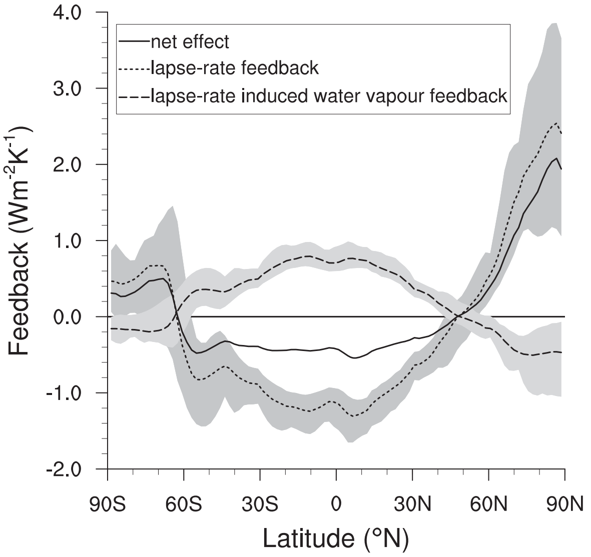

Figure 3.2: Zonal mean lapse-rate induced feedbacks in the 4xCO_2 experiments of nine CMIP5 models (shaded areas) and inter-model mean (black lines). The lapse-rate feedback is defined as the TOA response to the deviation of warming from a vertically uniform profile. The lapse-rate induced water vapour feedback is defined as the effect of this deviation on the water vapour feedback assuming constant relative humidity. The net effect of the deviation of warming from a vertically uniform profile is the sum of these two feedbacks. The feedbacks have been computed using radiative kernels from Block and Mauritsen (2013) applied to the temperature difference between the last 30 years of the perturbed and control experiments. Using radiative kernels from Soden et al. (2008) or Shell et al. (2008) results in similar meridional structures (not shown).

The water vapour feedback is due to the enhanced atmospheric emissivity of a warmer and thus moister atmosphere. It is globally positive, but can be negative in the Arctic boundary layer where atmospheric temperatures are higher than surface temperatures and hence a moister, more emissive atmosphere yields an increase in OLR (Soden et al. 2008).

Arctic temperature inversions thus cause both a regionally positive lapse-rate and locally negative water vapour feedback. Their total impact on feedbacks depends on the balance of these two effects. While it should be noted that the global-mean lapse-rate feedback and associated water vapour feedback of opposed sign roughly cancel (Held and Shell 2012), the regional balance of these effects is the determining factor here. In CMIP5 models, the positive lapse-rate feedback in the Arctic is several times greater than the negative water vapour feedback induced by lapse rate changes (Figure 3.2). Previous studies using both global models (Manabe and Wetherald 1975; Held 1978; Bintanja et al. 2012) and 1D radiative-transfer models (Bintanja et al. 2011) have concluded that the total impact of Arctic temperature inversions on feedbacks is positive.

Contrasting this understanding, Boé et al. (2009) report that in the CMIP3 model results, strong inversions are associated with a stronger negative longwave feedback which leads to weaker Arctic amplification. In the next section, we summarise the methodology used and the results obtained by Boé et al. (2009). We then discuss the problem of self-correlation and analyse how it affects the results, especially regarding the respective roles of the longwave and shortwave feedbacks in causing inter-model spread in Arctic warming.

3.2 Feedback analysis

The analysis of Boé et al. (2009) is based on a regional feedback framework using ocean mixed-layer temperatures instead of the conventional surface air temperatures. The feedback factor is defined as

$$\lambda = \frac{\Delta R}{\Delta T_{OC}}, \tag{3.1}$$

ΔT_{OC} being the change in vertically averaged potential temperature of the uppermost 70 m of the ocean and ΔR the change in TOA radiation in response to the forcing. All values are annual means for the region north of 70°N and changes are differences between the period 1900-1949 of the historical runs and the period 2150-2199 of the SRES A1B runs.

Within this feedback framework the longwave feedbacks ($\lambda_{LW} = \Delta R_{LW}/\Delta T_{OC}$) have a correlation of $r = 0.78$ with ocean temperature change (ΔT_{OC}) across all analysed models. This correlation is stronger than that of the shortwave feedbacks with ΔT_{OC} and almost as strong as the correlation between the sum of the feedbacks and

Arctic warming (0.81, Column 3 in Table 3.1). From this, Boé et al. (2009) conclude that 'a large part of the spread of Arctic climate change is explained by the longwave feedback parameter'. Boé et al. (2009) also find a near-perfect negative correlation ($r = -0.96$) between λ_{LW} and the ratio of atmospheric to oceanic temperature change, concluding that this ratio named temperature feedback factor 'is a crucial contributor to the uncertainties of Arctic climate change'. The inverse of this ratio is in turn found to correlate well with modelled present-day inversion strength. This line of reasoning lead to the conclusion that strong inversions in GCMs are associated with a stronger negative longwave feedback, posing a challenge to the conventional understanding of the lapse-rate feedback in the Arctic.

It should be noted that the use of ocean temperatures is crucial for obtaining a correlation between Arctic warming and inversion strength - no such correlation is found when using the conventional metric of surface air temperature change (Figure 3.3).

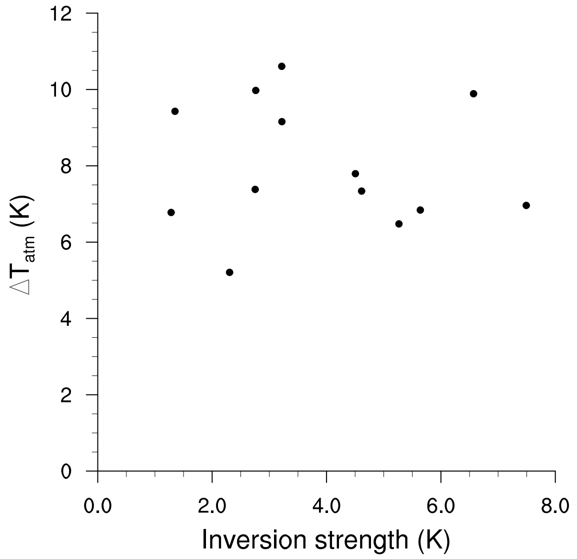

Figure 3.3: Present-day inversion strength and Arctic warming measured as surface air temperature change. Inversion strength is computed as 1960-1999 mean using the same definition as Boé et al. (2009).

3.3 Statistical artifacts from self-correlation

When plotting a feedback defined as $\frac{\Delta R}{\Delta T}$ against ΔT, the common term in the independent and the dependent variable causes a statistical self-correlation (Pearson 1896).

This effect can produce artificial, albeit apparently statistically significant correlations even for perfectly random datasets (Kenney 1982). To estimate the effect of self-correlation on results Klipp and Mahrt (2004) suggested to create randomised datasets with the same statistical moments as the original data by permuting the original values of the variables. The correlation obtained when repeating the original analysis using the randomised variables can be used as a measure of self-correlation in the analysis. Here we perform the described permutation test using the CMIP3 data presented by Boé et al. (2009).

The correlation between ΔT_{OC} and λ_{LW} obtained by Boé et al. (2009) can be easily reproduced from the randomised datasets. This is illustrated in Figure 3.4, where the upper panel shows the change in OLR against ocean temperature change for the original and randomised data and the lower panel shows the apparent correlation between temperature change and longwave feedbacks. The randomised datasets align as well as the original data.

The correlation coefficients obtained by Boé et al. (2009) can be compared to the average correlation coefficient obtained from a large number of randomised datasets generated as described above (Table 3.1). Here we permute ocean temperatures, but use the correct longwave and shortwave radiation changes from each model when randomising the sum of both feedbacks ($\sum \lambda_i$). The probability p that the correlation coefficient obtained from a randomised dataset exceeds r_{data} is computed as the fraction of all randomised datasets in which the correlation exceeds that in the original data. The null hypothesis is that two analysed variables are uncorrelated and the probability p corresponds to the level of significance of a given correlation. Table 3.1 shows these probabilities and the correlation coefficients for the sum of the feedbacks ($\sum \lambda_i$) as well as for the shortwave (λ_{SW}) and longwave feedbacks (λ_{LW}) separately.

Table 3.1: Correlations presented by Boé et al. (2009) compared with randomised data from 10000 permutations.

X-Axis	Y-Axis	r_{data}	$\bar{r}_{random}$	$p(r_{random} > r_{data})$
$\sum \lambda_i = \frac{\Delta R_{LW} + \Delta R_{SW}}{\Delta T_{OC}}$	ΔT_{OC}	0.81	0.62	0.02
$\lambda_{LW} = \frac{\Delta R_{LW}}{\Delta T_{OC}}$	ΔT_{OC}	0.78	0.73	0.18
$\lambda_{SW} = \frac{\Delta R_{SW}}{\Delta T_{OC}}$	ΔT_{OC}	-0.51	-0.64	0.05
$\frac{\Delta T_{AS}}{\Delta T_{OC}}$	$\lambda_{LW} = \frac{\Delta R_{LW}}{\Delta T_{OC}}$	-0.96	-0.97	

The analysis confirms that the correlations of the randomised datasets are close to

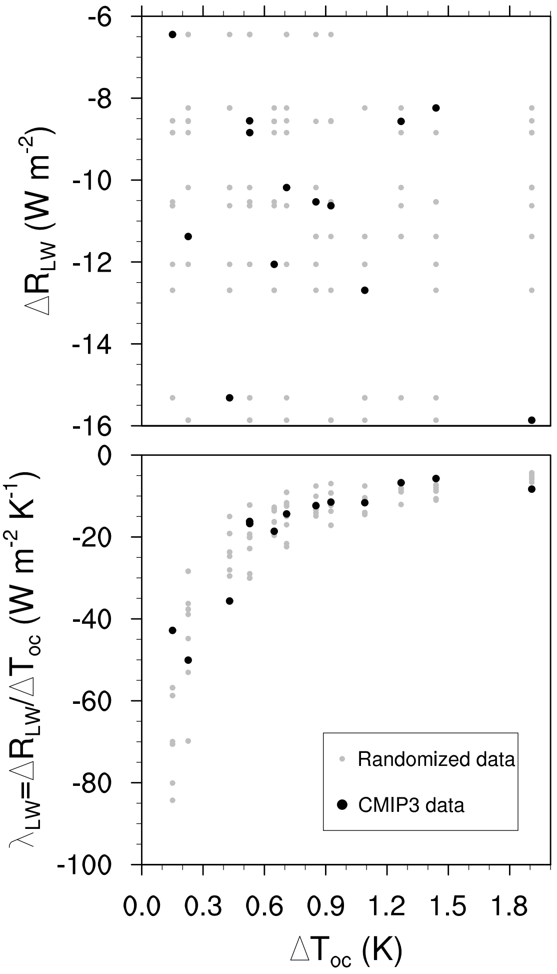

Figure 3.4: Comparison of correlations between the CMIP3 data and ten randomised datasets with the same statistical properties as the original data.

those obtained from the CMIP3 dataset. The average correlation between longwave feedbacks and ocean warming from the randomised datasets is 0.73 compared to 0.78 for the original data, and 18 percent of the randomised datasets have higher correlations than the original data. Therefore, no correlation between ΔT_{OC} and λ_{LW} that is significant to the 0.05 level can be inferred from the CMIP3 model results. Further, the near-perfect correlation between $\lambda_{LW} = \Delta R_{LW}/\Delta T_{OC}$ and $\Delta T_{AS}/\Delta T_{OC}$ can be partly attributed to self-correlation. The variables ΔR_{LW} and ΔT_{AS} are less strongly correlated ($r = -0.63$), but when dividing both ΔR_{LW} and ΔT_{AS} by randomly permuted values of ΔT_{OC}, we obtain practically the same correlation as using the original data (-0.97 vs. -0.96).

Boé et al. (2009) dismiss shortwave feedbacks as important contributors to the inter-model spread in Arctic amplification because the correlation with ΔT_{OC} is smaller than that of the longwave feedbacks, and further the correlation is negative (-0.53), which is physically not to be expected. However, the average correlation for randomised datasets is even more negative (-0.64), indicating that the true correlation between shortwave feedbacks and ocean warming is indeed positive, as we physically expect. Less than five percent of the randomised datasets have a correlation greater than -0.51, which means that the correlation between the shortwave feedbacks and ocean warming is significant to the 0.05 level. In agreement with our analysis, Winton (2006) reports that the most important cause of inter-model spread in Arctic amplification between twelve CMIP3 models are the non-surface albedo shortwave feedbacks caused by clouds and water vapour.

The permutation test shows that the strong correlations between ΔT_{OC} and λ_{LW} and between λ_{LW} and $\Delta T_{AS}/\Delta T_{OC}$ can be largely attributed to statistical self-correlation. This also affects the correlation between feedbacks and sea-ice cover change (ΔSIC), since ΔSIC and ΔT_{OC} are strongly correlated ($r = -0.87$, Fig. 9 in Boé et al. (2009)). The correlation between shortwave feedbacks and the inter-model spread in Arctic ocean warming is statistically significant, but the correlation between longwave feedbacks and warming is not, i.e. the magnitude and sign of the correlation coefficients are dominated by self-correlation and do not accurately reflect physical relationships.

3.4 Discussion and conclusion

Boé et al. (2009) argued that strong temperature inversions in the Arctic were associated with stronger negative longwave feedbacks in the CMIP3 model results, challenging our physical understanding of a positive lapse-rate feedback associated with stable stratification in the Arctic atmosphere. Their argument is based on correlations in the CMIP3 results linking the longwave feedback to the ratio of atmospheric to oceanic warming, which in turn is related to the inversion strength.

Randomly permuting the data shows that both the correlations between Arctic ocean warming (ΔT_{OC}) and longwave feedbacks (λ_{LW}) and between λ_{LW} and the ratio of Arctic surface air temperature change to ocean temperature change ($\Delta T_{AS}/\Delta T_{OC}$) can be explained as statistical artifacts caused by self-correlation. When self-correlation is taken into account, we find that no robust relationship between ΔT_{OC} and λ_{LW} can be inferred from the CMIP3 data and that shortwave feedbacks have a positive correlation with inter-model spread in Arctic warming that is significant to the 0.05 level. Hence, we cannot confirm a statistical link between strong present-day inversions and strong negative longwave feedbacks in the CMIP3 data.

Radiative transfer calculations with idealised atmospheric profiles at fixed relative humidity have shown that the presence of an inversion reduces the increase in OLR for a given increase in near-surface air temperatures (Bintanja et al. 2011). These calculations also show that warming in the boundary layer has a smaller impact on OLR than warming at higher levels in the troposphere. We further show that in the Arctic, the positive lapse-rate feedback dominates over the negative lapse-rate induced water vapour feedback in CMIP5 models.

The relatively stronger surface warming for models with strong temperature inversions reported by Boé et al. (2009) does therefore not give rise to a specific negative feedback - it is the response of the climate system to the positive feedback associated with the inversion: In the presence of an inversion, the radiative cooling to space is less efficient and more heat is retained near the ground, which causes additional surface warming (Manabe and Wetherald 1975). The resulting amplified warming eventually leads to an increase in OLR that restores the radiative energy balance. We conclude that the conventional understanding of a positive lapse-rate feedback associated with the Arctic inversion is consistent with the CMIP3 model ensemble and supported by current physical evidence.

Chapter 4

Mixed-phase clouds cause climate model biases in Arctic wintertime temperature inversions

Abstract

Temperature inversions are a common feature of the Arctic wintertime boundary layer. They have important impacts on both radiative and turbulent heat fluxes and partly determine local climate-change feedbacks. Understanding the spread in inversion strength modelled by current global climate models is therefore an important step in better understanding Arctic climate and its present and future changes. Here, we show how the formation of Arctic air masses leads to the emergence of a cloudy and a clear state of the Arctic winter boundary layer. In the cloudy state, cloud liquid water is present, little to no surface radiative cooling occurs and inversions are elevated and relatively weak, whereas surface radiative cooling leads to strong surface-based temperature inversions in the clear state. Comparing model output to observations, we find that most climate models lack a realistic representation of the cloudy state. An idealised single-column model experiment of the formation of Arctic air reveals that this bias is linked to inadequate mixed-phase cloud microphysics, whereas turbulent and conductive heat fluxes control the strength of inversions within the clear state.[1]

4.1 Introduction

With temperatures rising faster than the global mean, a fast retreat in summertime sea-ice cover and increasing mass loss of glaciers and ice sheets, the Arctic climate system is undergoing profound changes (ACIA 2004). Arctic processes have important implications for global climate through the formation of deep waters that sustain the oceanic meridional overturning circulation (e.g. Jungclaus et al. 2005), atmospheric connections to mid-latitude weather and climate (e.g. Honda et al. 2009; Francis and Vavrus 2012) and climate feedbacks possibly relevant on the global scale. Understanding Arctic climate and climate change therefore remains an important challenge.

---

[1] This chapter has been published as: Pithan, F., B. Medeiros and T. Mauritsen, 2013: Mixed-phase clouds cause climate model biases in Arctic wintertime inversion strength, *Climate Dynamics*, doi: 10.1007/s00382-013-1964-9

This paper aims to better understand Arctic temperature inversions and their representation in climate models. We combine CMIP5 model output and observational data with an idealised single-column model (SCM) experiment of the formation of Arctic air masses to investigate the processes that lead to the emergence and decay of temperature inversions. We find that low-level mixed-phase clouds play a key role in setting the surface fluxes and inversion strength, and many models struggle to represent these clouds at low temperatures.

Temperature inversions have important implications for the amplitude and sign of radiative and turbulent surface heat fluxes (Bintanja et al. 2011) as well as the mechanical coupling between surface and atmosphere and thus sea-ice drift (Overland and Guest 1991). When the climate warms, the stable stratification of the atmosphere in the presence of temperature inversions acts to trap additional heat near the surface and thus contributes to a stronger warming near the surface than in the upper troposphere (Manabe and Wetherald 1975). This vertical structure of Arctic warming causes a regionally positive lapse-rate feedback, because less warming in the upper troposphere leads to a smaller increase in outgoing longwave radiation compared to a vertically uniform warming. A smaller increase in outgoing radiation means that more surface warming is required to balance TOA fluxes and reach a steady state (Figure 4.1, see also Held 1978).

Temperature inversions have been reported to be a typical feature of the Arctic atmosphere since some of the earliest scientific explorations of the Arctic (Sverdrup 1933). Analysing radiosonde data from land-based and drifting stations, Serreze et al. (1992) found that the frequency, depth and strength of wintertime temperature inversions increased from the Norwegian Sea to the east, where cloud cover is reduced and anticyclonic conditions become dominant. Temperature inversions were present in almost all soundings taken over one year for the Surface Heat Budget of the Arctic experiment (SHEBA) in pack ice north of Alaska (Tjernström and Graversen 2009), with more than half of the observed inversions being surface-based in winter (DJF), while elevated inversions with a near-neutral mixed layer close to the surface dominated in spring and summer. Inversion strengths retrieved from satellite observations compare favourably with radiosonde stations at southern high latitudes and have also been used to extend our picture of Arctic temperature inversions (Gettelman et al. 2006; Pavelsky et al. 2011). Humidity inversions, i.e. specific humidity rising with altitude, are also common in Arctic boundary layers (Curry 1986; Devasthale et al. 2011).

Interactions between radiation and cloud condensate play an important role for

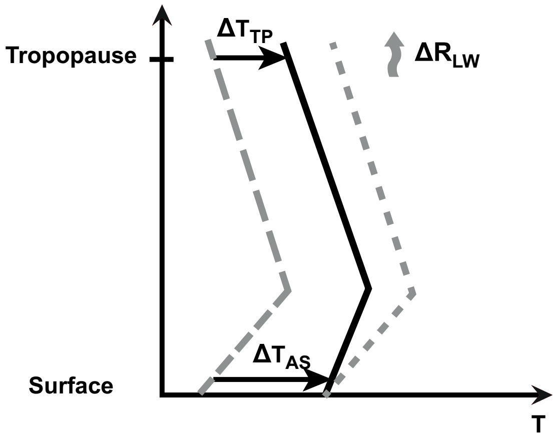

Figure 4.1: Stronger warming at the surface than in the middle and upper troposphere leads to a positive lapse-rate feedback in the Arctic. Figure: Pithan and Mauritsen (2013) ©American Meteorological Society

boundary-layer development and inversion strength, as was already noted by Sverdrup (1933). Observations from the SHEBA campaign (Persson et al. 2002) revealed two preferred states of the Arctic wintertime boundary layer: A radiatively clear state characterised by strong longwave cooling under ice clouds or clear skies and a cloudy state with low-level mixed-phase clouds and little to no longwave cooling at the surface (Persson et al. 1999; Stramler et al. 2011). These states display distinct turbulent and conductive heat fluxes as well as vertical temperature structures with stronger, surface-based inversions occurring in the clear state and weaker, usually elevated inversions in the cloudy state (Figure 4.2).

Arctic stratiform mixed-phase clouds typically consist of one or several thin layers of supercooled liquid water at cloud top, with ice crystals within and below the liquid layer (Morrison et al. 2012). Liquid water is mostly formed in updrafts and to a minor extent in the inversion layer, while ice crystals are formed within the cloud, grow and are removed by sedimentation. The presence of ice can lead to a rapid depletion of cloud liquid water via the Wegener-Bergeron-Findeisen process (Wegener 1911; Bergeron 1935; Findeisen 1938), and it has been suggested that low in-cloud concentrations of ice nuclei limit ice formation and thus contribute to the persistence of Arctic mixed-phase clouds (Fridlind et al. 2012). Turbulent updrafts and their effect on cloud processes cannot be resolved in large scale models and thus need to be parametrised. Most climate models also have too coarse a vertical resolution to resolve the supercooled liquid layers, resulting in one model layer representing the mean properties of the liquid and ice cloud layers. It is therefore challenging to accurately represent thermodynamic properties and microphysical processes of mixed-phase clouds in climate models (Klein et al. 2009; Barrett 2012).

Arctic temperature inversions and associated near-surface variables are poorly represented in current climate models. Medeiros et al. (2011) analysed monthly-mean inversion strength across the models participating in the third phase of the Coupled Model Intercomparison Project (CMIP3), defining inversion strength as the difference between the 850 hPa and surface air temperature. Partitioning the data into land and ocean domains, they found a spread in typical inversion strengths on the order of 10 K, with many models overestimating stability over both land and sea ice. Their definition of inversion strength deviates from the textbook definition of an inversion as a layer of air where temperatures rise with altitude, but gives a robust estimate of the bulk stability of the lower troposphere consistent with the coarse vertical resolution of climate models. We therefore adopt the same definition for analysing low-level stability as a proxy for inversion strength in model and reanalysis data throughout this paper. Turbulent fluxes at the surface are closely linked to the temperature structure and stability of the lower troposphere and also display a large spread in climate models. Medians of monthly mean turbulent heat fluxes over Arctic sea ice in winter range from -15 to +15 $\mathrm{W m^{-2}}$ across different CMIP3 models, and the spread in net longwave radiative fluxes is of the same magnitude (Svensson and Karlsson 2011).

The present study aims to understand the intermodel spread at the level of individual physical processes. Temperature inversions at high latitudes are a consequence of radiative cooling at the surface and advection of warmer air masses from lower latitudes (Zhang et al. 2011). To understand these processes, we use an idealised single-column experiment building on earlier studies by Wexler (1936) and Curry (1983). These studies show that radiative cooling, its interaction with cloud condensate and warm air advection are crucial not only for the development of temperature inversions but also that of the entire boundary layer and the surface heat budget in Arctic winter. Both Wexler (1936) and Curry (1983) refer to the radiative cooling of warmer air masses from maritime sources as formation of continental polar air. Throughout this paper, we will refer to the same process as formation of Arctic air masses.

Our investigation begins with an analysis of the large-scale monthly mean low-level stability in climate models and its relationship to global climate based on the results of Medeiros et al. (2011) (Section 4.3). To understand what causes the spread and biases of low-level stability in models, we examine the processes governing the emergence of temperature inversions in Arctic winter. We show that the clear and cloudy states of the Arctic winter boundary layer correspond to different stages of the formation of Arctic air masses and analyse how low-level stability develops during this process (Section 4.4). Subsequently, observations of low-level stability for the clear and cloudy states of the boundary layer are compared to the sub-daily output of CMIP5 models

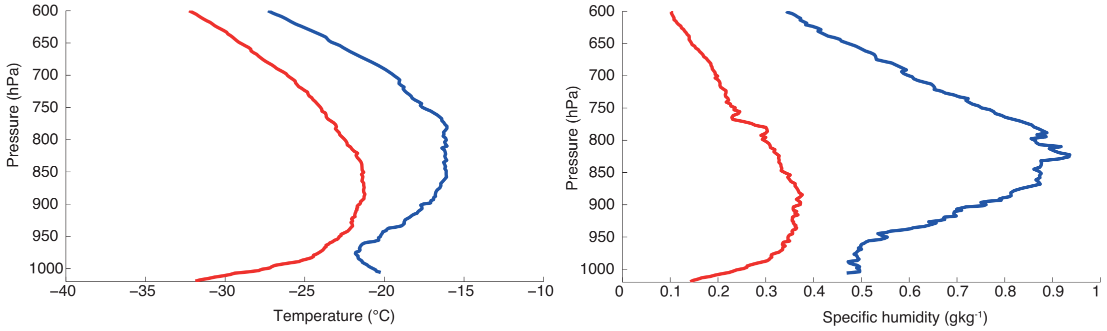

Figure 4.2: Median vertical structures of temperature and humidity in the clear (red) and cloudy (blue) boundary layer observed NDJF during SHEBA. Redrawn following Stramler et al. (2011) using a threshold of -10 $\mathrm{W m^{-2}}$ of surface net longwave radiation to separate the two states.

(Section 4.5). Finally, we test the sensitivity of an idealised SCM experiment of Arctic air formation to different model parametrisations in order to relate biases in global models to individual processes (Sections 4.5.1 and 4.5.2).

4.2 Models and data

Monthly mean atmospheric and near-surface air temperatures as well as sensible heat fluxes from the historical runs of a range of CMIP5 models (Table 4.1) and from the RCP8.5 runs for a subset of models based on data availability are used for the analysis of large-scale low-level stability and fluxes (Taylor et al. 2012). A more detailed analysis is carried out for the models for which we could obtain both atmospheric and near-surface temperatures and surface net longwave radiation at sub-daily resolutions. These models are listed alongside a brief characterisation of their mixed-phase cloud microphysics parametrisations in Table 4.2.

Observations made in multiyear pack-ice north of Alaska between October 1997 and October 1998 have been obtained from the SHEBA experiment (Persson et al. 2002). Standard meteorological observations and flux measurements were made on the ice floe, while atmospheric profiles were obtained from six- to twelve-hourly launches of radiosondes. We further use surface observations and radiosonde profiles from the Atmospheric Radiation Measurement (ARM) site in Barrow at the north coast of Alaska at 71.3°N 156.6°W (Xie et al. 2010).

We use reanalysis data from both the ERA-40 (Uppala et al. 2005) and the updated ERA-Interim dataset (Simmons et al. 2007). The two reanalyses use different versions of the European Centre for Medium-Range Weather Forecasts' integrated forecast system and different data assimilation schemes. Since all reanalyses rely on the assimilation of observations, results are less reliable for regions with scarce observational data such as the Arctic (e.g. Sorteberg et al. 2007). Given the lack of regular surface observations and soundings over the Arctic ocean, the reanalyses' vertical temperature profiles will strongly depend on satellite retrievals and the model used to derive the reanalysis. Tjernström and Graversen (2009) found a near-surface warm bias of about 1 K in ERA-40 compared to SHEBA data that persisted despite the assimilation of SHEBA observations into the reanalysis. Comparing ERA-40 first-guess values and final analyses for the SHEBA years and years without assimilated soundings, they concluded that assimilating the soundings reduced the near-surface warm bias by about 0.5 K. While this limitation should be considered when using reanalyses to evaluate climate models, Tjernström and Graversen (2009) suggest that ERA-40 somewhat underestimates typical inversion strengths, but properly captures the climatological characteristics of temperature inversions. We will show later that climate model biases are much greater than the likely error of the reanalysis, which justifies using the latter as approximation of the observational "truth".

4.2.1 Single-column models, forcing and initialisation

We use a single-column framework to model the cooling of an air mass advected from lower latitudes into the Arctic in winter (Wexler 1936; Curry 1983). By applying a Lagrangian perspective, i.e. following the trajectory of the air mass with the single-column model and assuming horizontal homogeneity, we devise an idealised setup to study the role of local processes. Large-scale advection of heat and moisture plays an important role in the formation and resilience of mixed-phase clouds and is the basis of our Lagrangian setup. We neglect the role of open leads which are sources of heat and moisture (Andreas et al. 2002).

Most experiments are run with the single-column version of ECHAM6, the atmosphere component of MPI-ESM (Stevens et al. 2013). We choose a vertical resolution of 47 layers as used in the CMIP5 runs with MPI-ESM-LR to be able to compare our SCM results to climate model output. The lowest level is located approximately 30 m above the ground and there are 10 levels within the lowest 3 km. Some experiments are repeated with the single-column version of the Community Atmosphere Model version 4 (CAM4, Gent et al. 2011), which is the atmosphere component of CCSM4.

The cloud microphysics scheme of ECHAM6 treats cloud water and cloud ice as separate prognostic variables, while rain and snow are diagnosed. Instantaneous homogeneous freezing of all cloud liquid water is assumed at temperatures below -35 °C, while stochastic heterogeneous and contact freezing occur at temperatures between 0 and -35 °C. Cloud ice may be transferred to lower levels or the surface through sedimentation, converted into snow by aggregation and accretion, and sublimated or melted.

Table 4.1: CMIP5 models used in this study

Model	Modelling centre
BCC-CSM1-1	Beijing Climate Center
BNU-ESM	College of Global Change and Earth System Science, Beijing Normal University
CanCM4	Canadian Centre for Climate Modelling and Analysis
CMCC-CM	Centro Euro-Mediterraneo per I Cambiamenti Climatici
CNRM-CM5	Centre National de Recherches Météorologiques
CSIRO-Mk3-6-0	Commonwealth Scientific and Industrial Research Organization
EC-EARTH	EC-EARTH consortium
FIO-ESM	The First Institute of Oceanography
FGOALS-s2	LASG, Institute of Atmospheric Physics
GFDL-CM3	NOAA Geophysical Fluid Dynamics Laboratory
GISS-E2-R	NASA Goddard Institute for Space Science
INMCM4	Institute for Numerical Mathematics
IPSL-CM5A-LR	Institut Pierre-Simon Laplace
IPSL-CM5B-LR	Institut Pierre-Simon Laplace
MIROC-ESM	Japan Agency for Marine-Earth Science and Technology
HadCM3	Met Office Hadley Centre
MPI-ESM-LR	Max Planck Institute for Meteorology
MRI-CGCM3	Meteorological Research Institute
CCSM4	National Center for Atmospheric Research
CESM1-CAM5	Community Earth System Model Contributors
NorESM1-M	Norwegian Climate Centre

Details of the scheme are described in Lohmann and Roeckner (1996).

The initial temperature profile represents an air mass in equilibrium with a near-freezing ocean surface. Temperature is prescribed as $T = T_0 \left(\frac{p}{p_0}\right)^{R\gamma g^{-1}}$ below 300 hPa and constant above that level, where $T_0 = 273\,\mathrm{K}$ and $p_0 = 1013\,\mathrm{hPa}$ are the surface temperature and pressure, $\gamma = 8 * 10^{-3}\,\mathrm{Km}^{-1}$ is the assumed lapse rate, $R = 287\,\mathrm{Jkg}^{-1}\mathrm{K}^{-1}$ the gas constant for air and g gravitational acceleration (Curry 1983). Relative humidity drops linearly with pressure from 80 percent at the surface to 20 percent at 600 hPa. A constant specific humidity of $3 * 10^{-6}$ is prescribed between 300 hPa and the model top. The model location is set to 70°N, initial sea ice thickness is 1 m and initial snow cover 0.1 m water equivalent. A geostrophic wind of $5\,\mathrm{ms}^{-1}$ is prescribed up to 300 hPa in order to drive moderate turbulent mixing. Large-scale advection of heat, moisture and momentum are set to zero. CO_2 concentration is set to the preindustrial value of 280 ppm. Surface temperatures are initialised at 250 K, the ocean underneath the ice is assumed to be at the freezing point of sea water (-1.9 °C). Surface temperatures, sea ice and snow properties are calculated interactively during the experiment. The model is started on 1 January and run for 20 days, leading to zero insolation throughout the experiment.

The qualitative results described in this study are robust to small changes in the initial and boundary conditions such as the initial surface temperature, initial temperature profiles and the prescribed geostrophic wind profile. Since the formation of clouds depends on the initial relative humidity profile, we prescribe a relative humidity quickly dropping off with increasing altitude to study low-level cloud processes over several days while avoiding high-level cloud formation.

Table 4.2: Overview of CMIP5 models providing high-frequency data. a)T_t: triple point, $\Delta T = 11.82\,\mathrm{K}$ b) $T_0 = -4\,^\circ\mathrm{C}$ over ocean and $-10\,^\circ\mathrm{C}$ over land.

CMIP model	Atmosphere	No. of layers	Reference	Computation of cloud ice fraction f
BCC-CM-1-1	BCC-AGCM 2.0.1	26	Wu et al. (2010)	Linear between -10 and -40
CMCC-CM	ECHAM5	31	Scoccimarro et al. (2011)	Explicit parametrisation of freezing processes between 0 and -35
CCSM4	CAM4	26	Gent et al. (2011)	Linear between -10 and -40
CNRM-CM5	Arpege-Climat 5.1	31	Météo France (2009)	No prognostic condensate, $f = 1 - exp\left\{\frac{-1}{2(\Delta T)^2}(T - T_t)^2\right\}$ ^{a}
GISS-E2-R	GISS ModelE	40	Schmidt et al. (2006)	T-dependent probability of freezing and Bergeron-Findeisen process $p_i = 1 - exp\left[-\left(\frac{T_0 - T}{12}\right)^2\right]$ ^{b}
GFDL-CM3	GFDL-AM3	48	Donner et al. (2011)	Explicit parametrisation of freezing processes between 0 and -30, almost no water at temperatures colder than -15
INMCM4	INMCM	21	Volodin et al. (2010)	$f = 1 - (0.0059 + 0.9941 \cdot exp(-0.003102T^2)$
IPSL-CM5A	LMDZ5A	39	Hourdin et al. (2012)	Linear between 0 and -15
MIROC-ESM	MIROC-AGCM	80	Watanabe et al. (2011)	$f = 1 - exp((-((268.91K - T)/12K)^2))$ above $-38\,^\circ\mathrm{C}$
MPI-ESM-LR	ECHAM6	47	Stevens et al. (2013)	Explicit parametrisation of freezing processes between 0 and -35
MRI-CGCM3	MRI-AGCM3	40	Yukimoto et al. (2012)	Explicit parametrisation of freezing processes, Bergeron-Findeisen process triggers full and immediate glaciation if ice water content $> 0.5\,\mathrm{mg\,kg}^{-1}$

4.3 Lower tropospheric temperature structure in CMIP5 models

We assess the typical temperature structure of the Arctic wintertime boundary layer and lower troposphere by analysing the area-weighted pdfs of monthly mean low-level stability over land and ocean from CMIP5 models and reanalyses (Figure 4.3). We obtain a similar bimodal distribution over the ocean domain as Medeiros et al. (2011) did for CMIP3 with a stable mode over sea ice and a near-neutral mode over open water. The distribution between the two modes essentially reflects the different sea-ice cover between models, and models do agree on the temperature structure of the near-neutral mode (-12 to -8 K) within a few Kelvin. Over the ocean, we will therefore focus on the stable mode that corresponds to the sea-ice covered Arctic ocean and contains the bulk of the inter-model spread.

Mean modelled low-level stability in the stable mode ranges from about 1.5 K to 13 K (Figure 4.4), while reanalyses give 4.1 (ERA-int) and 4.9 K (ERA40). Only five models produce weaker stability than the reanalyses, while 15 models produce stronger stability. The distribution of low-level stability over land is unimodal with a somewhat smaller intermodel spread (Figure 4.3b), mean modelled stability between 4.5 K and 11.5 K and reanalyses values of 7.1 (ERA40) and 7.5 K (ERA-int). Eight models display smaller and ten models larger stability than the reanalyses. In the reanalyses, mean low-level stability over land are 2 to 3 K stronger than over the ocean, while the difference is less than one K for most models. Five models display a difference of at least 2 K, and five other models display stronger stability over the ocean than over land.

Models with strong stability are underrepresented in the high-frequency output sample (Table 4.2), as can be seen in the distribution of dashed and solid lines in Figure 4.3. Reanalyses data should be used with caution because observational data over the Arctic ocean are limited to satellite irradiances and sporadic observational campaigns. If we assume the surface warm bias of up to 1.5 K detected in ERA40 compared to SHEBA observations (Tjernström and Graversen 2009) to be representative of the entire Arctic ocean and the whole time period considered, five models would fall within the range of realistic values, while ten models would still overestimate mean low-level stability. Since more soundings are available over land than over the Arctic ocean, the reanalysis bias over land could be smaller, leading to an overestimate of land-sea contrasts in low-level stability by the reanalysis.

Within an individual climate model, mean Arctic low-level stability is closely related to global mean temperature (Figure 4.5). Given the previously described amplification of Arctic warming near the surface, this relationship can be explained in simple terms. In a warming climate, the Arctic surface warms faster than air aloft, which leads to a weakening of temperature inversions and reduced low-level stability. This reduction

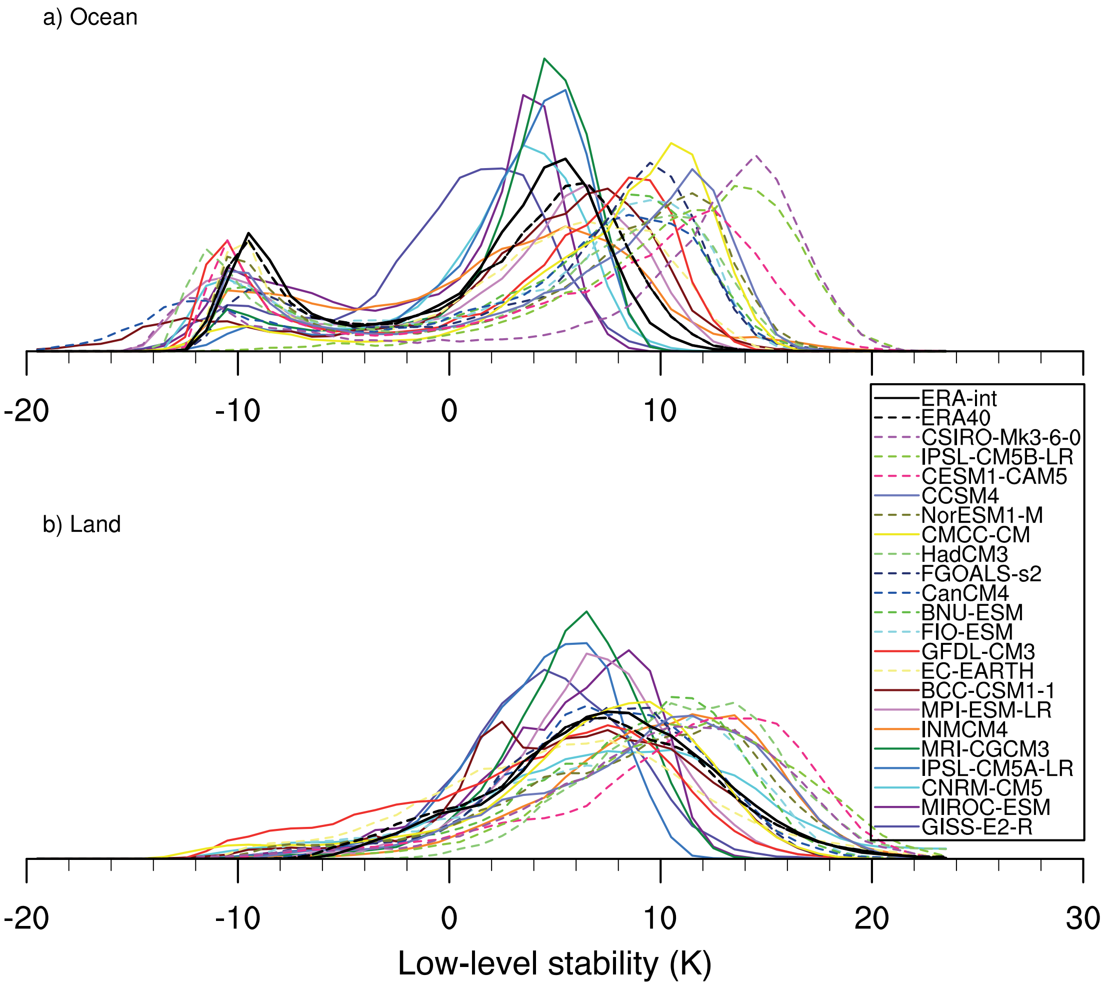

Figure 4.3: PDFs of NDJF Arctic (north of 64°N) monthly mean grid-point wise low-level stability in the historical runs, 1990-1999. Low-level stability is defined as 850 hPa temperature minus surface air temperature. The models' own land-sea masks have been used to partition data into land and ocean domains, considering any grid point with more than 20 percent land fraction as land. Models from Table 4.2 are displayed with solid lines.

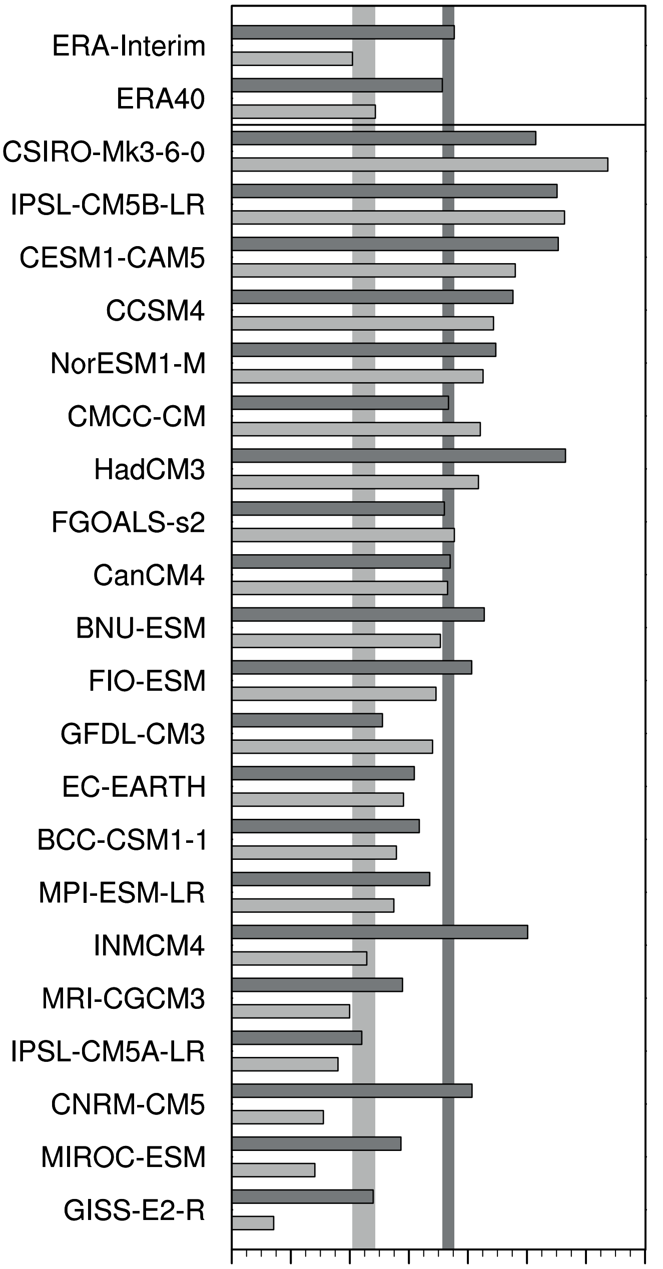

Figure 4.4: Mean low-level stability in the stable mode over the ocean (light grey) and over land (dark grey). Models are sorted by mean low-level stability in the stable mode over ocean. Modes are separated at the local minimum of the pdf for each model. Shaded areas mark the range of the reanalyses.

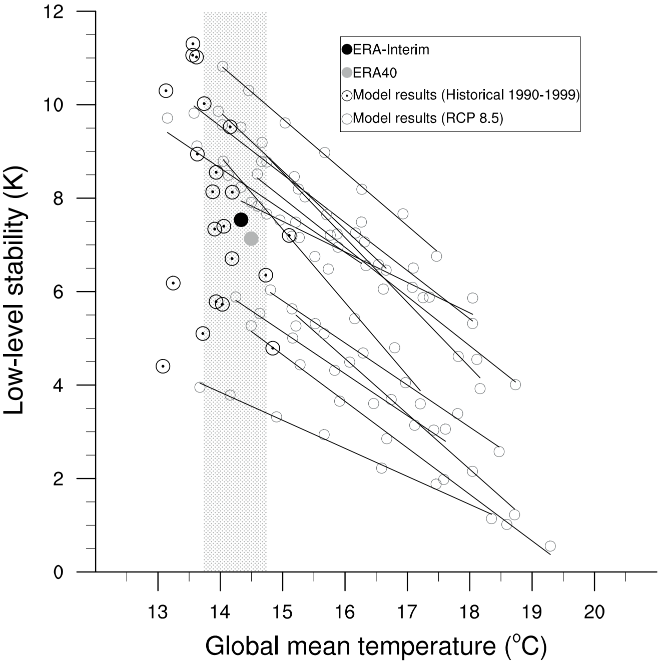

Figure 4.5: Mean low-level stability over land against global mean temperature in models and reanalyses. Lines show regressions within the RCP8.5 runs of a subset of models, black circles represent all CMIP5 model shown in Figure 4.4. The dotted area shows observed global mean temperatures and the associated uncertainty according to Jones et al. (1999).

of atmospheric stability and disappearance of temperature inversions is a prerequisite for deep convection over the Arctic ocean in winter, which has been suggested as a mechanism keeping the Arctic ocean free of winter sea ice in warm climates (Abbot and Tziperman 2008).

Since global mean temperatures are cold-biased in most climate models (Mauritsen et al. 2012), their relationship to Arctic low-level stability could in principle explain some of the overestimation relative to reanalyses of present-day stability noted before. However, Figure 4.5 shows that while the models with the strongest stability also tend to be cold-biased, this relationship cannot explain the bulk of the inter-model spread. To understand the spread of results, we thus need to investigate the local processes that control the emergence and strength of temperature inversions in Arctic winter.

4.4 The formation of Arctic air masses

Building on Wexler (1936) and Curry (1983), we investigate the formation of Arctic air by following a relatively warm and moist air mass from lower latitudes that is advected over cold Arctic sea ice. We model the air mass transformation in a SCM experiment as described in section 4.2.1.

Initially, an inversion is formed (Figure 4.7a) and the air mass cools to space and to the surface (Figure 4.6a). Radiative cooling leads to saturation of the air and the formation of liquid or mixed-phase clouds. Because the emissivity of these clouds is close to unity, radiative cooling now occurs in the cloud layer rather than at the surface, progressively eroding the inversion and reducing low-level stability (b). The cloud cools and is eventually transformed from a mixed-phase to a low-emissivity ice cloud, which allows the surface to cool radiatively (c). When the condensate has fallen out, strong surface cooling under a clear sky leads to the emergence and growth of a new surface-based temperature inversion (d). In the SCM experiment, (a) and (c) are unstable states in rapid transition to the quasi-stable state (b) or the stable state (d). Observations of both supercooled liquid water and ice clouds in the same temperature range indicate that the transition from a mixed-phase cloud (b) to an ice cloud (c) does not represent a threshold behaviour that occurs at a given temperature, but rather a regime shift in the dynamical interactions between cloud microphysics, cloud macrophysics and environmental conditions (Morrison et al. 2012). The formation of Arctic air leads to the formation of a humidity inversion (Figure 4.8) that is characteristic for the cloudy state of the boundary layer (Figure 4.2) because condensation begins near the surface and occurs at increasing altitudes as the boundary layer cools.

The first quasi-stable state (b) with little to no surface cooling in the presence of mixed-phase clouds corresponds to the cloudy state found in SHEBA observations,

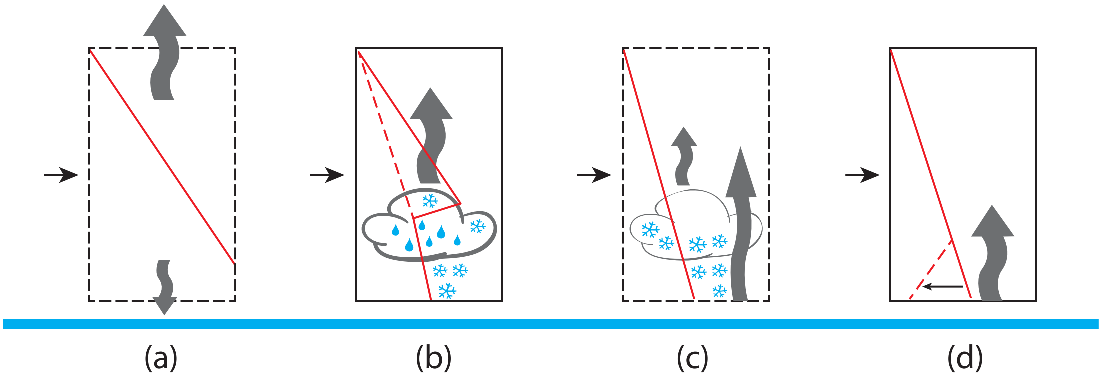

Figure 4.6: Sketch of the formation of Arctic air. Dashed boxes mark unstable transition states.

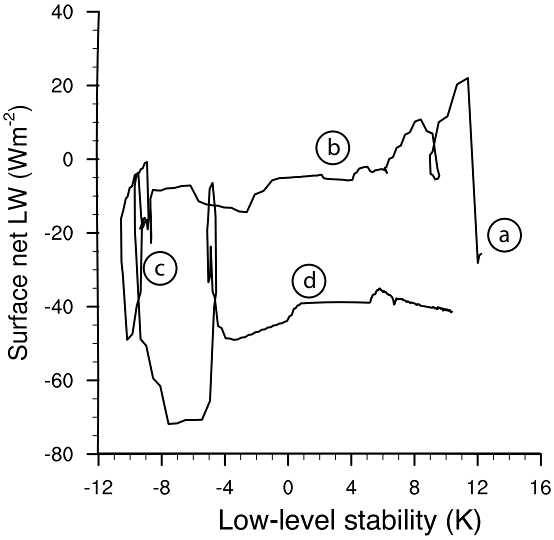

Figure 4.7: Trajectory of low-level stability against surface net longwave radiation in idealised SCM experiment of Arctic air formation (section 4.2.1), hourly averages.

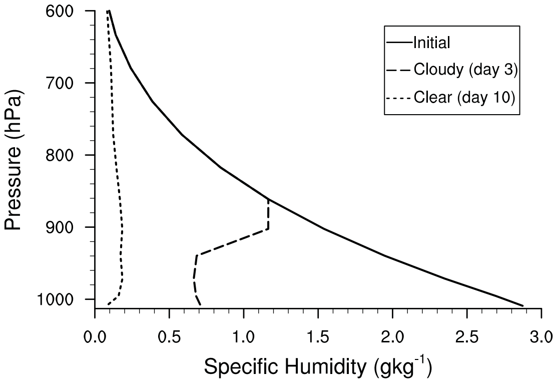

Figure 4.8: Profiles of specific humidity during the SCM experiment.

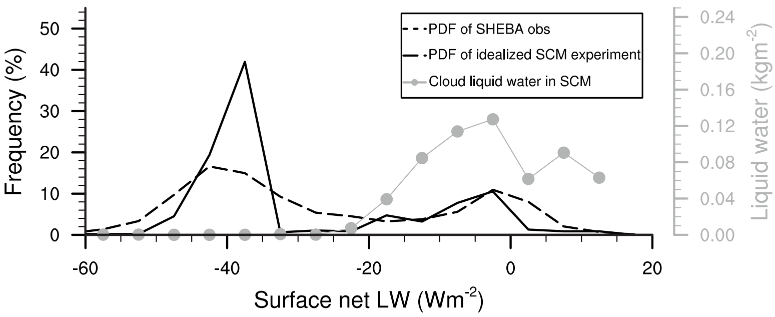

Figure 4.9: PDF of surface net longwave radiation during the formation of Arctic air in ECHAM6 SCM and observed NDJF at the SHEBA site. Both time series are hourly averages, bins are 5 Wm^{-2} wide. Grey circles denote cloud liquid water paths averaged for each bin.

while the second stable state (d) with strong longwave cooling in the absence of cloud liquid water corresponds to the clear state (Persson et al. 1999, 2002; Stramler et al. 2011). The occurrence of both states of the Arctic wintertime boundary layer is reflected in the bimodal distribution of surface net longwave radiation during the SCM experiment described in section 4.2.1 (Figure 4.9). Despite the highly idealised nature of the experiment, the location of the peaks matches those obtained from SHEBA observations. This indicates that the net surface longwave radiation in the two states of the Arctic winter boundary layer is an emergent property of the coupled surface-atmosphere system that is captured by the SCM, and largely independent of the actual temperatures and large-scale forcings. Note that since the SCM remains in the clear state at the end of the experiment, the relative weight of each peak depends on the duration of the model run and should not be compared to observations. The single-column experiment also reproduces the observed link between the presence of cloud liquid water and the occurrence of the cloudy state (Figure 4.9, Tjernström 2012). The mechanism described here is consistent with observations of Arctic air mass formation in northwestern Canada (Turner and Gyakum 2011), where cloud-top radiative cooling preceded clear-sky surface radiative cooling and the formation of surface-based temperature inversions.

Having established how temperature inversions develop and decay during the clear and cloudy states of the Arctic winter boundary layer, we proceed to analyse how the representation of these states affects mean low-level stability in global climate models.

4.5 The two states of the boundary layer in observations and CMIP5 models

Arctic wintertime inversions in the clear state of the boundary layer are typically stronger than in the cloudy state, as can be seen in ARM and SHEBA observations (Figure 4.10). Within the clear state, stronger stability corresponds to weaker longwave cooling. These observations are consistent with the processes outlined in the previous section and illustrated in Figure 4.6.

To determine to what extent the overestimation of mean low-level stability in models compared to reanalyses is caused by shortcomings in the representation of one or both states and by the distribution between the states, we analyse the distribution of low-level stability and surface radiative cooling in sub-daily output of CMIP5 models. While we cannot expect Arctic-wide model output to match point observations, models should represent the qualitative behaviour of a bimodal distribution with different stability between modes. Station output at high frequency would in principle allow for a closer comparison of model and observational data, but was only available for a few models.

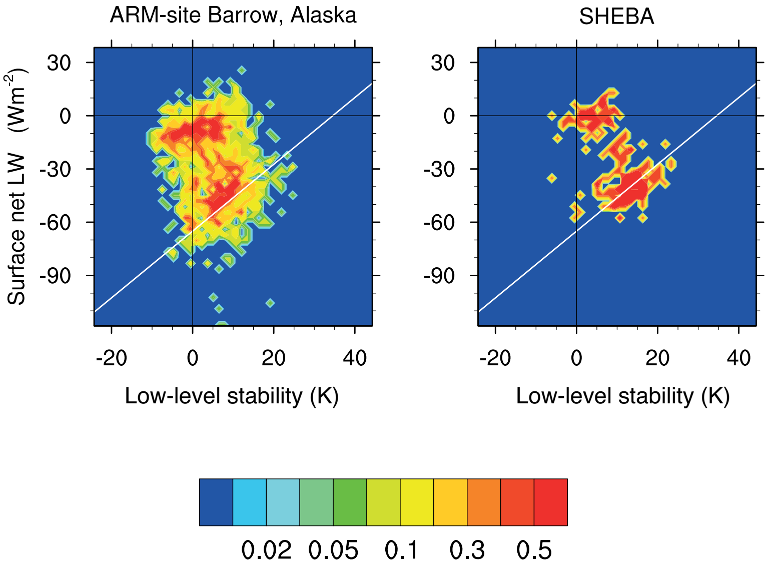

Figure 4.10: Bivariate pdfs of NDJF low-level stability and surface net longwave radiation from SHEBA observations (1997/1998) and the ARM site in Barrow (2000-2009). Low-level stability is defined as the temperature difference between the 850 hPa level and the near-surface air. Temperature measurements are for individual soundings while surface radiation measurements are 6-hourly averages. The pdf is constructed using 50 by 50 equally spaced bins ranging from -25 to 45 K for low-level stability and from -120 to 40 Wm^{-2} for net longwave radiation. The white line drawn across the plot serves as a visual reference and indicates a relationship between surface cooling and low-level stability with a Stefan-Boltzmann equation linearised around 240 K and assuming an effective atmospheric emissivity of 0.6. Both values are chosen to visually match the position and slope of the maximum density region in the pdfs.

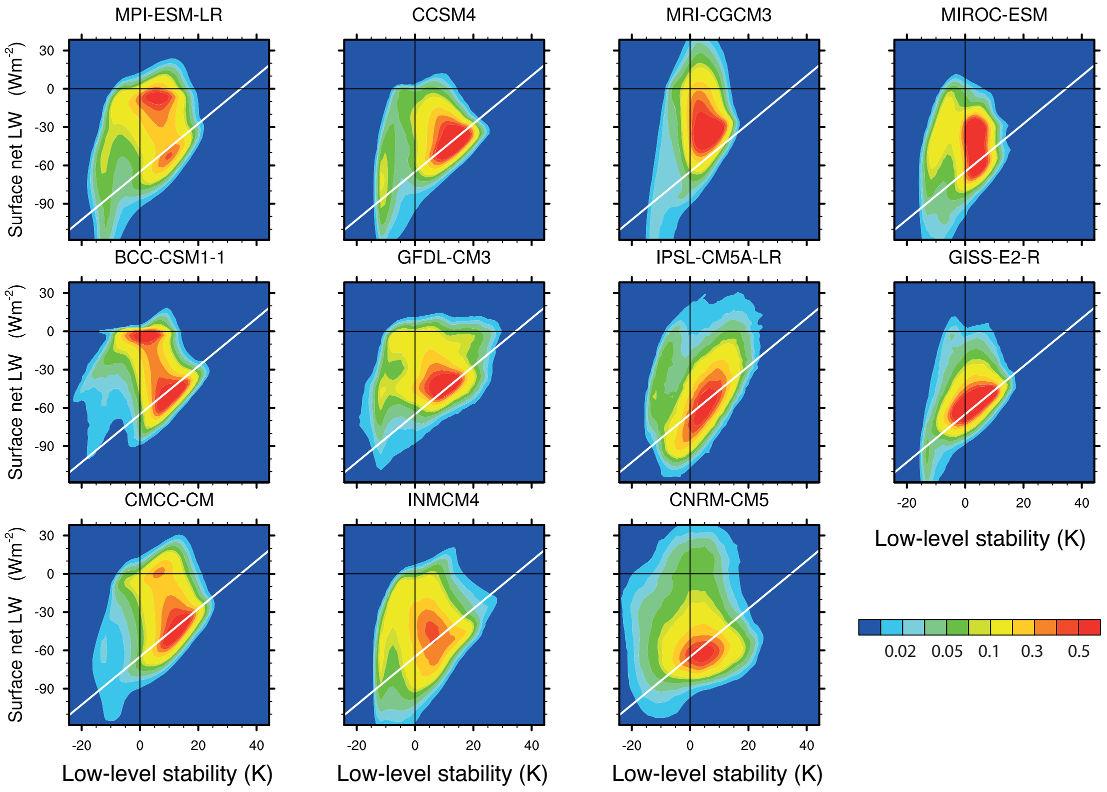

Figure 4.11: Bivariate pdfs of NDJF low-level stability and surface net longwave radiation from CMIP5 models, 6-hourly values from the ocean area north of 64°N for 1990-1999 of the historical runs.

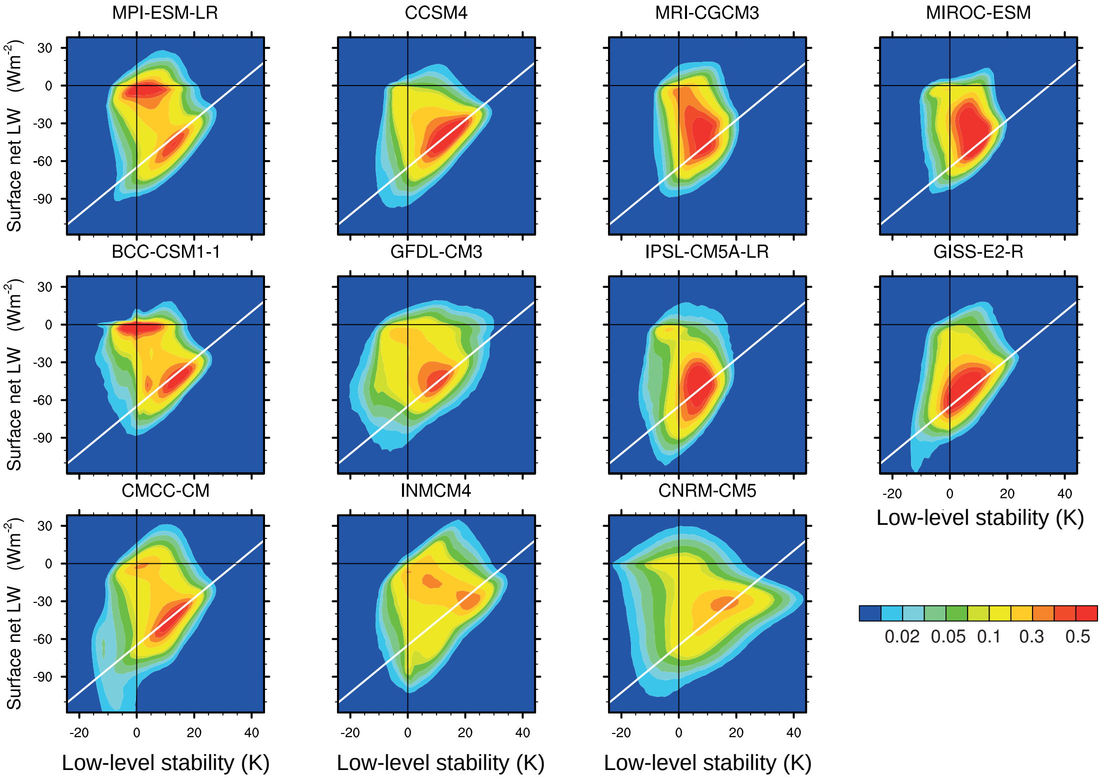

Figure 4.12: Bivariate pdfs of NDJF low-level stability and surface net longwave radiation from CMIP5 models, 6-hourly values over land.

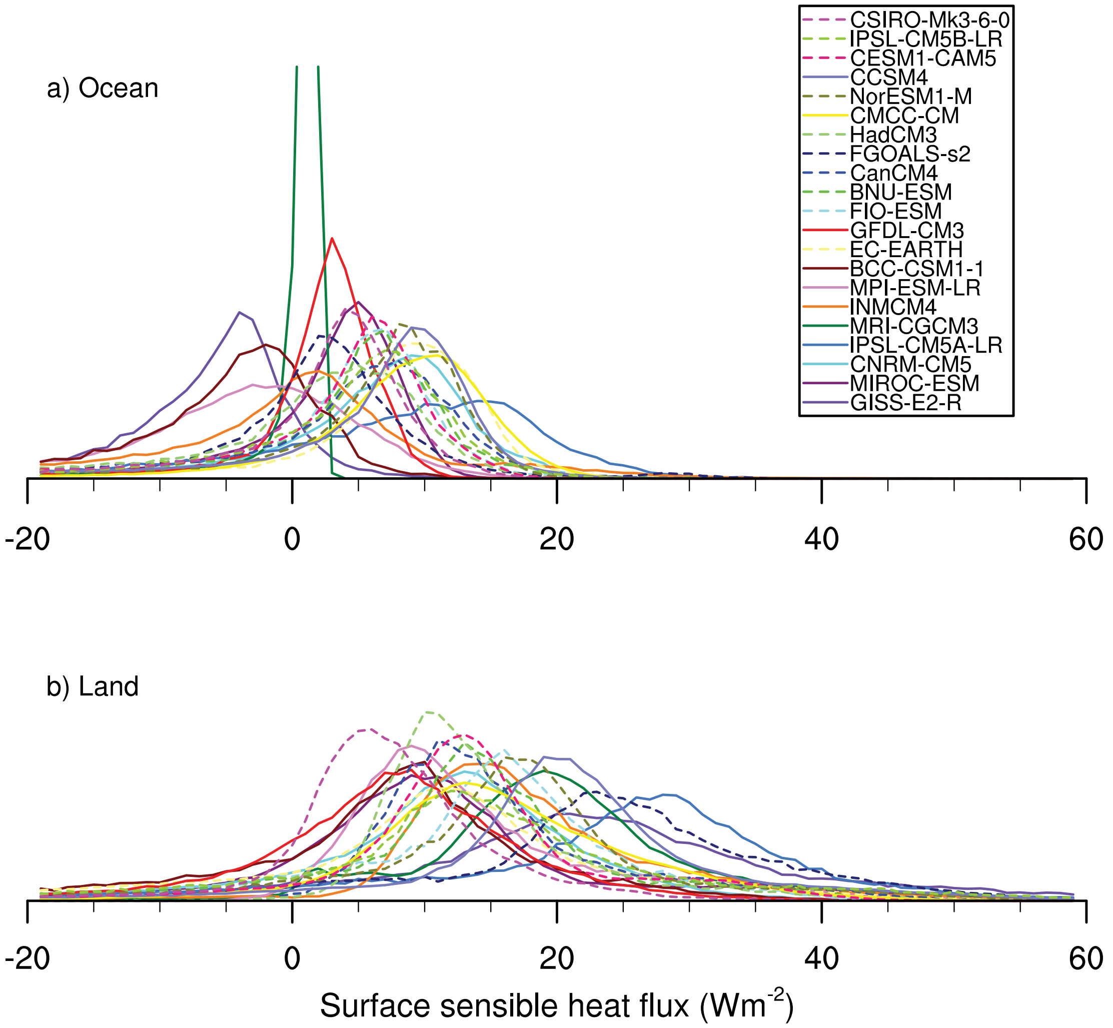

Figure 4.13: PDF of Arctic NDJF monthly mean turbulent heat fluxes in CMIP5 models 1990-1999, positive downwards. Downward turbulent fluxes in the MRI-CGCM3 model are always very small over sea ice, which results in the narrow peak at small positive values in Figure a.

The models can be grouped into three categories (Figures 4.11 and 4.12):

1. Three models (BCC-CSM-1-1, CMCC-CM and MPI-ESM-LR) reproduce the bimodal behaviour of the Arctic winter boundary layer with distinct clear and cloudy states as well as stronger stability in the clear than the cloudy state. CMCC-CM has a less frequent cloudy state and stronger mean stability than BCC-CSM-1-1 and MPI-ESM-LR, which both have a stability about 1 K stronger than the reanalyses over the ocean and weaker than the reanalyses over land (Figure 4.4).

2. Three models (CCSM4, GFDL-CM3 and INMCM4) lack the cloudy state, out of which CCSM4 over both ocean and land, GFDL-CM3 over ocean and INMCM4 over land produce stronger mean stability than the reanalyses. GFDL-CM3 is one of very few models with stronger stability over the ocean than over land, while INMCM4 mean low-level stability is in agreement with the reanalyses over ocean and much stronger than the reanalyses over land.

3. Five models lacking the cloudy state produce weak stability despite strong longwave cooling. These models also produce weaker monthly mean stability than the reanalyses. We will show later that this can be caused by excessive downward sensible heat fluxes from the atmosphere or excessive upward conductive heat fluxes from the liquid ocean to the surface.

Some models that do not represent the cloudy state over the ocean do so over land. This is most evident in INMCM4, but also in GFDL-CM3, CNRM-CM5 and IPSL-CM5A which all show a distinct but small representation of the cloudy state over land.

We can explain some of the relationships between boundary layer state, low-level stability and surface heat fluxes (Figure 4.13 and 4.14) in different CMIP5 models. MPI-ESM-LR and BCC-CSM1-1 typically produce small upward monthly mean sensible heat fluxes over sea ice, while most other models including CMCC-CM produce mean downward turbulent fluxes (Figure 4.13). SHEBA observations show that upward turbulent fluxes indeed occur in the cloudy state, when the surface does not cool radiatively but is still warmed through conductive heat fluxes from the warmer ocean surface underneath the ice (Persson et al. 2002). We can therefore understand that models lacking the cloudy state predominantly produce downward sensible heat fluxes in a stably stratified boundary layer that is associated with surface radiative cooling.

IPSL-CM5A has the strongest downward sensible heat fluxes over both land and ocean, which explains the models' very weak stability despite strong longwave cooling. Interestingly, the introduction of a new physics package in IPSL-CM5B has substantially changed the inversion characteristics, reducing downward turbulent heat fluxes

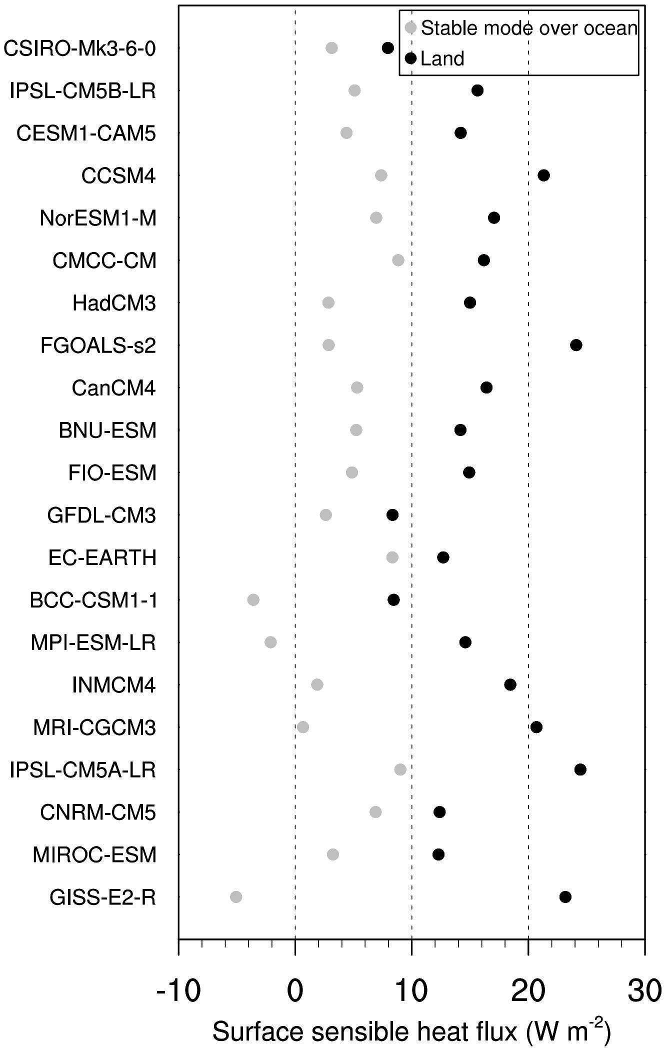

Figure 4.14: Arctic NDJF monthly mean turbulent heat fluxes in CMIP5 models 1990-1999, positive downwards.

and making the model produce a mean stability that is one of the strongest in the ensemble (Figure 4.4). Unfortunately, no sub-daily data from IPSL-CM5B were available for this study.

As noted before, most models have smaller land-ocean contrasts in low-level stability than reanalyses and much stronger downward sensible heat fluxes over land than over the ocean. In contrast to sea ice, the land surface is not warmed from below, which could explain stronger stability over land than sea ice. The much stronger sensible heat fluxes towards the land surface in models might be related to models overestimating diffusivity under strongly stable stratification (Cuxart et al. 2006), weakening the land-ocean contrast in low-level stability. Land-ocean contrasts in low-level stability are larger than in reanalyses in CNRM-CM5 (Figure 4.4), likely due to sensible heat fluxes being virtually identical over both surfaces.

The GISS-E2-R model stands out by having monthly mean turbulent fluxes similar to models that do represent the cloudy state (Figure 4.13), but by far the weakest stability over sea ice (Figure 4.4) while producing strong surface longwave cooling at all times (Figure 4.11). Over land, the GISS-E2-R model displays strong downward turbulent fluxes and stability at the lower end, but within the range of other models. We infer that the upward turbulent fluxes and very weak stability over the ocean are caused by strong conductive heat fluxes from the ocean that effectively prevent the boundary layer from becoming very stably stratified.

Eight of eleven analysed models lack a distinct representation of the cloudy state of the Arctic winter boundary layer over sea ice and therefore produce excessive surface longwave cooling. The few models that do represent a distinct cloudy state also have a monthly mean low-level stability in better agreement with reanalyses. Models with excessive longwave cooling caused by the lack of a cloudy state may either produce strong stability or compensate for the cooling by stronger turbulent or conductive heat fluxes towards the surface, which results in weak low-level stability. It should be noted that models lacking the cloudy state do not display a cloud-free Arctic ocean, but merely lack near-surface liquid or mixed-phase clouds that have a large enough emissivity to inhibit surface longwave cooling. In other words, the issue with models is not their cloud fraction but their cloud phase. We thus find that the bias of too little liquid water in Arctic winter clouds found by Cesana et al. (2012) for IPSL-CM5B does occur in a wide range of models.

4.5.1 The role of mixed-phase cloud microphysics

To link this process-based understanding of the climate models' mean state to individual model parametrisations, we perform sensitivity experiments using the SCM. Since the presence of cloud liquid water is important for determining the surface longwave radiation balance and thus the state of the Arctic boundary layer, the representation

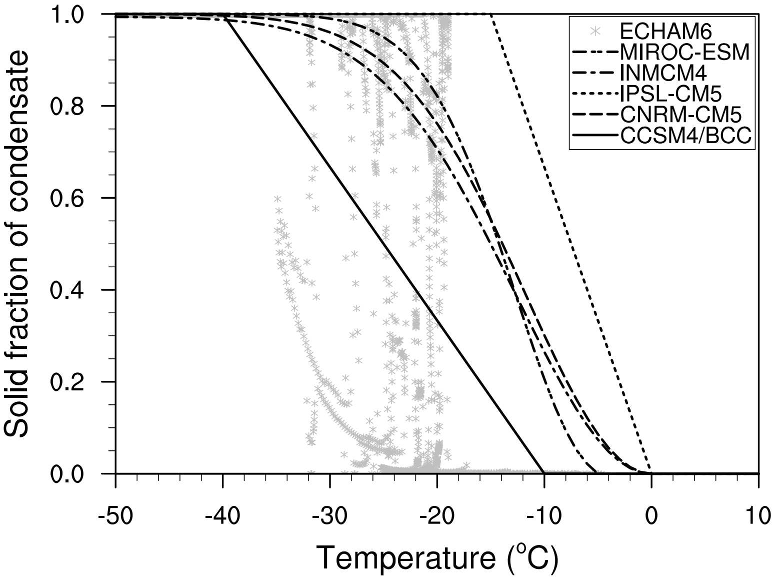

Figure 4.15: Temperature dependence of condensate phase in different CMIP5 models.

of mixed-phase cloud microphysics at low temperatures is likely to be an important process. Many CMIP5 models prescribe a temperature-dependent ratio of ice to total condensate (Figure 4.15). The atmosphere component of MPI-ESM-LR, ECHAM6, instead computes temperature-dependent freezing rates. For this model, ratios of ice to total condensate during the SCM experiment are plotted for comparison.

To test model sensitivity to changes in cloud microphysics, we modify the respective parametrisation in MPI-ESM-LR to mimic the behaviour of the other schemes shown in Figure 4.15 and re-run the single-column experiment. For all schemes except the one used in CCSM4 and BCC-CSM-1-1, which allows for a substantial fraction of cloud liquid water at cold temperatures, this leads to the disappearance of the cloudy state (Figure 4.16), showing that freezing of cloud liquid water at too warm temperatures can explain the lack of a cloudy state in the analysed models except for CCSM4. The phase of condensate is computed in the same way in CCSM4 and BCC-CSM-1-1, but the latter model does represent the cloudy state in agreement with our SCM experiment. The lack of the cloudy state in CCSM4 could be caused by other parametrisations, implementation issues or different large-scale conditions. In runs done with the single-column version of CCSM4, vertically integrated total cloudiness never exceeds 0.4, while it is unity during almost the entire experiment in ECHAM6 (not shown). This difference in the modelled cloud cover contributes to continuous surface radiative cooling on the order of 40 $\mathrm{W m^{-2}}$ in CCSM4, supporting the suggestion that mechanisms other than the mixed-phase cloud microphysics parametrisation are responsible for the lack of a

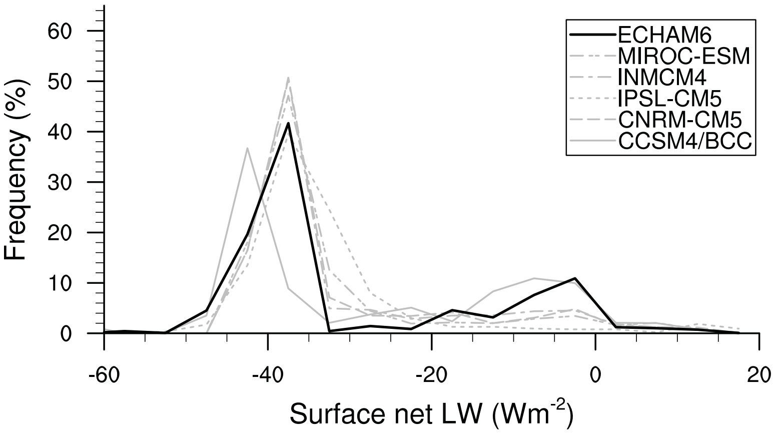

Figure 4.16: PDFs of surface net longwave radiation in SCM experiment with perturbed microphysics.

cloudy state in this model. We could not test the more complicated parametrisations of the GFDL-CM3, GISS-E2-R and MRI-CGCM3 models in the same way, but it is known that the freezing parametrisation in the GFDL-CM3 model leads to an almost complete disappearance of cloud liquid water below -15 °C (Rotstayn et al. 2000). The MRI-CGCM3 model has a parametrisation of the Bergeron-Findeisen process that leads to immediate freezing of all condensate as soon as cloud ice exceeds a threshold value of 0.5 mg kg^{-1} (Yukimoto et al. 2012), which is exceeded immediately once freezing begins in ECHAM6. It is therefore likely that these parametrisations also result in a rapid transition to ice clouds. In the GISS-E2-R model, there is a temperature-dependent probability for freezing to occur at any timestep plus a representation of the Bergeron-Findeisen process, which likewise make rapid glaciation very likely to occur (Schmidt et al. 2006).

Modifying one parametrisation of a single model to resemble the behaviour of other models is of course no substitute for a full model intercomparison, as we also see in the differing results between CCSM4 itself and the version of ECHAM6 modified to resemble CCSM4 mixed-phase cloud microphysics. However, our experiments show that the differences in cloud microphysics among CMIP5 models can determine the presence or lack of a cloudy state during Arctic air formation, all other things being equal.

4.5.2 Model sensitivity to turbulent diffusivity and heat conduction

Amongst models lacking a realistic representation of mixed-phase clouds, typical monthly-mean low-level stability still varies between 1.5 and 10 K (Figure 4.4). Under radiatively

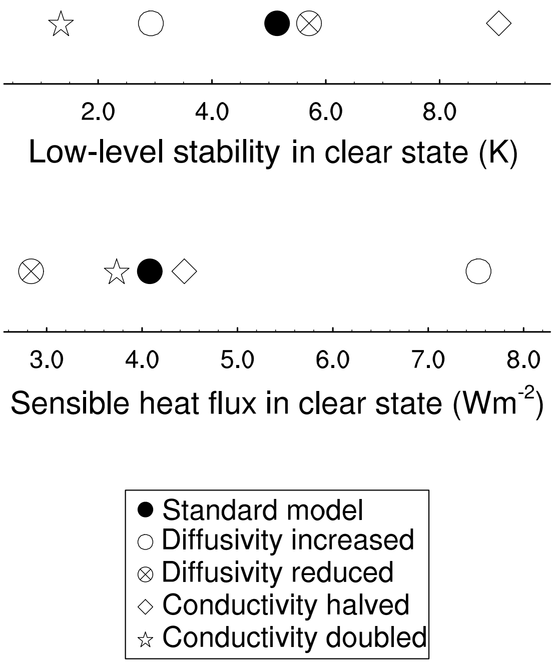

Figure 4.17: Overview of parametrisation sensitivity experiments in SCM. The clear state is defined as all timesteps with surface net longwave radiation below -20 $\mathrm{W m^{-2}}$

clear sky conditions, surface temperatures (and thus potentially stability and inversion strength) depend on turbulent and conductive heat fluxes to the surface (Sterk et al. 2013). To examine the extent to which different turbulent or conductive heat fluxes may cause differences in low-level stability, we perturb stable boundary layer diffusivity and snow conductivity in the ECHAM6 SCM and rerun our idealised experiment (Figure 4.17).

When diffusivity under stably stratified conditions is increased, the cloud deepens faster during the first days and the transition to clear skies happens earlier (not shown). We attribute this change to stronger mixing between the cloud and free-tropospheric air, which is a source of moisture to the Arctic boundary layer (Solomon et al. 2014), leading to faster condensation and hence drying of the atmospheric column. Under clear skies, the turbulent heat flux towards the surface is reduced by about 25 percent in a run with reduced diffusivity, resulting in slightly stronger stability. Downward turbulent heat fluxes almost double in the increased diffusivity run, leading to a reduction of low-level stability by several Kelvin.

The ocean beneath the sea ice is typically 10 to 40 K warmer than the Arctic wintertime atmosphere and thus constitutes a potentially important source of heat. Heat conduction to the atmosphere must be balanced by latent heat release from sea ice formation. How much heat is conducted to the surface depends on the thickness, density and specific conductivities of ice and snow. We here vary the conductivity of snow (shown as stars and triangles in Figure 4.17) as a proxy for inter-model differences in any of those quantities or in model formulations influencing conductive heat fluxes. Low-level stability in the clear state is almost doubled when snow conductivity is halved and is reduced to less than half the standard value when conductivity is doubled. Despite these impacts on low-level stability, turbulent heat fluxes towards the surface remain almost unchanged.

Sterk et al. (2013) studied the impact of both turbulent diffusivity and ice conductivity on surface fluxes and near-surface temperatures in a clear-sky stable boundary layer SCM experiment. They found a stronger sensitivity of fluxes and surface temperatures to turbulent diffusivity under strong winds ($8\,\mathrm{ms}^{-1}$), while conductive heat flux and clear-sky radiative transfer calculations were more important at low wind speeds ($2\,\mathrm{ms}^{-1}$). This confirms that both conductive and turbulent heat fluxes may affect low-level stability and temperature inversions under radiatively clear skies, but also shows that different stable boundary-layer regimes should be considered when analysing what role each process actually plays in a specific model.

In summary, the overestimation of stable boundary-layer diffusivity in most large-scale models may contribute to the lack of mixed-phase clouds in CMIP5 models. Weak low-level stability under radiatively clear skies as seen in the third group of CMIP5 models can be caused by excessive turbulent mixing or by excessive heat conduction through snow and ice.

4.6 Conclusions

We have shown that an idealised single-column experiment of the formation of an Arctic air mass driven by radiative cooling and cloud processes can reproduce the observed occurrence of a cloudy and a clear state of the Arctic winter boundary layer. The cloudy state characterised by little to no surface longwave cooling occurs when the formation of a liquid or mixed-phase cloud is triggered by radiative cooling of a relatively warm and moist air mass advected into the Arctic from lower latitudes. As the cloud cools, it transforms into a lower emissivity ice cloud that permits stronger surface cooling and is therefore associated with the radiatively clear state of the boundary layer. When the ice cloud has precipitated out, the boundary layer remains in the clear state until a new moist air mass is advected in. During the formation of Arctic air, inversions are formed by advection, eroded by cooling at the cloud level and formed again by surface cooling in the clear state. This results in two typical quasi-stable states, with inversions being stronger in the clear than in the cloudy state.

Changing individual parametrisations in the SCM and comparing results to the standard model, we find that the representation of mixed-phase cloud microphysics is key to successfully modelling the two boundary layer states. Freezing of supercooled water at too warm temperatures that occurs in many CMIP5 models leads to a lack of high-emissivity mixed-phase clouds and thus of a cloudy state in these models. Models lacking a cloudy state display excessive surface radiative cooling in Arctic winter, which tends to produce strong low-level stability and temperature inversions. However, weak temperature inversions in the absence of high-emissivity clouds may be sustained through excessive downward turbulent heat fluxes from the atmosphere or excessive conductive heat fluxes from the ocean, both of which warm the surface.

These processes control the representation of the two boundary layer states and inversion strengths in the CMIP5 models:

1. Few models that allow for cloud liquid water at very low temperatures reproduce both the clear and cloudy state of the boundary layer. Among these models, mean low-level stability depends mostly on the relative occurrence of the two states.
2. A second group of models lacks the cloudy state and exhibits strong stability and strong longwave cooling.
3. Other models also lack the cloudy state, but generate weak stability despite strong longwave cooling. This may be caused by excessive sensible and/or conductive heat fluxes to the surface.

The CMIP5 intermodel spread of typical monthly-mean low-level stability over sea ice in winter is about 10 K, which is similar to that in CMIP3 models (Medeiros et al. 2011). 15 out of 21 CMIP5 models overestimate low-level stability over sea ice compared to reanalyses data, and we argue that this overestimation is substantially larger than biases in the reanalyses. We have shown that this widespread model bias is linked to shortcomings in the representation of mixed-phase cloud microphysics. Models that do exhibit a reasonably frequent cloudy state also exhibit mean low-level stability in good agreement with reanalyses. To understand the causes of biases in turbulent fluxes and/or heat conduction which likely cause weak low-level stability despite strong surface radiative cooling, a closer analysis of the affected third group of models would be necessary. Likewise, the differences in cloud properties, energy fluxes and inversion strengths between land and sea ice domains remain to be investigated.

To advance our understanding of the formation of Arctic air masses and to further link model performance to specific parametrisations, we suggest comparing the results of a wider range of single-column models for an idealised case of warm air advection into the Arctic. In order to better represent the Arctic winter boundary layer and surface energy budget in climate models, an important step would be to improve the mixed-phase cloud microphysics and to obtain an adequate representation of the cloudy state.

Chapter 5

Challenges in improving the representation of boundary-layer turbulence in a general circulation model

Abstract

Turbulent fluxes of momentum in the boundary layer exert drag on the large-scale circulation, and the turbulent fluxes of heat and moisture are important terms in the surface energy budget. Model intercomparisons have identified important deficits in the representation of the stable boundary layer by turbulence parametrisations used in current weather and climate models. However, detrimental impacts of more realistic schemes on the large-scale flow have hindered progress in this area. Here, we implement a total turbulent energy scheme into the climate model ECHAM6. Reducing the previously exaggerated surface drag in stable boundary layers indeed causes an increase in zonal mean winds and large-scale pressure gradients, which can be compensated for by increasing the parametrised orographic drag and mountain lift. The new scheme includes a more physically-based length scale and implicitly represents entrainment flux in a dry convective boundary layer. Modifying the neutral turbulent Prandtl number changes the atmospheric temperature and humidity structure, affecting clouds and precipitation.

5.1 Introduction

Turbulent motion on scales from a few metres to the depth of the planetary boundary layer cannot be resolved in general circulation models (GCMs) with a horizontal grid spacing ranging from a few to about a hundred kilometres. While first high-resolution global atmospheric models are able to resolve deep convection (Satoh et al. 2008), boundary-layer turbulence will remain unresolved in such models for the foreseeable future. Horizontal turbulent fluxes of momentum, heat, moisture or other tracers are usually negligible at the resolution of current GCMs, but vertical turbulent fluxes are crucial and thus need to be parametrised. The relevant scales of important atmospheric processes and the increasing resolution of models used for climate research and weather prediction are visualised in Figure 5.1.

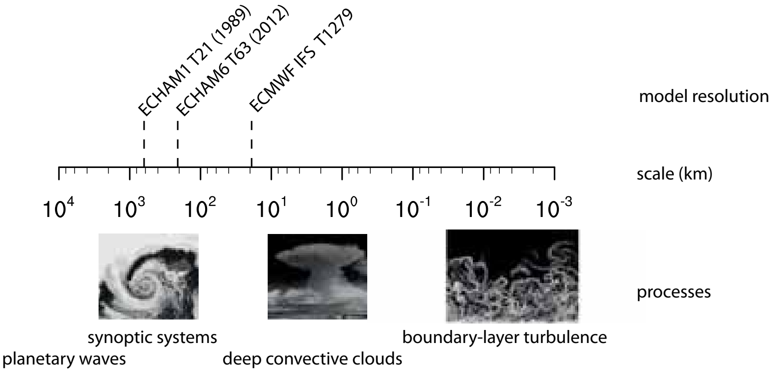

Figure 5.1: Scales of atmospheric processes and resolution of global atmospheric models. The positioning of model names along the axis represents the horizontal resolution of each model at the equator, and that of atmospheric processes indicates the scales relevant for each process. Cyclone picture by NASA, Cumulus cloud by NOAA, turbulence graphic courtesy of Cedrick Ansorge

The task of a turbulence parametrisation is to predict the mean turbulent fluxes in the vertical for given profiles of wind and buoyancy, the latter being a function of temperature and moisture. Any set of equations that can be derived from first principles of physics to describe turbulent fluxes contains more unknowns than equations and thus cannot be solved. Empirical relationships or turbulence closures are therefore needed to parametrise turbulent fluxes for weather and climate models. Such parametrisations have been developed and increased in complexity from the very first atmospheric GCMs (Smagorinsky et al. 1965) to the latest generation of coupled climate models, but most are still based on the same fundamentals of boundary-layer meteorology and turbulence theory developed by Monin and Obukhov (1954).

In the simplest form, the surface stress or momentum flux at the surface is given as

$$(u_*)^2 = \frac{k^2}{\ln^2\left(\frac{z}{z_0}\right)} f_m U^2, \tag{5.1}$$

where k is the von karman constant, z the height of the first model level, z_0 the aerodynamic roughness length and U the mean wind at the first level height. The aerodynamic roughness length z_0 is defined as the height at which the logarithmic near-surface wind profile vanishes when being extrapolated towards the surface. To account for the effect of stable or unstable stratification, an empirically derived stability function

$f_m(Ri)$ is introduced, where the Richardson number Ri as the ratio of stratification to wind shear is a measure of stability. The surface fluxes of heat and water vapour can be derived in an analogous fashion:

$$H = \frac{k^2}{\ln\left(\frac{z}{z_0}\right) \cdot \ln\left(\frac{z}{z_{0h}}\right)} \frac{1}{Pr_0} f_h |U| (\theta_z - \theta_S), \tag{5.2}$$

where θ_z and θ_S are the potential temperatures at the first level and the surface, respectively, and z_{0h} is the roughness length for heat.

While different stability functions f_m and f_h are usually used for momentum and heat, the ratio of the drag coefficients for heat and momentum at neutral stratification, the turbulent Prandtl number Pr_0 is often implicitly understood to be equal to unity (Liu et al. 2013). For the surface layer, this is equivalent to ascribing any difference between the neutral drag coefficients for heat and momentum to differences between the roughness lengths for momentum and heat, z_0 and z_{0h}. A range of values between 0.7 and 1 has been suggested for Pr_0 (Kays 1994), but the consequences of assuming a specific neutral turbulent Prandtl number are rarely discussed in the context of weather and climate modelling. What ratio the flux coefficients for heat and momentum have in the neutral limit may appear to be a purely academic question, since the heat flux at neutral stratification is zero by definition. However, the stability functions for both heat and momentum only scale the respective neutral values of the coefficients, such that the neutral turbulent Prandtl number impacts the ratio of heat to momentum diffusivity for any stability: $Pr(Ri) = Pr_0 \cdot \frac{f_m(Ri)}{f_h(Ri)}$.

Away from the surface, parametrised turbulent fluxes can be obtained from a turbulent diffusivity coefficient (K) multiplied by the gradient of the resolved fields:

$$F_X = -K \frac{\partial X}{\partial z}. \tag{5.3}$$

The diffusivity can be computed from a mixing length l characterising the size of the largest eddies, the stability functions and, for some schemes, turbulent kinetic energy (TKE). In the alternative K-profile approach, a profile of eddy diffusivity is prescribed based on the properties of the entire boundary layer. Some models further use a mass-flux approach to represent the transport by convective eddies that are larger than the vertical grid spacing, which is a counter-gradient flux in the upper part of a typical convective boundary layer. Over the past decades, much work has been done to determine the ideal form and parameter values of the stability functions, the roughness lengths for momentum and heat over various surfaces and to develop and improve schemes to compute the diffusivity and in some cases the convective mass flux in the atmospheric boundary layer (e.g. Louis 1979; King et al. 2001; Köhler et al. 2011; Bogenschutz et al. 2013).

The GABLS (Global Atmospheric Boundary Layer Studies) model intercomparisons have shown that operational models still struggle to represent stable boundary layers (SBL) and the diurnal cycle of near-surface variables, with many models overestimating diffusivity under stable stratification (Holtslag et al. 2013). This overestimation has in principle been known for a decade or longer, and was sometimes purposefully introduced to avoid a decoupling and runaway cooling of the surface under strongly stable stratification (Viterbo et al. 1999). It is also known that the performance of numerical weather prediction models benefits from using larger diffusivities in SBLs than can be justified from large-eddy simulations (LES) and observations, but the reasons for this model behaviour remain unclear. Sandu et al. (2013) recently showed that reducing SBL diffusivity leads to stronger high- and low-pressure systems in 10-day forecasts using the ECMWF model, causing or worsening a high bias in model activity at the planetary and synoptic scales, especially in the winter hemisphere. They also found that changes to the low-level blocking and orographic drag scheme can at least partly compensate for these deteriorations. These results have encouraged us to further investigate the role of boundary-layer diffusivity at the longer time scales relevant to climate modelling and to explore options for a physically more realistic representation of boundary-layer turbulence in ECHAM. To that end, we implement a total turbulent energy closure (Mauritsen et al. 2007; Angevine et al. 2010) into the climate model ECHAM6.

We set off by describing the turbulence and sub-grid drag schemes currently implemented in ECHAM6 and the experiments and datasets used throughout the study (Section 5.2). We then document our implementation of the TTE scheme in ECHAM6 (Section 5.3) and show how it performs in idealised single-column experiments. Finally, we investigate the impact of changing stable boundary-layer diffusivity and turbulent Prandtl number in global experiments. We conclude with an evaluation of the progress achieved with ECHAM-TTE and suggestions for possible further improvements.

5.2 Model, data and experiments

5.2.1 ECHAM6 climate model

We use the atmospheric component of the MPI climate model ECHAM6 (Stevens et al. 2013). Besides a number of bugfixes and a change of roughness length computation over land, no major changes of the model physics have occurred between the documented version 6.1 used in the 5th phase of the Coupled Model Intercomparison Project (CMIP5) and version 6.2, which is the basis for our implementation. However, it should be noted that the model needed to be retuned after the implementation of several bugfixes to make sure it would still yield a balanced pre-industrial control climate and reproduce the historical record. We here give a brief description of the

1.5-order turbulence scheme currently used in ECHAM (Brinkop and Roeckner 1995). Turbulent diffusivity K_m and conductivity K_h are computed as

$$K_{m,h} = l \cdot F_{m,h} \cdot \sqrt{E_k}, \tag{5.4}$$

where l is the mixing length, $F_{m,h}$ are the stability functions for heat and momentum and E_k is turbulent kinetic energy. The mixing length l is obtained from

$$\frac{1}{l} = \frac{1}{kz} + \frac{1}{\lambda}, \tag{5.5}$$

where λ equals 150 m in the boundary layer and decreases exponentially to 1 m in the free troposphere. Note that the neutral stability coefficients are different from unity and different for heat and momentum, leading to a neutral Prandtl number of about 0.8.

In the surface layer, drag coefficients are computed from the roughness lengths and stability functions based on Louis (1979) following equations 5.1 and 5.2. The original scheme by Louis (1979) explicitly included a neutral turbulent Prandtl number of 0.74, but did not allow for different roughness lengths for heat and momentum. For the surface layer computations in ECHAM6, however, the neutral turbulent Prandtl number is assumed to be equal to unity. On the other hand, ECHAM6 does allow for different roughness lengths over ocean and to a limited extent over land (but not over sea ice). The roughness length for momentum over ocean is computed using the Charnock relation, whereas the roughness length for heat is derived from that for momentum as $z_{0h} = z_{0m} \exp(2 - 86.276 \cdot (z_{0m})^{0.375})$. For unstable conditions over ocean, the stability coefficient for heat f_h is computed using a free-convection approximation (Miller et al. 1992) to account for the mixing by convective eddies at low mean wind velocities. The effective ratio $\frac{C_D}{C_H}$ over ocean is therefore no unique function of static stability.

ECHAM uses a staggered vertical coordinate, where temperature, moisture and wind velocities are computed at full levels, whereas turbulent energy and the fluxes of heat, moisture and momentum are defined at half levels. The lowest half level is located at the surface, and in the standard vertical resolution L47, the lowest full level is located about 30 m above the ground. The next level is placed around 120 m and a total of ten levels represent the lowermost 3 km of the atmosphere. Past increases in the number of levels have primarily served to improve the representation of the stratosphere, such that the vertical resolution in the boundary layer is identical for the versions L31, L47 and L95. Standard model runs are made using the tagged version 6.2.00 and ECHAM-TTE corresponds to revision 3435 of echam_6.2.00_tte_fxp.

Mountain lift parametrisation

The sub-grid orographic drag scheme by Lott (1999) is implemented in ECHAM6 to represent the drag and mountain lift generated by non-resolved orography. The scheme

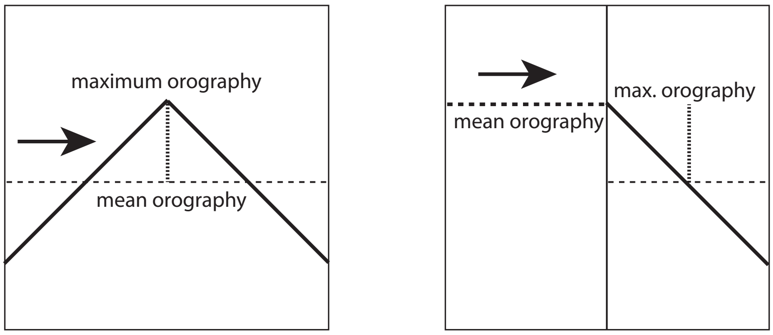

a) unresolved peak b) resolved plateau

Figure 5.2: Sketch of the representation of non-resolved and resolved orographic features in the subgrid-scale orographic drag scheme. a) shows the situation for which the scheme has been developed, whereas b) is representative of the edges of large ice sheets, where the application of mountain lift forces to the difference between mean and maximum orography causes a spurious effect on the circulation

computes a drag force opposed to the mean wind, which is thought to represent drag by orographically blocked flow, and a lift force perpendicular to the mean wind. However, the key tuning parameter for the lift parametrisation is currently set to zero, such that only drag forces by the non-resolved orography are simulated. While alleviating some biases in the mean pressure fields, the mountain lift parametrisation in its current implementation introduces new biases around Antarctica and in Northern Europe. We attribute these to a conceptual problem in the representation of the big ice sheets of Antarctica and Greenland, which have central plateaus resolved by the model grid (Figure 5.2). On the downwind side of the Greenland ice sheet and at the edges of the Antarctic plateau, the difference between the mean and the maximum orography therefore does not represent an unresolved peak. Reducing the maximum orography to the mean orography over the eastern half of the Greenland ice sheet and over Antarctica clearly improves the pressure fields over Northern Europe when the lift parametrisation is used. This modified orography is used to demonstrate the value of parametrised mountain lift for the model, but more work is needed to solve this problem in a more consistent manner, for example by taking the orientation of slopes and the height of adjacent grid points into account.

5.2.2 Data

ERA-Interim reanalysis data (Simmons et al. 2007) is used to evaluate the performance of the different versions of ECHAM. The reanalysis is obtained by assimilating a large

Table 5.1: Setup of the single-column experiments

Experiment	SBL (GABLS1)	dry CBL
z0m, z0h	0.1 m	0.1 m
Initial surface temperature	265 K	290 K
Surface temperature change	-0.25 $\mathrm{Kh^{-1}}$	0.5 $\mathrm{Kh^{-1}}$
Initial temperature profile	$\theta = \begin{cases} 265\,\mathrm{K} & \text{for } z \leq 100\,\mathrm{m} \\ 265\,\mathrm{K} + 0.01\,\mathrm{Km^{-1}} \cdot z & \text{for } z > 100\,\mathrm{m} \end{cases}$	$\mathrm{T}=290\,\mathrm{K}+0.0065\,\mathrm{Km^{-1}} \cdot z$
geostrophic wind (u)	8 $\mathrm{ms^{-1}}$	0 or 10 $\mathrm{ms^{-1}}$
Radiation	off	off
Latent heat flux, moisture	0	0
Latitude	73°N	50°N

array of observations into the ECMWF model. Especially in regions with few or no regular observations, the reanalysis is strongly model dependent and should thus be interpreted with caution. Results from direct numerical simulations of a free convective boundary layer from Garcia and Mellado (2014) are used as a basis for comparison for the single-column experiments.

5.2.3 Experiments

We run the model with prescribed sea-surface temperatures and sea-ice concentrations as observed from 1979 to 2008 (AMIP setup). For the stable boundary layer single-column experiments, we use the GABLS1 setup (Cuxart et al. 2006), where prescribed surface cooling (0.25 $\mathrm{Kh^{-1}}$) and a constant geostrophic wind (8 $\mathrm{ms^{-1}}$) drive the development of a moderately stable boundary-layer. For the unstable case, we use a similar setup with prescribed surface warming (0.5 $\mathrm{Kh^{-1}}$), a linear initial temperature profile and geostrophic winds of 0 and 10 $\mathrm{ms^{-1}}$ (Table 5.1).

5.3 Total turbulent energy scheme

The budget equation for turbulent kinetic energy (TKE) reads

$$\frac{DE_{kin}}{Dt} = \tau \cdot S + \frac{g}{\theta}\overline{w'\theta'} - \gamma - \frac{\partial F_E}{\partial z}, \tag{5.6}$$

where the first term on the right-hand side is referred to as shear production of turbulence, the second term as buoyancy production under unstable or buoyancy destruction under stable stratification, and the remaining terms represent dissipation and the turbulent flux of turbulent energy. In a TKE framework, the displacement of an air parcel against the buoyancy gradient of a stably stratified boundary layer is thus interpreted as buoyancy destruction of TKE. When buoyancy destruction exceeds shear production, turbulence cannot be sustained and the flow becomes laminar. The stability threshold at which buoyancy destruction equals shear production is called the critical Richardson number Ri_{crit} and is an implicit feature of the TKE scheme (Richardson 1920). Since observational studies have shown turbulence to be present at very high stabilities (e.g. Kondo et al. 1978; Smedman 1988), and because a breakdown of turbulence can cause both unphysical runaway cooling of the surface and numerical stability problems in models, excessive diffusivity has often been introduced in SBL schemes to avoid such a turbulence shutdown at high stabilities. A turbulence closure without an implicit critical Richardson number would thus be advantageous for the representation of stably stratified boundary layers in GCMs.

Such a closure can be obtained by using total turbulent energy (TTE) rather than turbulent kinetic energy as prognostic variable. TTE is defined as the sum of turbulent kinetic energy and turbulent potential energy (Zilitinkevich et al. 2007)

$$E_p = \frac{1}{2}\sigma_\theta^2 \frac{\beta^2}{|N^2|}. \tag{5.7}$$

When an air parcel is displaced against the buoyancy gradient of a stable boundary layer, turbulent kinetic energy is converted to turbulent potential energy, and TTE is conserved. Total turbulent energy is only lost through dissipation, and can therefore be in a steady state at arbitrarily high stabilities.

We here implement the TTE closure developed by Mauritsen et al. (2007) based on observations of stably stratified turbulence (Mauritsen and Svensson 2007) and tuned to match a set of large-eddy simulations. Angevine et al. (2010) extended the TTE closure for use in unstable conditions when developing an eddy-diffusivity mass-flux scheme for the Weather Research and Forecast model (WRF). We use their developments for the eddy diffusivity component under unstable stratification.

5.3.1 Turbulent potential and turbulent kinetic energy

The budget equation for total turbulent energy can be obtained as the sum of the budget equations for turbulent kinetic and turbulent potential energy. It reads

$$\frac{DE}{Dt} = \tau \cdot S - \gamma - \frac{\partial F_E}{\partial z} + \begin{cases} 0 & \text{for } N^2 \geq 0 \\ 2\beta\overline{w'\theta'} & \text{for } N^2 < 0 \end{cases}, \tag{5.8}$$

where τ is the turbulent stress, S the wind shear, $\gamma = 0.07E^{1.5}l^{-1}$ the dissipation rate, $\beta = g\theta^{-1}$ the buoyancy parameter, $N^2 = \beta\frac{\partial\theta}{\partial z}$ the square of the Brunt-Vaisala frequency, $F_E = -|S|l^2\frac{\partial E}{\partial z}$ is the turbulent flux of turbulent energy and l the turbulence length scale. The ratio of turbulent potential to turbulent kinetic energy is diagnosed as

$$\frac{E_p}{E_k} = \begin{cases} \dfrac{Ri}{2 \cdot Ri - Pr_0} & \text{for } Ri < 0 \\ \dfrac{Ri}{3 \cdot Ri + Pr_0} & \text{for } Ri \geq 0 \end{cases} \tag{5.9}$$

5.3.2 Length scales

As the turbulence scheme previously implemented in ECHAM, the TTE scheme uses a turbulent length scale that is thought to represent the size of the largest eddies, which determine the spatial scale of mixing processes and the dissipation of turbulent energy. Under stable stratification, eddies are limited in size by the distance to the surface, deformation by the Coriolis force and static stability. Implementing these constraints in ECHAM-TTE is a conceptual advance over the previous scheme, which only considered the distance to the surface and a fixed asymptotic length scale far away from the surface (Blackadar 1962). For convective boundary layers, we use an up-down length scale based on the distance to the surface and the dry thermal top. This length scale l is computed as

$$\frac{1}{l} = \frac{1}{kz} + \begin{cases} \dfrac{f}{C_f\sqrt{\tau}} + \dfrac{N}{C_N\sqrt{\tau}} & \text{for } N^2 \geq 0 \\ \dfrac{3}{k(h_d - z)} & \text{for } N^2 < 0 \end{cases}, \tag{5.10}$$

where f is the Coriolis parameter, $C_f = 0.185$ and $C_N = 2$ are tuning parameters of the scheme, and h_d is the dry thermal top in a convective boundary layer, defined as the first model level with a dry static energy exceeding that of the lowest model level. Outside the boundary layer, the same equations are applied, but the mixing length is not allowed to exceed 150 m.

5.3.3 Diffusivities under stable and unstable stratification

Above the surface, the turbulent diffusivity (K_m) and conductivity (K_h) under stable stratification are computed as

$$K_m = \frac{f_\tau^2 E_k^2}{C_\epsilon \dfrac{E_k\sqrt{E}}{l} - \beta f_\theta \sqrt{E_k \sigma_\theta^2}} \tag{5.11}$$

and

$$K_h = \frac{2 f_\theta^2 E_k l}{C_\Phi \sqrt{E}}. \tag{5.12}$$

The respective coefficients under unstable stratification are obtained as

$$K_m = \frac{f_\tau^2}{C_\epsilon} l \sqrt{E_k} f_m(Ri) \tag{5.13}$$

and

$$K_h = Pr_0^{-1} K_m f_h(Ri) \tag{5.14}$$

with $C_\epsilon = C_\Phi = 0.07$. For convective boundary layers, the unstable form of the diffusivity equations is used up to $z = 0.5h_d$ and above if the resulting diffusivities exceed those from the stable form of the equations. Under stable conditions, the scheme uses stability functions formulated in terms of the non-dimensional stress $f_\tau = \frac{|\tau|}{E_k}$ and heat flux $f_\theta = \frac{\overline{w\theta}}{\sqrt{E_k \sigma_\theta^2}}$, where $f_\tau = 0.17\left(0.25 + 0.75(1+4Ri)^{-1}\right)$ and $f_\theta = -0.145(1+4Ri)^{-1}$ (Mauritsen and Svensson 2007). Under unstable conditions, we retain the stability functions based on Louis (1979).

5.3.4 Surface layer

Surface fluxes are computed as

$$\tau = \frac{l^2}{(f_{sl} \cdot z_1)^2 \ln\left[\frac{z_1}{z_{0m}}\right]^2} \frac{f_\tau(Ri)}{f_\tau(0)} (U^2 + V^2) \tag{5.15}$$

and

$$\overline{w'\theta'} = \frac{l^2}{(f_{sl} \cdot z_1)^2 \ln\left[\frac{z_1}{z_{0t}}\right] \ln\left[\frac{z_1}{z_{0m}}\right]} \frac{f_\theta(Ri)}{f_\theta(0)} \sqrt{\frac{f_\tau(Ri)}{f_\tau(0)}} \cdot (U^2 + V^2 + c_w w_*^2)(\theta_1 - \theta_S), \tag{5.16}$$

where z_1 is the height of the first model level, usually around 30 m, $w_* = \left(g\theta_v^{-1} h_d \overline{w'\theta_v'}\right)^{1/3}$ is the convective velocity scale and f_{sl} is the fraction of the first-level height at which the surface fluxes are nominally evaluated. Note that Mauritsen et al. (2007) used $f_{sl} = 0.5$ and extrapolated fluxes from the next atmospheric flux level down to the surface. Implementing such an extrapolation in a GCM would be complicated due to the different surface properties that may be contained in one gridbox, and a first attempt of doing so lead to numerical instability. To avoid such complications and keep the scheme reasonably simple, we immediately use the computed fluxes as surface fluxes and reduce the nominal height used for the flux computation. We will show later how f_{sl} affects the surface drag in stable boundary layers. Following Beljaars (1994), we include the convective velocity scale into the total wind speed used to derive the surface heat flux in order to account for free convection. The ratio of the mean absolute wind at the first level to the convective velocity scale under free convection, c_w, was suggested to be 1.2 by Beljaars (1994), but shown to be around 0.5 in recent DNS experiments of a free-convective boundary layer (Garcia and Mellado 2014).

To provide a lower boundary condition for total turbulent energy, its value at the surface is taken to be

$$E = \left(1 + \frac{E_p}{E_k}\right) \cdot \frac{1}{f_\tau} \left(u_*^3 + l \cdot 2 \frac{g}{\theta_v} \overline{w'\theta'}\right)^{2/3} . \tag{5.17}$$

The prognostic equation for total turbulent energy is solved implicitly using the same numerical scheme that was used for the TKE equation by Brinkop and Roeckner (1995). All vertical fluxes including surface fluxes are computed using an integrated implicit solver (Schulz et al. 2001). Surface fluxes, 2 m temperatures and 10 m winds are interpolated following Geleyn (1988).

5.4 Results and discussion

The impact of changes in climate model physics on the modelled climate can be challenging to understand, since any substantial change in local processes affecting the fluxes of heat and momentum will change the large-scale circulation, which in turn controls temperature and moisture profiles and thus affects surface fluxes. In order to better understand the impact of the new turbulence scheme in a controlled setting, we first test the new model version ECHAM-TTE in idealised single-column model test cases for the stable and convective boundary layer as described in Table 5.1. As we proceed to global simulations, the understanding of local effects derived from the SCM experiments will help interpret changes in the global model.

5.4.1 Performance of the total turbulent energy scheme in idealised single-column experiments

ECHAM 6.2 produces too much surface drag in stable boundary layers, as do many operational models. For the GABLS1 case described in section 5.2.3, the friction velocity from ECHAM 6.2 clearly falls outside the range of LES results (Figure 5.3), and corresponds to that of the most diffusive models that participated in the intercomparison (Cuxart et al. 2006). The new TTE scheme produces more realistic results in the middle of the LES range (solid line). The surface drag can be varied by changing the fraction of the first-level height at which surface fluxes are nominally evaluated, which is represented by the parameter f_{sl}. Reducing f_{sl} from 0.5 to 0.4, surface drag is somewhat increased but remains within the range of LES results. The original code from Mauritsen et al. (2007) uses a much higher vertical resolution and interpolates fluxes from the lowest flux level to the surface. When run at a similar resolution as ECHAM, the original scheme produces somewhat lower surface drag with friction within the lower part of the LES range (not shown).

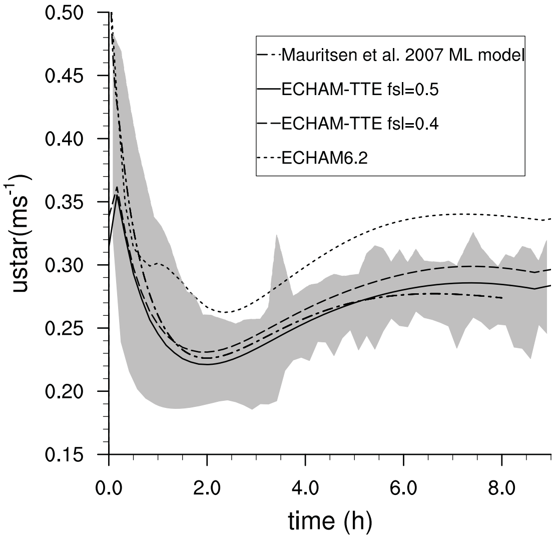

Figure 5.3: Friction velocity for the GABLS1 case. The grey shaded area denotes the range of LES results at 6.25 m resolution, the lines correspond to the original Matlab code by Mauritsen et al. (2007) and different versions of the ECHAM single-column model, all at the standard vertical resolution L47.

In a growing convective boundary layer, buoyant plumes from the convective layer penetrate into the capping inversion, mixing warmer air into the boundary layer and thus causing a downward heat flux at the inversion, the entrainment flux. Direct numerical simulations of the entrainment zone at the top of a growing boundary layer show a complex interplay between length scales and turbulence properties set by the convective plumes penetrating into the inversion and by the local stability (Garcia and Mellado 2014). At the lower end of the capping layer, the dominant length scale is the depth of the boundary layer, whereas further inside the capping layer, the length scale transitions to a scale proportional to the ratio of the convective velocity scale to the stratification, $\frac{w_*}{N}$. The standard version of ECHAM6 produces effectively zero entrainment flux at the top of a growing CBL (Figure 5.4), such that no effect of entrainment on the evolution of the potential temperature profile is visible (Figure 5.5). ECHAM-TTE produces substantial entrainment flux which visibly affects the structure of the growing convective boundary layer and its capping inversion. Higher rates of entrainment in the new turbulence scheme are mostly achieved by using the convective length scale and diffusivities up to the dry thermal top whenever they are greater than

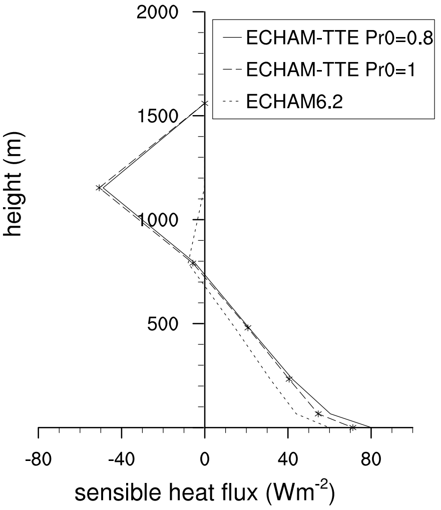

Figure 5.4: Sensible heat flux profiles for an idealised dry convective boundary-layer case (u_{geo}=10 ms^{-1}) averaged over one hour after 6 hours of model integration.

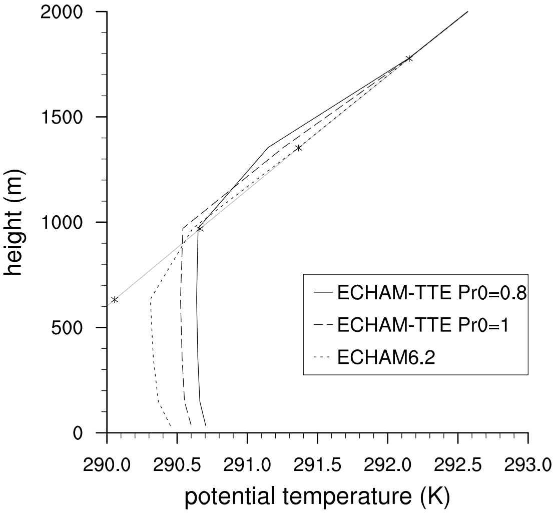

Figure 5.5: Potential temperature profiles, as Figure 5.4

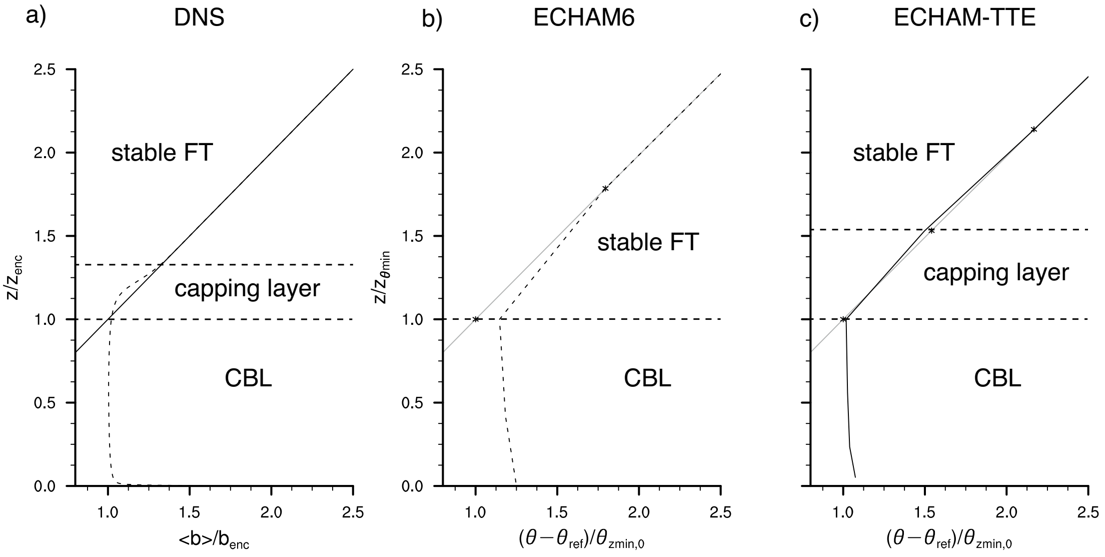

Figure 5.6: Normalised buoyancy/potential temperature profiles of a growing dry free convective boundary layer. The DNS experiment is described in Garcia and Mellado (2014). SCM experiments are normalised using the height of the minimum potential temperature as upper end of the mixed layer and a reference temperature of 290 K, which corresponds to the initial surface temperature of the background profile.

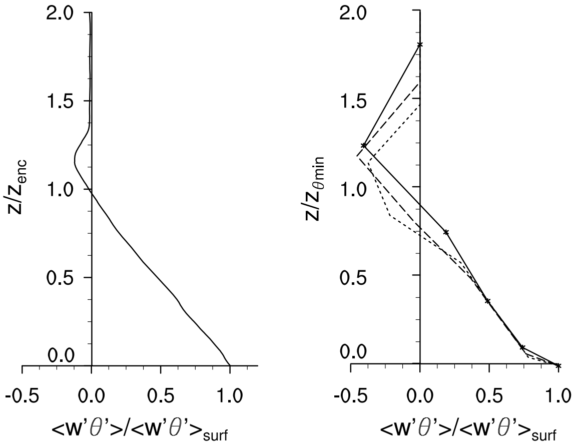

Figure 5.7: Normalised sensible heat flux profiles averaged over one hour at hours 6,8 and 10 of the dry free convective boundary layer experiment.

the length scale and diffusivity obtained from the equations for stable stratification. The old scheme is formulated purely in terms of the local stability and therefore ignores the influence of the underlying convective boundary layer at the first flux level within the capping inversion, treating this level as part of the stable free troposphere (Figure 5.6b). This leads to turbulence shutdown and absence of entrainment mixing. The new scheme effectively treats the entrainment zone or capping layer as a special part of the convective boundary layer (Figure 5.6c). Entrainment flux is implicitly computed in the turbulence scheme, i.e. without using an explicit entrainment parametrisation that other models rely on.

The implicit computation of entrainment demands to represent both the effects of the underlying convective layer and the static stability on turbulent diffusivity in the capping layer. In ECHAM-TTE, static stability influences diffusivity through the evolution of turbulent kinetic energy and the length scale limited by the small distance to the dry thermal top, whereas the effects of convection enter the computation of diffusivity through the equations for diffusivity and conductivity. Both the thickness of the capping layer and the length scale limited by the distance to the dry thermal top are affected by the vertical grid spacing, which becomes coarser with height. Entrainment flux in a free convective boundary layer over land, i.e. without wind shear, is larger in ECHAM-TTE than in direct numerical simulations (Figure 5.7). In contrast to the old scheme, ECHAM-TTE qualitatively represents the effect of entrainment flux on the structure of a growing dry convective boundary layer. The strength of the entrainment flux is however overestimated, and a more sophisticated treatment of the interaction of turbulence and stratification around the capping inversion that gives more weight to the effect of static stability is likely to further improve the scheme.

Reducing the neutral turbulent Prandtl number in the surface layer warms the boundary layer in the convective case (Figure 5.5) - the resulting larger turbulent conductivity for heat reduces the temperature gradient between the surface and the first model level. This turns out to have important consequences for climate in global model runs (section 5.4.3).

5.4.2 Surface drag and large-scale pressure gradients

Prior studies have shown that reduced, more realistic surface drag in stable boundary layers is often detrimental to the representation of the large-scale flow in global models (e.g. Viterbo et al. 1999; Sandu et al. 2013). Implementing the total turbulent energy scheme without substantially worsening the model's performance in regard of mean sea-level pressure and zonal mean zonal wind velocities would therefore already be a success. In comparison to the ERA-Interim reanalysis (upper panels of Figure 5.8), the reference model version ECHAM 6.2 has an Azores high that is too strong and a low-pressure bias extending eastwards from Iceland, which results in an exaggerated meridional

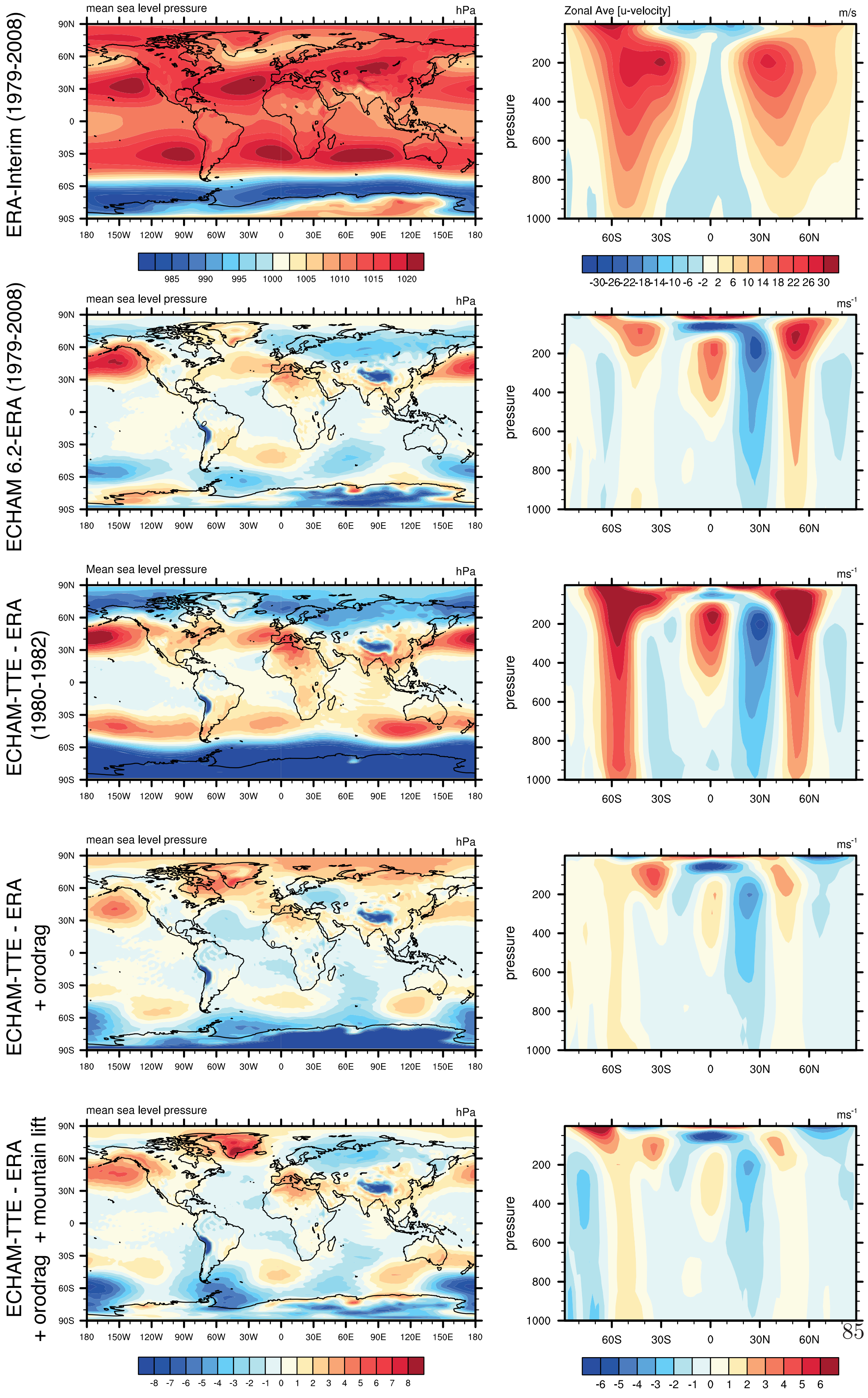
ERA-Interim (1979-2008)
ECHAM 6.2-ERA (1979-2008)
ECHAM-TTE - ERA (1980-1982)
ECHAM-TTE - ERA + orodrag
ECHAM-TTE - ERA + orodrag + mountain lift
mean sea level pressure
Mean sea level pressure
hPa
90N
60N
30N
0
30S
60S
90S
180
150W
120W
90W
60W
30W
0
30E
60E
90E
120E
150E
180
985
990
995
1000
1005
1010
1015
1020
Zonal Ave [u-velocity]
m/s
ms-1
pressure
200
400
600
800
1000
60S
30S
0
30N
60N
-30 -26 -22 -18 -14 -10 -6 -2 2 6 10 14 18 22 26 30
-8 -7 -6 -5 -4 -3 -2 -1 0 1 2 3 4 5 6 7 8
-6 -5 -4 -3 -2 -1 0 1 2 3 4 5 6

Figure 5.8: Global sea-level pressure fields and zonal mean winds

pressure gradient over the North Atlantic. Further notable pressure biases include a high-pressure bias over the Northern Pacific and a low-pressure bias at the equatorward edge of the southern hemispheric storm track. ECHAM 6.2 also overestimates the zonal wind velocities in the extratropical jetstreams (difference plots from ERA-Interim in the second row of Figure 5.8).

Running ECHAM-TTE without retuning any parameters leads to frequent model crashes, as wind velocities in the jetstream increase to and beyond the limit of numerical stability. At the same time, large-scale pressure gradients are substantially overestimated in ECHAM-TTE, which is expressed both in high-biased mean sea-level pressure in high-pressure regions and low biases in the storm track regions (third row of Figure 5.8). Note that since both the numerical instability and the model results were considered unacceptable, this configuration of the model was only run for three years. The model response to reduced surface drag is consistent with our physical understanding: Less surface drag leads to reduced cross-isobaric flow (Svensson and Holtslag 2009), which causes stronger pressure systems. Both the resulting stronger pressure gradients and the reduced drag itself contribute to stronger zonal winds. To alleviate these biases, we turn to the parametrisation of subgrid-scale orographic drag (Lott 1999) following Sandu et al. (2013).

In a first step, the tuning parameter for drag by orographically blocked flow is increased by almost an order of magnitude, from 0.2 to 1.2 (C_d from equation (2) in Lott (1999)). This change strongly reduces zonal wind velocities especially in the jet regions, resolving the numerical stability problem that initially occurred after introducing the new turbulence scheme, and alleviates the biases in mean sea-level pressure (fourth row of Figure 5.8). However, the parameter change introduces a new high-pressure bias in the Arctic. We therefore activate the parametrisation for mountain lift caused by subgrid-scale orography by increasing C_l from equation (5) in Lott (1999) from zero to 0.7, which largely removes the Arctic high-pressure bias. The parameter was set to zero to avoid generating new pressure biases around Antarctica when tuning ECHAM6. The parametrisation for drag caused by orographically blocked flow (Lott 1999) was also used to partly compensate for the overestimation of synoptic and planetary-scale activity in the reduced-diffusivity ECMWF model (Sandu et al. 2013). In that study, increasing turbulent orographic form drag (Beljaars et al. 2004) compensated for the circulation biases more efficiently. Turbulent orographic form drag is however not implemented in ECHAM, so that we could not easily test its effect in the climate model.

Both Sandu et al. (2013) and the present work suggest that the circulation biases that appear when surface drag is reduced to realistic values can be compensated in a satisfactory manner by retuning parts of the model related to effects of non-resolved orography. However, a total of three different parametrisations related to different processes have been proposed to achieve this effect, and other schemes and physical processes (e.g. gravity wave drag) could still be tested. Obtaining a parameter combination that results in a reasonably realistic large-scale mean flow is by no means equivalent to realistically representing the different physical processes. A physically realistic representation is however crucial for climate modelling, since confidence in climate change projections is largely justified by the physical understanding underlying the model formulations. As more emphasis is being placed on projections of future circulation changes, understanding and realistically representing the small-scale processes that control the large-scale circulation becomes an imperative for climate model development.

5.4.3 Neutral turbulent Prandtl number, temperature and precipitation

The most important temperature biases in ECHAM 6.2 are a widespread warm bias in near-surface air temperature over land, especially in the Northern Hemisphere, and a cold bias in the upper troposphere (second row in Figure 5.9). In ECHAM-TTE with a Prandtl number of 1, the extratropical cold biases in the upper troposphere/lower stratosphere are alleviated, whereas the tropical upper tropospheric cold bias becomes stronger (third row in Figure 5.9). Reducing the turbulent Prandtl number, i.e. increasing the ratio of heat to momentum flux causes a warming especially of the tropical and subtropical boundary layers, but also of the upper tropical troposphere that is coupled to the boundary layer through deep convection (fourth row in Figure 5.9). Despite the sea-surface temperatures being fixed to the observed values, a warm bias in 2 m temperatures over the ocean occurs when using ECHAM-TTE. 2 m temperatures are interpolated from surface and lowest-level atmospheric temperatures based on static stability (Geleyn 1988). They are therefore affected both by the changes in the surface-layer formulation and the warmer boundary layers in the new model version. Note that 2 m temperatures are also sensitive to technical choices made in the computation of sensible heat fluxes at the surface. Making a different choice in the future may compensate for much or all of the warm bias in oceanic 2 m temperatures that occurs in ECHAM-TTE.

The reduced cold bias in the extratropical upper troposphere and lower stratosphere in ECHAM-TTE is consistent with the reduction of excessive westerlies at the same levels shown in the previous section, as an exaggerated meridional temperature gradient would sustain a stronger thermal wind.

The warming and deepening of the tropical and subtropical boundary layers caused by the new turbulence scheme is associated with a drying of the boundary layer and therefore a reduction in cloudiness. This causes a global TOA imbalance of several Wm^{-2}. To reduce the amount of absorbed shortwave radiation and achieve radiative balance at top-of-atmosphere (Mauritsen et al. 2012), the entrainment rate for shallow convection in ECHAM-TTE is increased from $3 \cdot 10^{-4}$ to $10^{-3}\,\mathrm{m}^{-1}$. Reducing Pr_0

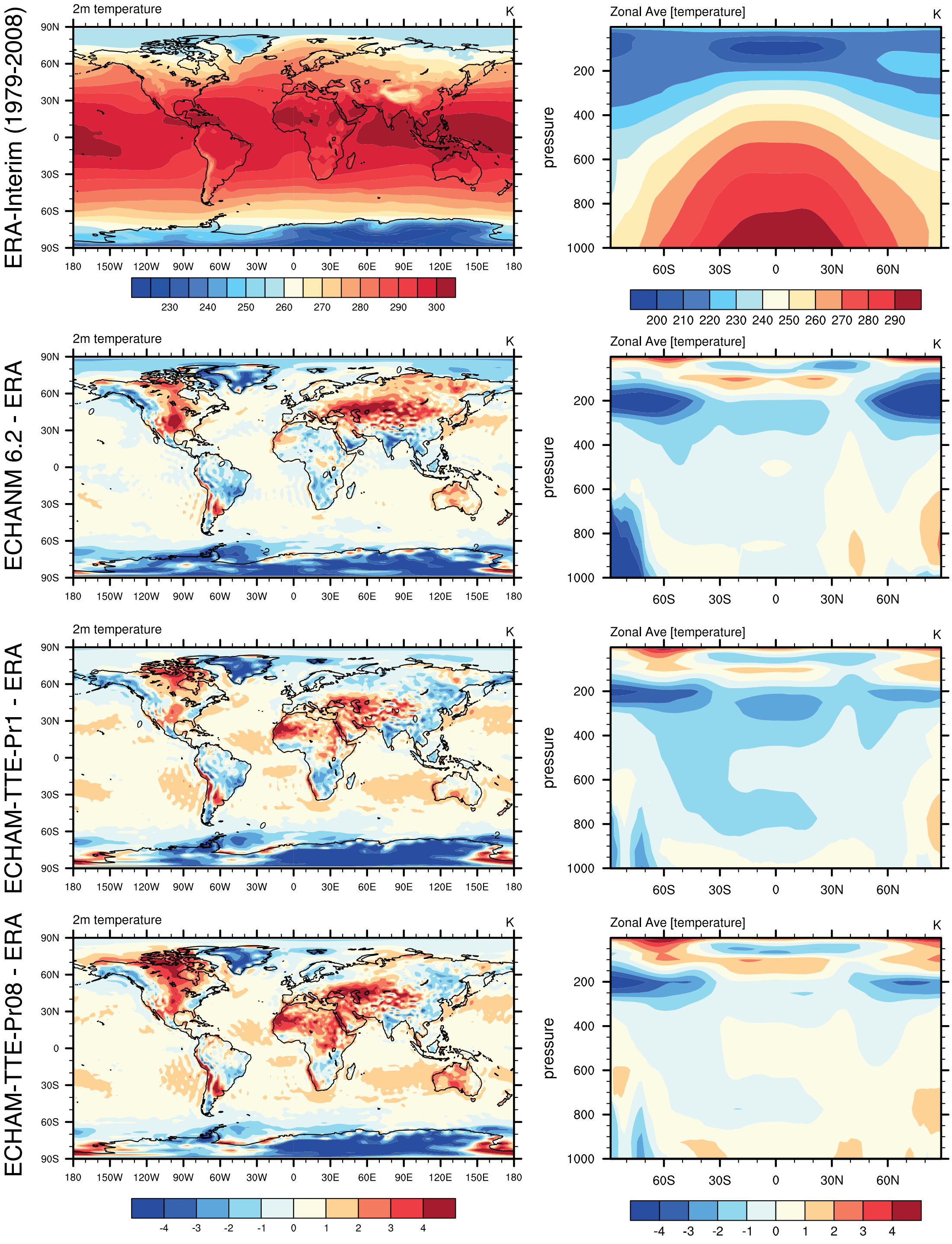
ERA-Interim (1979-2008)
ECHANM 6.2 - ERA
ECHAM-TTE-Pr1 - ERA
ECHAM-TTE-Pr08 - ERA
2m temperature
K
Zonal Ave [temperature]
pressure
90N
60N
30N
0
30S
60S
90S
180
150W
120W
90W
60W
30W
0
30E
60E
90E
120E
150E
180
200
400
600
800
1000
60S
30S
0
30N
60N
230 240 250 260 270 280 290 300
200 210 220 230 240 250 260 270 280 290
-4 -3 -2 -1 0 1 2 3 4

Figure 5.9: 2 m temperature and zonal mean atmospheric temperature

from 1 to 0.8 in ECHAM-TTE causes an increase in relative humidity in the boundary layer, increases in cloud cover in the stratocumulus regions where cloudiness is usually underestimated and in both liquid water path and reflected shortwave radiation in the storm track regions of both hemispheres. The lower Prandtl number thereby causes a reduction in absorbed shortwave radiation of about 1.2 Wm^{-2} in the global mean. A lower turbulent Prandtl number is also associated with a global increase in atmospheric water vapour and precipitation.

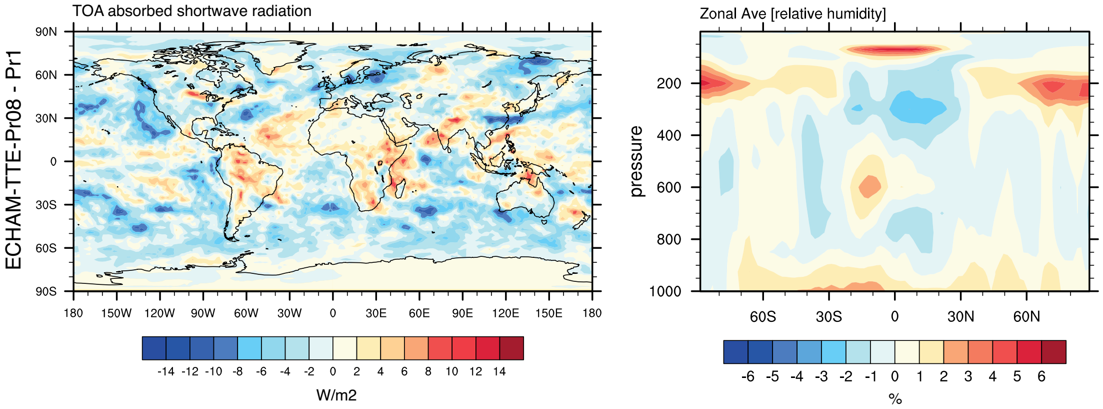
TOA absorbed shortwave radiation
ECHAM-TTE-Pr08 - Pr1
90N
60N
30N
0
30S
60S
90S
180
150W
120W
90W
60W
30W
0
30E
60E
90E
120E
150E
180
-14 -12 -10 -8 -6 -4 -2 0 2 4 6 8 10 12 14
W/m2
Zonal Ave [relative humidity]
pressure
200
400
600
800
1000
60S
30S
0
30N
60N
-6 -5 -4 -3 -2 -1 0 1 2 3 4 5 6
%

Figure 5.10: Changes in absorbed shortwave radiation at TOA and zonal mean relative humidity between $Pr_0 = 0.8$ and $Pr_0 = 1$

ECHAM uses different roughness lengths for heat and momentum over ocean, which could be thought of as representing the deviation of the Prandtl number from unity. However, setting these roughness lengths to an equal value hardly affects the variables that are affected by changes in the Prandtl number (not shown). The model is evaluated against ERA-Interim, a reanalysis product derived using the IFS Cy31r1, which also assumes a neutral turbulent Prandtl number of one in the surface layer. This evaluation might thus be biased in favour of a larger neutral Prandtl number. However, smaller values of Pr0 also result in high biases in atmospheric water vapour and globally averaged precipitation compared to estimates based on satellite observations.

Table 5.2: Values of tuning parameters changed between ECHAM 6.2 and ECHAM-TTE

Tuning parameter	Entrainment rate for shallow convection (entrscv)	Subgrid-scale orographic drag (gkdrag)	Subgrid-scale orographic lift (gklift)
value in ECHAM 6.2	$3 \cdot 10^{-4}\,\mathrm{m}^{-1}$	0.2	0
value in ECHAM-TTE	$1 \cdot 10^{-3}\,\mathrm{m}^{-1}$	1.2	0.7

5.5 Discussion and Conclusions

ECHAM6 overestimates diffusivity and thus surface drag in stably stratified boundary layers, as do many other climate and numerical weather prediction models (Cuxart et al. 2006). We have implemented a new turbulence scheme based on the concept of total turbulent energy (Mauritsen et al. 2007), which generates surface drag within the range of large-eddy simulations for an idealised single-column case. The new scheme also includes a more physically-based turbulent length scale and does generate entrainment fluxes at the top of a growing dry convective boundary layer, which the old turbulence scheme failed to achieve. Compared to a direct numerical simulation of a dry free-convective boundary layer (Garcia and Mellado 2014), ECHAM-TTE now substantially overestimates entrainment flux. We attribute this to interactions between stratification and convectively driven turbulence in the capping layer that are not yet satisfactorily represented in the scheme.

In agreement with our expectations and results from the ECMWF model (Sandu et al. 2013), reducing turbulent surface drag to realistic values leads to an unrealistic increase in large-scale pressure gradients and zonal wind speeds. These biases can largely be compensated for by increasing the parametrised drag caused by orographically blocked flow and mountain lift forces (Lott 1999). The warming and deepening of marine boundary layers in ECHAM-TTE is probably the cause for a reduced shortwave cloud radiative effect, which leads to an imbalance in top-of-atmosphere radiation. Reducing the entrainment rate for shallow convection largely compensates for this (Mauritsen et al. 2012). Reducing the neutral turbulent Prandtl number, i.e. the ratio of eddy diffusivity for momentum to eddy conductivity for heat from unity to 0.8 leads to further warming, but also to an increase in relative humidity in the tropical and subtropical boundary layers and thus reduces absorbed shortwave radiation.

To obtain more realistic values for the entrainment flux, a more detailed representation of the capping layer would be required. First steps in that direction could be to 1) obtain the height of the dry thermal top by interpolation rather than setting it to a full level height and 2) combine the diffusivities obtained using the formulations for the stable and convective case to compute the diffusivity across the capping layer.

While much work has been done on different aspects of the ECHAM climate model physics over the last decade, the boundary-layer scheme has not been changed since more than twenty years. It is therefore to be expected that the model is in many ways adapted to the current boundary layer scheme, and even physically reasonable changes may lead to unintended results elsewhere. Once a final version of the TTE scheme has been developed, its interactions with the surface, shallow and deep convection and large-scale cloud parametrisations has to be analysed to properly integrate the scheme into the model.

The sensitivity of the modelled climate to the assumed neutral turbulent Prandtl number should be further investigated. This includes the interaction with the surface flux computation, where different choices in the discretisation of surface fluxes may compensate for the biases currently associated with a lower Prandtl number, and a possible effect of different Prandtl numbers on cloud feedbacks and thus climate sensitivity. Regarding the interaction of boundary-layer drag and the large-scale circulation, the present understanding is probably sufficient to retune a climate model after reducing surface drag to a realistic range. However, obtaining a realistic large-scale circulation in the present-day climate that might be the result of new compensating errors would inspire little confidence in projections of future circulation changes and their interactions with radiative processes. A deeper process-based understanding of the role of boundary-layer drag, orographic features and possibly gravity waves for the large scale circulation thus remains to be established.

Chapter 6

Conclusions

The present thesis investigates properties of and processes in the Arctic boundary layer that shape the state of Arctic climate and its susceptibility to changes. One of these properties is the vertical structure of the lower Arctic atmosphere, which has long been known to be dominated by stable stratification and the presence of temperature inversions (Sverdrup 1933). Our feedback analysis shows that this stratification is the single most important reason for Arctic amplification of climate change in contemporary models, because it confines warming to a shallow layer close to the surface, letting little heat escape to space (lapse-rate feedback). Furthermore, at the cold Arctic surface temperatures, a smaller warming than in the tropics is required to obtain a globally uniform increase in emitted longwave radiation (Planck feedback). In contrast to a widespread opinion, the lapse-rate and Planck feedbacks contribute more to Arctic amplification than the surface albedo feedback associated to the retreat of snow and ice.

While static stability and the presence of temperature inversions are typical of the Arctic boundary layer, especially in winter, explaining the variations in observed inversion strength and height and their relationship to other boundary-layer variables and surface fluxes has been a considerable challenge. Both observations (Persson et al. 1999; Tjernström 2012) and an idealised single-column experiment (Chapter 4) show that the aggregate state of cloud water determines in which of two distinct states the Arctic winter boundary layer is. As relatively warm and moist air masses are advected into the Arctic and cool radiatively, the presence of liquid water in the atmospheric column maintains a cloudy state with weak, elevated inversions, whereas the lack of cloud liquid water leads to a radiatively clear state with stronger, surface-based temperature inversions. Climate models that lack cloud liquid water in Arctic winter fail to represent the cloudy state of the boundary layer, resulting in substantial biases in mean inversion strength.

Within the radiatively clear state of the boundary layer, conductive heat fluxes through snow and ice and downward turbulent heat fluxes largely determine the strength of temperature inversions. Many large-scale models are known to overestimate turbulent fluxes under stable stratification (Cuxart et al. 2006). While more realistic fluxes would be beneficial for the representation of the surface energy budget and near-surface temperatures, they often deteriorate the representation of the large-scale flow in models, which has so far impeded their implementation in weather and climate models (Viterbo et al. 1999; Sandu et al. 2013).

Implementing a total turbulent energy scheme (Mauritsen et al. 2007) into ECHAM6, we obtain a climate model that realistically represents turbulent fluxes in the stable boundary layer. The TTE scheme uses empirical stability functions directly derived from observations and has more physical representations of the mixing length and of the inversion capping a dry convective boundary layer. As expected based on prior studies, the new model version ECHAM-TTE substantially overestimates zonal winds and large-scale pressure gradients. However, these biases can be largely eliminated by enhancing the parametrised effects of non-resolved orography.

Past scientific discoveries and developments that prepared the ground for extending our understanding of Arctic boundary layer processes and their relationship to climate change in the present thesis include the fundamental understanding of how the emission of longwave radiation depends on temperature (Planck 1901), the very first climate change experiments in general circulation models (Manabe and Wetherald 1975), the development of radiative kernels as a tool for feedback analysis (Soden et al. 2008) and a series of studies on Arctic amplification continuing to the present (e.g. Crook et al. 2011; Taylor et al. 2013) as well as earlier model studies on the radiative cooling of air masses advected into the Arctic (Wexler 1936; Curry 1983) and observations of the Arctic boundary layer (e.g. Persson et al. 2002; Tjernström and Graversen 2009). We have added to this knowledge and these methods by using the inverted temperature kernel to compute local warming contributions of individual feedbacks and by developing a process-based diagnostic to evaluate the representation of the Arctic winter boundary layer in climate models.

A supposed correlation between strong present-day temperature inversions and weak future Arctic warming in CMIP3 models (Boé et al. 2009) is inconsistent with our physical understanding of temperature inversions contributing to a positive lapse-rate feedback in the Arctic. A permutation test reveals that the correlation is no longer significant when accounting for self-correlation in the analysed variables. Beyond the specific statistical artifact, this should serve as a reminder that many variables display seemingly significant correlations by pure chance in huge data sets such as the CMIP archives (Nuzzo 2014). Any attempt to constrain future model behaviour based on model performance in the present-day climate should therefore be based on a solid physical understanding of the underlying processes.

The work carried out for this thesis offers several threads for further investigation. The radiative cooling of air advected into the Arctic that drives the formation of Arctic air masses is currently being investigated in a single-column model intercomparison, and large-eddy simulations of the same case would be a great asset for further analysis and investigation. While very challenging to obtain, a Lagrangian set of in-situ and remote sensing observations following such an air mass on its trajectory would be a great foundation for a follow-up case based on and directly comparable to observations.

The formation of Arctic air masses also feeds back on the circulation as radiative cooling at the cloud level and surface drives the formation of cold-core anticyclones. Investigating this coupling would make for an interesting Arctic contribution to the world climate research program's grand challenge on how clouds and radiation couple to circulation (Bony and Stevens 2012).

We need to understand to what extent excessive turbulent drag in weather and climate models actually compensates for a lack of orographic drag, and how the impacts of both processes on the large-scale circulation differ in order to obtain a physically realistic representation of the large-scale flow and thereby build confidence in projections of future circulation changes.

The boundary layer mediates all exchanges of heat, momentum, and matter between the Earth's surface and its atmosphere. It remains crudely resolved in models of the general circulation, but is crucial for low-level clouds and surface drag, and thus both the thermodynamic and dynamic aspects of climate change. Understanding the physical processes that shape the surface-atmosphere coupling is therefore of paramount importance for climate science. Observing and modelling the Arctic boundary layer in the context of global climate change, we can make a contribution to meeting that challenge in the decades to come.

Bibliography

Abbot, D. S. and E. Tziperman, 2008: A high-latitude convective cloud feedback and equable climates. *Q. J. Roy. Met. Soc.*, **134 (630)**, 165–185, doi:10.1002/qj.211.

ACIA, 2004: *Impacts of a Warming Arctic-Arctic Climate Impact Assessment*. Cambridge University Press.

Andreas, E. L., P. S. Guest, P. O. G. Persson, C. W. Fairall, T. W. Horst, R. E. Moritz, and S. R. Semmer, 2002: Near-surface water vapor over polar sea ice is always near ice saturation. *J. Geophys. Res.: Oceans*, **107 (C10)**, SHE 8–1–SHE 8–15, doi:10.1029/2000JC000411.

Angevine, W. M., H. Jiang, and T. Mauritsen, 2010: Performance of an eddy diffusivity-mass flux scheme for shallow cumulus boundary layers. *Mon. Wea. Rev.*, **138 (7)**, 2895–2912.

Arrhenius, S., 1896: On the influence of carbonic acid in the air upon the temperature of the ground. *The London, Edinburgh, and Dublin Philosophical Magazine and Journal of Science*, **41 (251)**, 237–276.

Barrett, A., 2012: Why can't models simulate mixed-phase clouds correctly? Ph.D. thesis, University of Reading.

Barron, E. J., 1983: A warm, equable cretaceous: The nature of the problem. *Earth-Science Rev.*, **19 (4)**, 305–338, doi:10.1016/0012-8252(83)90001-6.

Beare, R. J., et al., 2006: An intercomparison of large-eddy simulations of the stable boundary layer. *Boundary-Layer Met.*, **118 (2)**, 247–272.

Bekryaev, R. V., I. V. Polyakov, and V. A. Alexeev, 2010: Role of polar amplification in long-term surface air temperature variations and modern arctic warming. *J. Climate*, **23 (14)**, 3888–3906.

Beljaars, A., 1994: The parametrization of surface fluxes in large-scale models under free convection. *Q. J. Roy. Met. Soc.*, **121 (522)**, 255–270.

Beljaars, A., A. R. Brown, and N. Wood, 2004: A new parametrization of turbulent orographic form drag. *Q. J. Roy. Met. Soc.*, **130 (599)**, 1327–1347.

Beljaars, A. and P. Viterbo, 1998: Role of the boundary layer in a numerical weather prediction model. *Clear and Cloudy Boundary Layers*, A. Holtslag and P. Duynkerke, Eds., Royal Netherlands Academy of Arts and Sciences, 297–304.

Bergeron, T., 1935: On the physics of clouds and precipitation. *Proc. 5th Assembly*, UGGI, Lisbon, 156–178.

Bintanja, R., R. Graversen, and W. Hazeleger, 2011: Arctic winter warming amplified by the thermal inversion and consequent low infrared cooling to space. *Nat. Geosci.*, **4**, 758–761.

Bintanja, R. and E. van der Linden, 2013: The changing seasonal climate in the arctic. *Sci. Rep.*, **3**, doi:10.1038/srep01556.

Bintanja, R., E. van der Linden, and W. Hazeleger, 2012: Boundary layer stability and Arctic climate change: a feedback study using EC-Earth. *Climate Dyn.*, **39 (11)**, 2659–2673, doi:10.1007/s00382-011-1272-1.

Blackadar, A. K., 1962: The vertical distribution of wind and turbulent exchange in a neutral atmosphere. *J. Geophys. Res.*, **67 (8)**, 3095–3102.

Block, K. and T. Mauritsen, 2013: Forcing and Feedback in the MPI-ESM-LR coupled model under abruptly quadrupled CO2. *J. Adv. Model. Earth Syst.*, doi: 10.1002/jame.20041.

Boé, J., A. Hall, and X. Qu, 2009: Current GCMs' Unrealistic Negative Feedback in the Arctic. *J. Climate*, **22**, 4682–4695.

Bogenschutz, P. A., A. Gettelman, H. Morrison, V. E. Larson, C. Craig, and D. P. Schanen, 2013: Higher-order turbulence closure and its impact on climate simulations in the community atmosphere model. *J. Climate*, **26 (23)**, 9655–9676.

Bony, S. and B. Stevens, 2012: Clouds, circulation and climate sensitivity: How the interaction between clouds, greenhouse gases and aerosols affect temperature and precipitation in a changing climate. available online at http://wcrp-climate.org/images/documents/grand_challenges/GC4_Clouds_14nov2012.pdf, last accessed 19th March 2014.

Brinkop, S. and E. Roeckner, 1995: Sensitivity of a general circulation model to parameterizations of cloud–turbulence interactions in the atmospheric boundary layer. *Tellus A*, **47 (2)**, 197–220.

Cesana, G., J. Kay, H. Chepfer, J. English, and G. de Boer, 2012: Ubiquitous low-level liquid-containing Arctic clouds: New observations and climate model constraints from CALIPSO-GOCCP. *Geophys. Res. Letters*, **39 (20)**, L20 804.

Chapman, W. L. and J. E. Walsh, 1993: Recent variations of sea ice and air temperature in high latitudes. *Bull. Am. Met. Soc.*, **74 (1)**, 33–47.

Cowtan, K. and R. G. Way, 2013: Coverage bias in the hadcrut4 temperature series and its impact on recent temperature trends. *Q. J. Roy. Met. Soc.*, doi:10.1002/qj.2297.

Crook, J. A., P. M. Forster, and N. Stuber, 2011: Spatial Patterns of Modeled Climate Feedback and Contributions to Temperature Response and Polar Amplification. *J. Climate*, **24**, 3575–3592.

Curry, J., 1983: On the Formation of Continental Polar Air. *J. Atmos. Sci.*, **40**, 2278–2292.

Curry, J., 1986: Interactions among turbulence, radiation and microphysics in Arctic stratus clouds. *J. Atmos. Sci.*, **43 (1)**, 90–106.

Cuxart, J., et al., 2006: Single-column model intercomparison for a stably stratified atmospheric boundary layer. *Boundary-layer Met.*, **118 (2)**, 273–303.

Dahl-Jensen, D., K. Mosegaard, N. Gundestrup, G. D. Clow, S. J. Johnsen, A. W. Hansen, and N. Balling, 1998: Past temperatures directly from the greenland ice sheet. *Science*, **282 (5387)**, 268–271, doi:10.1126/science.282.5387.268.

Devasthale, A., J. Sedlar, and M. Tjernström, 2011: Characteristics of water-vapour inversions observed over the arctic by atmospheric infrared sounder (airs) and radiosondes. *Atmos. Chem. Phys*, **11**, 9813–9823.

Donner, L., et al., 2011: The dynamical core, physical parameterizations, and basic simulation characteristics of the atmospheric component AM3 of the GFDL global coupled model CM3. *J. Climate*, **24 (13)**, 3484–3519.

Findeisen, W., 1938: Die kolloidmeteorologischen vorgänge bei der niederschlagsbildung. *Meteor. Z*, **55**, 121–133.

Francis, J. A. and S. J. Vavrus, 2012: Evidence linking arctic amplification to extreme weather in mid-latitudes. *Geophys. Res. Lett.*, **39 (6)**.

Fridlind, A. M., B. Van Diedenhoven, A. S. Ackerman, A. Avramov, A. Mrowiec, H. Morrison, P. Zuidema, and M. D. Shupe, 2012: A fire-ace/sheba case study of mixed-phase arctic boundary layer clouds: entrainment rate limitations on rapid primary ice nucleation processes. *J. Atmos. Sci.*, **69 (1)**, 365–389.

Garcia, J. and J.-P. Mellado, 2014: The two-layer structure of the entrainment zone in the convective boundary layer. *J. Atmos. Sci.*, accepted, doi:10.1175/JAS-D-13-0148.1.

Geleyn, J.-F., 1988: Interpolation of wind, temperature and humidity values from model levels to the height of measurement. *Tellus A*, **40 (4)**, 347–351.

Gent, P., et al., 2011: The community climate system model version 4. *J. Climate*, **24 (19)**, 4973–4991.

Gettelman, A., V. Walden, L. Miloshevich, W. Roth, and B. Halter, 2006: Relative humidity over Antarctica from radiosondes, satellites, and a general circulation model. *J. Geophys. Res.*, **111 (D9)**, D09S13.

Graversen, R. G. and M. Wang, 2009: Polar amplification in a coupled climate model with locked albedo. *Climate Dyn.*, **33 (5)**, 629–643.

Hall, A., 2004: The role of surface albedo feedback in climate. *J. Climate*, **17 (7)**, 1550–1568.

Hansen, J., M. Sato, and R. Ruedy, 1997: Radiative forcing and climate response. *J. Geophys Res.: Atmos.*, **102 (D6)**, 6831–6864.

Held, I., 1978: The Tropospheric Lapse Rate and Climatic Sensitivity: Experiments with a Two-Level Atmospheric Model. *J. Atmos. Sci.*, **35**, 2083–2098.

Held, I. and K. Shell, 2012: Using relative humidity as a state variable in climate feedback analysis. *J. Climate*, **25**, 2578–2582.

Held, I. M. and B. J. Soden, 2006: Robust responses of the hydrological cycle to global warming. *J. Climate*, **19 (21)**, 5686–5699.

Holland, M. and C. Bitz, 2003: Polar amplification of climate change in coupled models. *Climate Dyn.*, **21 (3)**, 221–232.

Holtslag, A., et al., 2013: Stable atmospheric boundary layers and diurnal cycles-challenges for weather and climate models. *Bull. Am. Met. Soc.*, **94**, 1691–1706.

Honda, M., J. Inoue, and S. Yamane, 2009: Influence of low arctic sea-ice minima on anomalously cold eurasian winters. *Geophys. Res. Let.*, **36 (8)**, L08 707, doi: 10.1029/2008GL037079.

Hourdin, F., et al., 2012: LMDZ5B: the atmospheric component of the IPSL climate model with revisited parameterizations for clouds and convection. *Climate Dyn.*, doi: 10.1007/s00382-012-1343-y.

Huybrechts, P., 2002: Sea-level changes at the lgm from ice-dynamic reconstructions of the greenland and antarctic ice sheets during the glacial cycles. *Quaternary Sci. Rev.*, **21 (1)**, 203–231.

Hwang, Y.-T., D. M. Frierson, and J. E. Kay, 2011: Coupling between arctic feedbacks and changes in poleward energy transport. *Geophys. Res. Lett.*, **38 (17)**, L17 704, doi:10.1029/2011GL048546.

IPCC, 2007: *Climate Change 2007: The Physical Science Basis. Contribution of Working Group I to the Fourth Assessment Report of the Intergovernmental Panel on Climate Change*. Cambridge University Press, Cambridge, UK.

IPCC, 2013: *Climate Change 2013: The Physical Science Basis. Contribution of Working Group I to the Fifth Assessment Report of the Intergovernmental Panel on Climate Change*. Cambridge University Press, Cambridge, UK.

Jones, P., M. New, D. Parker, S. Martin, and I. Rigor, 1999: Surface air temperature and its changes over the past 150 years. *Rev. Geophys.*, **37 (2)**, 173–199.

Jungclaus, J., H. Haak, M. Latif, and U. Mikolajewicz, 2005: Arctic-North Atlantic interactions and multidecadal variability of the meridional overturning circulation. *J. Climate*, **18 (19)**, 4013–4031.

Kays, W. M., 1994: Turbulent prandtl number. where are we? *ASME Transactions Journal of Heat Transfer*, **116**, 284–295.

Kenney, B. C., 1982: Beware of spurious self-correlations! *Water Resour. Res.*, **18 (4)**, 1041–1048.

Khodri, M., Y. Leclainche, G. Ramstein, P. Braconnot, O. Marti, and E. Cortijo, 2001: Simulating the amplification of orbital forcing by ocean feedbacks in the last glaciation. *Nature*, **410 (6828)**, 570–574.

King, J., W. Connolley, and S. Derbyshire, 2001: Sensitivity of modelled antarctic climate to surface and boundary-layer flux parametrizations. *Q. J. Roy. Met. Soc.*, **127 (573)**, 779–794.

Klein, S. A., et al., 2009: Intercomparison of model simulations of mixed-phase clouds observed during the arm mixed-phase arctic cloud experiment. i: Single-layer cloud. *Q. J. Roy. Met. Soc.*, **135 (641)**, 979–1002.

Klipp, C. L. and L. Mahrt, 2004: Flux-gradient relationship, self-correlation and intermittency in the stable boundary layer. *Q. J. Roy. Meteor. Soc.*, **130**, 2087–2103.

Köhler, M., M. Ahlgrimm, and A. Beljaars, 2011: Unified treatment of dry convective and stratocumulus-topped boundary layers in the ecmwf model. *Q. J. Roy. Met. Soc.*, **137 (654)**, 43–57.

Kondo, J., O. Kanechika, and N. Yasuda, 1978: Heat and momentum transfers under strong stability in the atmospheric surface layer. *J. Atmos. Sci.*, **35 (6)**, 1012–1021.

Liu, G., Y. Liu, and S. Endo, 2013: Evaluation of surface flux parameterizations with long-term arm observations. *Mon. Wea. Rev.*, **141 (2)**, 773–797.

Lohmann, U. and E. Roeckner, 1996: Design and performance of a new cloud microphysics scheme developed for the ECHAM general circulation model. *Climate Dyn.*, **12 (8)**, 557–572.

Lott, F., 1999: Alleviation of stationary biases in a gcm through a mountain drag parameterization scheme and a simple representation of mountain lift forces. *Mon. Wea. Rev.*, **127 (5)**, 788–801.

Louis, J.-F., 1979: A parametric model of vertical eddy fluxes in the atmosphere. *Boundary-Layer Met.*, **17 (2)**, 187–202.

Manabe, S. and R. Wetherald, 1975: The effects of doubling the CO2 concentration on the climate of a general circulation model. *J. Atmos. Sci.*, **32**, 3–15.

Manabe, S. and R. T. Wetherald, 1980: On the distribution of climate change resulting from an increase in co2 content of the atmosphere. *J. Atmos. Sci.*, **37 (1)**, 99–118.

Manzo, K., 2010: Beyond polar bears? re-envisioning climate change. *Met. Appl.*, **17 (2)**, 196–208.

Masson-Delmotte, V., et al., 2006: Past and future polar amplification of climate change: climate model intercomparisons and ice-core constraints. *Climate Dyn.*, **26 (5)**, 513–529.

Mauritsen, T. and G. Svensson, 2007: Observations of stably stratified shear-driven atmospheric turbulence at low and high richardson numbers. *J. Atmos. Sci.*, **64 (2)**, 645–655.

Mauritsen, T., G. Svensson, S. S. Zilitinkevich, I. Esau, L. Enger, and B. Grisogono, 2007: A total turbulent energy closure model for neutrally and stably stratified atmospheric boundary layers. *J. Atmos. Sci.*, **64 (11)**, 4113–4126.

Mauritsen, T., et al., 2012: Tuning the climate of a global model. *J. Adv. Model. Earth Sys.*, **4**, M00A01, doi:10.1029/2012MS000154.

Medeiros, B., C. Deser, R. Tomas, and J. Kay, 2011: Arctic inversion strength in climate models. *J. Climate*, **24**, 4733–4740.

Météo France, 2009: ARPEGE-Climat V5.1 Algorithmic documentation. Tech. rep., Météo France/CNRM.

Miller, M., A. Beljaars, and T. Palmer, 1992: The sensitivity of the ecmwf model to the parameterization of evaporation from the tropical oceans. *J. Climate*, **5 (5)**, 418–434.

Monin, A. and A. Obukhov, 1954: Basic laws of turbulent mixing in the surface layer of the atmosphere. *Contrib. Geophys. Inst. Acad. Sci. USSR*, **151**, 163–187.

Morrison, H., G. de Boer, G. Feingold, J. Harrington, M. Shupe, and K. Sulia, 2012: Resilience of persistent Arctic mixed-phase clouds. *Nat. Geosci.*, **4**, 11–17, doi: 10.1038/ngeo1332.

Notz, D., V. Brovkin, and M. Heimann, 2013: Arctic: Uncertainties in methane link. *Nature*, **500 (7464)**, 529–529.

Nuzzo, R., 2014: Scientific method: Statistical errors. *Nature*, **506**, 150–152, doi: 10.1038/506150a.

Overland, J. and P. Guest, 1991: The Arctic snow and air temperature budget over sea ice during winter. *J. Geophys. Res.*, **96 (C3)**, 4651–4662.

Pavelsky, T., J. Boé, A. Hall, and E. Fetzer, 2011: Atmospheric inversion strength over polar oceans in winter regulated by sea ice. *Climate Dyn.*, **36 (5)**, 945–955.

Pearson, K., 1896: Mathematical Contributions to the Theory of Evolution.–On a Form of Spurious Correlation Which May Arise When Indices Are Used in the Measurement of Organs. *Proc. Roy. Soc. London*, **60**, 489–498.

Persson, P., C. Fairall, E. Andreas, P. Guest, and D. Perovich, 2002: Measurements near the Atmospheric Surface Flux Group tower at SHEBA: Near-surface conditions and surface energy budget. *J. Geophys. Res*, **107 (10.1029)**.

Persson, P., T. Uttal, J. Intrieri, C. Fairall, E. Andreas, and P. Guest, 1999: Observations of large thermal transitions during the arctic night from a suite of sensors at sheba. *Third Symposium on Integrated Observing Systems Am. Meteorol. Soc. Dallas, Tex.*

Petoukhov, V. and V. A. Semenov, 2010: A link between reduced barents-kara sea ice and cold winter extremes over northern continents. *J. Geophys. Res.: Atmos.*, **115 (D21)**.

Pithan, F. and T. Mauritsen, 2013: Comments on'current gcms' unrealistic negative feedback in the arctic'. *J. Climate*, **26 (19)**, 7783–7788.

Planck, M., 1901: Ueber das gesetz der energieverteilung im normalspectrum. *Annalen der Physik*, **309 (3)**, 553–563.

Richardson, L., 1920: The supply of energy to and from atmospheric eddies. *Proc. Roy. Soc. A*, **97 (686)**, 354–373.

Rotstayn, L., B. Ryan, and J. Katzfey, 2000: A scheme for calculation of the liquid fraction in mixed-phase stratiform clouds in large-scale models. *Mon. wea. rev.*, **128 (4)**, 1070–1088.

Sandu, I., A. Beljaars, P. Bechtold, T. Mauritsen, and G. Balsamo, 2013: Why is it so difficult to represent stably stratified conditions in numerical weather prediction (nwp) models? *J. Adv. Mod. Earth Syst.*

Satoh, M., T. Matsuno, H. Tomita, H. Miura, T. Nasuno, and S. Iga, 2008: Nonhydrostatic icosahedral atmospheric model (nicam) for global cloud resolving simulations. *J. Comput. Phys.*, **227 (7)**, 3486–3514.

Schmidt, G., et al., 2006: Present-day atmospheric simulations using GISS ModelE: Comparison to in situ, satellite, and reanalysis data. *J. Climate*, **19 (2)**, 153–192.

Schneider, S. and R. Dickinson, 1974: Climate modeling. *Rev. Geophys. Space Phys.*, **12 (3)**, 447–493.

Schulz, J.-P., L. Dümenil, and J. Polcher, 2001: On the land surface-atmosphere coupling and its impact in a single-column atmospheric model. *J. Appl. Met.*, **40 (3)**, 642–663.

Scoccimarro, E., et al., 2011: Effects of Tropical Cyclones on Ocean Heat Transport in a High-Resolution Coupled General Circulation Model. *J. Climate*, **24 (16)**, 4368–4384.

Screen, J. A. and I. Simmonds, 2010: The central role of diminishing sea ice in recent arctic temperature amplification. *Nature*, **464 (7293)**, 1334–1337.

Sedlar, J., M. D. Shupe, and M. Tjernström, 2012: On the relationship between thermodynamic structure and cloud top, and its climate significance in the arctic. *J. Climate*, **25 (7)**.

Serreze, M. and R. Barry, 2011: Processes and impacts of Arctic amplification: A research synthesis. *Global Planet. Change*, **77**, 85–96.

Serreze, M., R. Schnell, and J. Kahl, 1992: Low-level temperature inversions of the Eurasian Arctic and comparisons with Soviet drifting station data. *J. Climate*, **5 (6)**, 615–629.

Serreze, M. C. and J. A. Francis, 2006: The arctic amplification debate. *Climatic Change*, **76 (3-4)**, 241–264.

Shell, K., J. Kiel, and C. Shields, 2008: Using the Radiative Kernel Technique to Calculate Climate Feedbacks in NCAR's Community Atmospheric Model. *J. Climate*, **21**, 2269–2283.

Simmons, A., S. Uppala, D. Dee, and S. Kobayashi, 2007: ERA-Interim: New ECMWF reanalysis products from 1989 onwards. *ECMWF newsletter*, **110**, 25–35.

Smagorinsky, J., S. Manabe, and J. L. Holloway Jr, 1965: Numerical results from a nine-level general circulation model of the atmosphere 1. *Mon. Wea. Rev.*, **93 (12)**, 727–768.

Smedman, A.-S., 1988: Observations of a multi-level turbulence structure in a very stable atmospheric boundary layer. *Boundary-Layer Met.*, **44 (3)**, 231–253.

Soden, B., I. Held, R. Colman, K.Shell, J. Kiel, and C. Shields, 2008: Quantifying climate feedbacks using radiative kernels. *J. Climate*, **21**, 3504–3520.

Solomon, A., M. D. Shupe, O. Persson, H. Morrison, T. Yamaguchi, P. M. Caldwell, and G. de Boer, 2014: The sensitivity of springtime arctic mixed-phase stratocumulus clouds to surface layer and cloud-top inversion layer moisture sources. *J. Atmos. Sci.*, **71 (2)**, 574–595.

Sorteberg, A., V. Kattsov, J. E. Walsh, and T. Pavlova, 2007: The Arctic surface energy budget as simulated with the IPCC AR4 AOGCMs. *Climate Dyn.*, **29 (2)**, 131–156.

Spielhagen, R. F., et al., 2011: Enhanced modern heat transfer to the arctic by warm atlantic water. *Science*, **331 (6016)**, 450–453, doi:10.1126/science.1197397.

Sterk, H., G. Steeneveld, and A. Holtslag, 2013: The role of snow-surface coupling, radiation, and turbulent mixing in modeling a stable boundary layer over arctic sea ice. *J.Geophys. Res.: Atmos.*, **118**, 1199–1217.

Stevens, B., et al., 2013: The Atmospheric Component of the MPI-M Earth System Model: ECHAM6. *J. Adv. Model. Earth Syst.*, doi:10.1002/jame.20015.

Stramler, K., A. Del Genio, and W. Rossow, 2011: Synoptically driven Arctic winter states. *J. Climate*, **24 (6)**, 1747–1762.

Svensson, G. and A. A. Holtslag, 2009: Analysis of model results for the turning of the wind and related momentum fluxes in the stable boundary layer. *Boundary-layer Met.*, **132 (2)**, 261–277.

Svensson, G. and J. Karlsson, 2011: On the Arctic Wintertime Climate in Global Climate Models. *J. Climate*, **24 (22)**, 5757–5771.

Sverdrup, H., 1933: *Meteorology*, The Norwegian North Polar expedition with the 'Maud' 1918-1925, scientific results, Vol. II. Geophysical Institute, Bergen, Norway.

Taylor, K., R. Stouffer, and G. Meehl, 2012: An overview of CMIP5 and the experiment design. *Bull. Am. Met. Soc.*, **93 (4)**, 485.

Taylor, P. C., M. Cai, A. Hu, J. Meehl, W. Washington, and G. J. Zhang, 2013: A decomposition of feedback contributions to polar warming amplification. *J. Climate*, **26**, 7023–7043, doi:10.1175/JCLI-D-12-00696.1.

Tjernström, M., 2012: The Arctic Ocean boundary layer: Interactions with the sea-ice surface and clouds. *ECMWF GABLS workshop on diurnal cycles and the stable boundary layer, 7-10 November 2011*, European Centre for Medium-Range Weather Forecasts.

Tjernström, M. and R. Graversen, 2009: The vertical structure of the lower Arctic troposphere analysed from observations and the ERA-40 reanalysis. *Q. J. Roy. Met. Soc.*, **135 (639)**, 431–443.

Turner, J. K. and J. R. Gyakum, 2011: The Development of Arctic Air Masses in Northwest Canada and Their Behaviour in a Warming Climate. *J. Climate*, **24**, 4818–4633, doi:10.1175/2011JCLI3855.1.

Uppala, S., et al., 2005: The ERA-40 re-analysis. *Q. J. Roy. Met. Soc.*, **131 (612)**, 2961–3012.

Uttal, T., et al., 2002: Surface heat budget of the arctic ocean. *Bull. Am. Met. Soc.*, **83 (2)**.

Vavrus, S., 2004: The Impact of Cloud Feedbacks on Arctic Climate under Greenhouse Forcing. *J. Climate*, **17 (3)**, 603–615.

Viterbo, P., A. Beljaars, J.-F. Mahfouf, and J. Teixeira, 1999: The representation of soil moisture freezing and its impact on the stable boundary layer. *Q. J. Roy. Met. Soc.*, **125 (559)**, 2401–2426.

Volodin, E., N. Dianskii, and A. Gusev, 2010: Simulating present-day climate with the INMCM4.0 coupled model of the atmospheric and oceanic general circulations. *Izvestiya Atmospheric and Oceanic Physics*, **46 (4)**, 414–431.

Watanabe, S., et al., 2011: MIROC-ESM 2010: model description and basic results of CMIP5-20c3m experiments. *Geosci. Model Dev.*, **4**, 845–872.

Wegener, A., 1911: *Thermodynamik der Atmosphäre*. JA Barth, Leipzig, Germany.

Wexler, H., 1936: Cooling in the lower atmosphere and the structure of polar continental air. *Mon. Wea. Rev.*, **64**, 122–136.

Whiteman, G., C. Hope, and P. Wadhams, 2013: Climate science: Vast costs of arctic change. *Nature*, **499 (7459)**, 401–403.

Winton, M., 2006: Amplified Arctic climate change: What does surface albedo feedback have to do with it? *Geophys. Res. Lett.*, **33 (3)**, L03 701.

Wu, T., et al., 2010: The Beijing Climate Center atmospheric general circulation model: description and its performance for the present-day climate. *Climate Dyn.*, **34 (1)**, 123–147.

WWRP, 2014: WWRP Polar Prediction Project Year of Polar Prediction (YOPP) Implementation Plan. available online at http://polarprediction.net/en/documents/ , last accessed 20th February 2014.

Xie, S., et al., 2010: CLOUDS AND MORE: ARM Climate Modeling Best Estimate Data. *Bull. Am. Met. Soc.*, **91 (1)**, 13–20.

Yukimoto, S., Y. Adachi, and M. Hosaka, 2012: A New Global Climate Model of the Meteorological Research Institute: MRI-CGCM3: Model Description and Basic Performance (Special Issue on Recent Development on Climate Models and Future Climate Projections). *J. Met. Soc. Japan*, **90**, 23–64.

Zhang, M., J. Hack, J. Kiehl, and R. Cess, 1994: Diagnostic study of climate feedback processes in atmospheric general circulation models. *J. Geophys. Res.*, **99 (D3)**, 5525–5537.

Zhang, Y., D. Seidel, J. Golaz, C. Deser, and R. Tomas, 2011: Climatological Characteristics of Arctic and Antarctic Surface-Based Inversions. *J. Climate*, **24 (19)**, 5167–5186.

Zilitinkevich, S., T. Elperin, N. Kleeorin, and I. Rogachevskii, 2007: Energy-and flux-budget (efb) turbulence closure model for stably stratified flows. part i: steady-state, homogeneous regimes. *Boundary-layer Met.*, **125 (2)**, 167–191.

Acknowledgements

In my three years as PhD candidate at the Max Planck Institute for Meteorology in Hamburg, I enjoyed both a great support and great freedom to determine and change the scope of my work. I owe these privileges to my supervisor Thorsten Mauritsen, who also had the wonderful idea to start this PhD project at the interface of boundary-layer meteorology and climate science. Input and questions from Bjorn Stevens both inside and outside of panel meetings helped me to extend my understanding of the climate system and to improve my own work. Thanks to Andreas Chlond for being a dedicated and efficient panel chair.

Many more have allowed me to develop an understanding of the processes controlling our climate by sharing their insights throughout my studies and PhD work. I am especially grateful to Brian Medeiros, who was my host when visiting NCAR, Tiina Nygård, who taught an inspiring lecture on Arctic inversions at a field school in Svalbard, and Erich Roeckner for answering my questions on the inner workings of ECHAM. Wayne Angevine was incredibly helpful in implementing the total turbulent energy scheme, and Jade Garcia shared her data and insights from direct numerical simulations of turbulence. I was lucky to have Julien Boé discuss the findings of his paper and share the original data with me. Florian Rauser, Dirk Notz, Lorenzo Tomassini, Ann Kristin Naumann, Vera Schemann and anonymous reviewers at the Journal of Climate, Climate Dynamics and Nature Geoscience provided valuable feedback on different parts of this work.

Scientific progress is always built on the achievements of the past, and I was fortunate to use a variety of tools and data sets developed and provided by others: Karoline Block computed radiative kernels for MPI-ESM and helped me to apply them. Brian Soden and Karen Shell made their sets of kernels available, the modelling groups, the Program for Climate Model Diagnosis and Intercomparison and the World Climate Research Program's Working Group on Coupled Modelling made available the CMIP3 and CMIP5 multi-model data sets and researchers involved in the collection of SHEBA and ARM data also shared their results. ERA40 and ERA-interim reanalysis data have been obtained from the ECMWF data server. The HadCRUT3v data set has been provided by the Climatic Research Unit at the University of East Anglia. LES data for the GABLS1 case was made available by Beare et al. (2006).

Acting as spokesperson for Max Planck Society's network of PhD candidates gave me a wider picture of how science and especially doctoral education is being organised in

the MPS, and I believe that the MPI for Meteorology and its International Max Planck Research School on Earth System Science can serve as examples of best practice in many aspects of supporting PhD candidates.

Finally, I would like to thank Suvarchal Kumar Cheedela for developing and helping with the single-column version of ECHAM6, Monika Esch for helping out whenever I couldn't make the model run or compile, Antje Weitz and the IMPRS office for their support, and Vera Schemann for introducing me to the institute and sharing all the LaTeX templates I ever needed.

List of publications

Parts of this thesis have been published as scientific papers:

- Chapter 2: Pithan, F. and T. Mauritsen, 2014: Arctic amplification dominated by temperature feedbacks in contemporary climate models, *Nature Geoscience* 7, 181-184
- Chapter 3: Pithan, F. and T. Mauritsen, 2013: Comments on 'Current GCM's unrealistic negative feedback in the Arctic', *J. Climate*, 26(19), 7783-7788
- Chapter 4: Pithan, F., B. Medeiros and T. Mauritsen, 2013: Mixed-phase clouds cause climate model biases in Arctic wintertime inversion strength, *Climate Dynamics*, doi: 10.1007/s00382-013-1964-9

Eidesstattliche Versicherung

Hiermit erkläre ich an Eides statt, dass ich diese Arbeit selbst verfasst und keine anderen als die angegebenen Quellen und Hilfsmittel benutzt habe.

Felix Pithan

Hinweis / Reference

Die gesamten Veröffentlichungen in der Publikationsreihe des MPI-M
„Berichte zur Erdsystemforschung / Reports on Earth System Science“,
ISSN 1614-1199

sind über die Internetseiten des Max-Planck-Instituts für Meteorologie erhältlich:
http://www.mpimet.mpg.de/wissenschaft/publikationen.html

All the publications in the series of the MPI -M
„Berichte zur Erdsystemforschung / Reports on Earth System Science“,
ISSN 1614-1199

are available on the website of the Max Planck Institute for Meteorology:
http://www.mpimet.mpg.de/wissenschaft/publikationen.html